Development and Field-Deployment of an Absorption Spectrometer to Measure Atmospheric HONO and NO2

Dr. Steven C. Wofsy Hwan Kyu Lee

Development and field-deployment of an absorption spectrometer to measure atmospheric HONO and NO_2

Abstract

Field observations show daytime HONO levels in urban, rural and remote environments are typically greater than those expected at photostationary state, that is, balance between production by the homogeneous NO+OH reaction and loss by UV-photolysis and OH-oxidation. Studies have interpreted measurements of $[HONO]_{Obs} > [HONO]_{PSS}$ – or equivalently, the rate of HONO loss exceeding that of production – as evidence of a missing, sunlight-driven HONO source. Formation rate inferred from assuming photostationarity indicate a significant, yet-unaccounted source of HONO, which photolyzes to yield OH. Moreover, depending on the mechanism, this source may represent a pathway by which deposited nitrogen oxides are repartitioned back into the atmosphere in reactive form.

The accumulation of HONO beneath the nocturnal boundary layer initiates photochemistry in the early morning prior to other HO_x precursors. Previous studies have estimated nighttime HONO production rate by attributing the increase in $HONO:NO_x$ solely to heterogeneous HONO formation, while treating NO_x as an invariant. Moreover, because ambient $HONO:NO_x$ exceed what is observed in automobile exhaust, combustion sources are discounted.

In May of 2009, we observed HONO and NO_2 mixing ratios in Houston, Texas during the SHARP campaign. We demonstrate – using a chemical box model – that photostationary state during daytime is not fully established. The reaction/transport time since emission from automobiles is short relative to the lifetime of HONO. The result of assuming PSS is a drastic over-estimation of the magnitude of the so-called missing HONO source. At night, we show that

NO_x oxidation and emission are significant, thus, NO_x cannot be treated as a conservative tracer to infer secondary HONO production.

Nearly-continuous observations of HONO and NO_2 at Harvard Forest from December 2010 to December 2011 reveal daytime HONO levels that are comparable to what is expected from just known chemistry and much lower than has been reported in similar environments by different measurement techniques. Moreover, HONO fluxes are always below detection limit, indicating daytime HONO production contributes negligibly to the HO_x and NO_x budgets of the overlying atmosphere at Harvard Forest. Nighttime HONO enhancement is observed, but high night-to-night variability in HONO:NO_2 that is not reasonably explained by the trends in HONO and NO_2 fluxes, suggest a non-NO_2, non-ground/canopy-surface related HONO source.

Acknowledgments

First, I would like to thank my thesis committee: Steve Wofsy, Daniel Jacob and Bill Munger. I thank my advisor Steve Wofsy for allowing me to join his group and for trusting in me to pursue my own research interests. After decades in the field he has helped to build, after countless accolades, Steve still exudes a contagious excitement for formulating new experiments to address vital and pertinent questions, and that is who I aspire to be. I thank Bill Munger, without whom my thesis would have been impossible. From basic engineering to field work to constructing manuscripts, he has guided me at every step of my research. I thank Daniel Jacob for setting the standard on how to give an effective lecture/presentation, for teaching us that it is not only okay but encouraged to ask tough questions during seminars, and for so eloquently demonstrating the importance of being concise by stating, "every word must hurt."

I am grateful to current and former members of the Wofsy group who have helped me in invaluable ways. In particular, I thank Greg Santoni for being there with me at our first field experiment, for making even the most tedious task entertaining. I appreciate the endless hours of scientific discussions with Eric Kort and all the feedback he has given me over the years. I thank my officemates Marcos Longo and VY Chow for putting up with me and my occasional grumpy moods. The field deployment at Harvard Forest would not have been possible and not nearly as enjoyable without my friend and colleague, Josh McLaren.

I thank the friendly and incredibly supportive members of Aerodyne Research, Inc., in particular, Mark Zahniser for his infinite patience and wisdom. I thank Dave Nelson and Barry McManus, neither of whom showed any annoyance at my endless questions and demands for assistance. I thank Chuck Kolb for being so welcoming, and for regaling me with stories of how

instrument work used to be back in the days to help me feel better about my own instrument woes. I thank Scott Herndon for stressing the importance of efficiency and pragmatism. I am indebted to Ezra Wood, my former graduate student instructor at Berkeley, who has had the unenviable task of reading every one of my first drafts. I appreciate the helpful work and words from Ryan McGovern, Stanley Huang, John Jayne, Joanne Shorter and Jody Wormhoudt.

I am grateful for having been a part of the Earth and Planetary Sciences and Atmospheric Chemistry communities at Harvard, an exciting and challenging environment in which to work. I would like to thank members of Daniel's group especially for providing me a different scientific and methodological perspective, inspiring discussions, for fielding my elementary-level questions regarding global models and for creating and managing the atmospheric chemistry journal club. The administrative staff in EPS, in particular, Brenda Mathieu and Arlene Pippen have been tremendous.

Finally, I would like to thank my family and friends, for their love and support. Seven at-times-grueling years of graduate school certainly would not have been possible without our mutual desire for fun, food and distractions with friends, especially Hilary Close, Patrick Kim, John Crowley and Justin Parrella. I want to thank my girlfriend Young Ji Ham for being so understanding, particularly near the completion phase of my thesis, and for helping me to have a more balanced life.

This work was funded by the National Science Foundation Awards No. AGS – 0813617 and 0814202.

Table of Contents

List of Figures

Chapter 2

Chapter 3

Figure 4.4. a) Ratio of HO_x radical production rate in jet exhaust relative to those under "typical" urban conditions (~0.5 parts per trillion per second), plotted versus plume dilution factor. HO_x is produced from the photolysis of precursors including HONO, HCHO, CH_3CHO and the ozonolysis reactions between O_3 and alkenes. b) Relative strengths of HO_x sources in jet exhaust.

Figure 4.5. Plume dilution factor calculated from CO_2 measurements made at varying distances from the emission source, plotted versus distance.

Chapter 5

Figure 5.1. Schematic of the instrumental setup used to determine absorption parameters for the *cis* conformer.

Figure 5.2. Time series (1-hertz) of HONO, NO_2 and NO (measured by two different instruments) mixing ratios (ppb) during two gas addition experiments. Addition of a) NO_2 from a permeation device and from generated b) HONO.

Figure 5.3. Absorbance (base e) spectra of *cis*-HONO (top panel) and effective line strengths (bottom panel) from KMH (black) and this study (red), all plotted as a function of wavenumber (cm^{-1}). Listed numbers represent the ratio of KMH strengths to those from this study. Brackets above the figure summarize each experimental condition. Asterisks point to degenerate entries in KMH due to limited spectral resolution.

Figure 5.4. Same as figure 3, for *trans*-HONO.

Figure 5.5. Absorbance spectra (base 10) obtained by S04 (black) and KMH (grey) of the ν_2 bands of *cis* and *trans*-HONO centered around 1640 and 1699 cm^{-1}, respectively. While there is good agreement between the two spectra for the *trans* conformer, the S04 spectrum is lower than that of KMH by about a factor of two for the *cis* conformer.

Chapter 6

Figure 6.1. a) Small grey symbols show the hourly-averaged measured:PSS ratio and b) sum of HONO production (R1) and loss rates (R2+R3), both plotted as a function of time of day (CST). The large black line-connected markers represent the overall median for each daytime hour during the SHARP campaign.

Figure 6.2. Simulated time-series of (a) [NO], $[NO_2]$, $[HONO]_{time\text{-}integrated}$ and $[HONO]_{instantaneous\text{-}PSS}$ in vehicle exhaust for constant [OH] = 0.5 ppt and constant $[O_3]$ = 30 ppb, (b) sum of the production (R1) and loss (R2+R3) rates of HONO and (c) the ratio of time-integrated:instantaneous-PSS HONO for the four cases. (d) Probability distribution of the age of air mass that was assigned to each simulation, the result of which is summarized in figure 3.

Figure B7. Complete times series of 1-hr averaged HONO and NO_2 mixing ratios measured by the dual-laser absorption spectrometer at Harvard Forest from December 2010 to December 2011. Gaps in the data are due to power flickers, instrument failures and routine maintenance.

Figure B8. Side by side spectra (1-hr averaged) of ambient and background HONO (top) and NO_2 (bottom).

Figure B9. Additions of HONO with full setup (left), without the 180 feet of tubing (middle) and without inlet or tubing (right).

Figure B10. Scatter plot showing enhancement of HONO during additions of NO_2 on top of dry room air, humid Houston air and humidity-matched zero-air.

Figure B11. Top panel shows HONO and NO_2 mixing ratios during a 12-hr zero-addition experiment, when the instrument was exposed to typical temperature swings inside the shed at Harvard Forest. Allan variance analysis shows 1-s (1σ) noise for HONO and NO_2 decrease from 100 ppt and 15 ppt by a factor of 20 and 10, respectively, with 1-hr averaging.

Figure B12. Lag-correlation plot of HONO' and NO_2', lagged against w'.

List of Tables

Chapter 1:

Introduction

Numerous studies infer the existence of a strong, yet-unconstrained daytime nitrous acid (HONO) forming pathway. Given the reported rates, this sunlight-driven source can have a significant impact on the cycling of HO_x and NO_x species near the Earth's surface. This so-called missing HONO source, it has been argued, may close the gap in the model-measured discrepancy of boundary layer OH levels. However, previous measurements – particularly in rural and remote environments – have been made utilizing wet-chemical extraction methods, which have not always demonstrated good agreement with optical techniques.

A robust, field-deployable dual-laser absorption spectrometer was constructed to measure the mixing ratios and eddy covariance fluxes of HONO and NO_2, a hypothesized HONO precursor. The sampling system consists of a filter-free inlet followed by temperature-controlled, shielded tubing to draw ambient air down from aloft to the ground-based instrument. Routine in-field tests demonstrated the absence of positive and negative artifacts. We report detection limits (3σ 1-hr) below 15 and 5 ppt for HONO and NO_2, respectively, with one-hour spectral averaging. We determined experimentally in a laboratory experiment the absorption parameters – including line strengths and air-broadening coefficients in the 6 and 8 micron spectral regions – to accurately quantify gaseous HONO spectroscopically.

The goal of my thesis was to characterize the production and loss processes of atmospheric HONO in a polluted, urban environment and above a rural forest in New England. The aim was to quantify the impact of daytime HONO production on the NO_x and HO_x budgets. Aided by

accompanying measurements and from long-term deployments, the chemical reaction(s) responsible for this HONO source was to be determined.

The following six chapters are each self contained, with an abstract, introduction, results, conclusion and references. In chapter 2, I discuss the instrument structure, performance and applicability. In chapters 3 and 4, measurements of HONO aircraft emission indices during the Alternative Aviation Fuel Experiment (January 2009 in Palmdale, California) and their potential impact on air quality are described. Chapter 5 outlines the laboratory experiment to determine HONO absorption parameters – which are not accurately represented in any comprehensive linelist – in the 6 and 8 micron spectral regions. Chapter 6 discusses HONO and NO_2 measurements during the Study of Houston Atmospheric Radical Precursors campaign (May 2009 in Houston, Texas) and the invalidity of assuming air masses sampled in urban areas are at all times at photostationary state. Finally, chapter 7 concludes by summarizing nearly-continuous, year-long measurements of HONO and NO_2 above the canopy at Harvard Forest. A conclusion chapter sums up the main findings of the thesis and presents potential future research.

Chapter 2:

Simultaneous measurements of atmospheric HONO and NO_2 via absorption spectroscopy using tunable mid-infrared continuous-wave quantum cascade lasers[1]

Abstract

Nitrous acid (HONO) is important as a significant source of hydroxyl radical (OH) in the troposphere and as a potent indoor air pollutant. It is thought to be generated in both environments via heterogeneous reactions involving nitrogen dioxide (NO_2). In order to enable fast-response HONO detection suitable for eddy-covariance flux measurements and to provide a direct method that avoids interferences associated with derivatization, we have developed a 2-channel tunable infrared laser differential absorption spectrometer (TILDAS) capable of simultaneous high-frequency measurements of HONO and NO_2. Beams from two mid-infrared continuous-wave mode quantum cascade lasers (cw-QCLs) traverse separate 210 m paths through a multi-pass astigmatic sampling cell at reduced pressure for the direct detection of HONO (1660 cm^{-1}) and NO_2 (1604 cm^{-1}). The resulting one-second detection limits (S/N=3) are 300 and 30 ppt (pmol/mol) for HONO and NO_2, respectively. Our HONO quantification is based on revised line-strengths and peak-positions for *cis*-HONO in the 6-micron spectral region that were derived from laboratory measurements. An essential component of ambient HONO measurements is the inlet system and we demonstrate that heated surfaces and reduced pressure minimize sampling artifacts.

[1] Lee, B. H, Wood, E. C, Zahniser, M. S., McManus, J. B., Nelson, D. D., Herndon, S. C., Santoni, G. W., Wofsy, S. C., and J. W. Munger[1] (2011), *Appl. Phys. B*, **102**, 417-423, doi:10.1007/s00340-010-4266-5.

2.1. Introduction

Atmospheric nitrous acid (HONO) photo-dissociates with a lifetime between 10 and 20 minutes to yield nitric oxide (NO) and hydroxyl radical (OH), the main oxidant in the atmosphere. Nighttime HONO formation and photolysis at sunrise can contribute significantly to early morning photochemistry. Observations of mid-day HONO concentrations above levels expected from photo-stationary balance between HONO, NO and OH suggest a yet unidentified light-dependent production mechanism. These measurements have used various instruments in a wide range of environments [1-3]. Thus, HONO may make a larger contribution to the HO_x (= $OH + HO_2$) cycle in the lower troposphere than has been accounted for by its nighttime formation. In addition, HONO chemistry may contribute to reactivating deposited nitrogen, which was presumed to be permanently removed from photochemical cycle. HONO is also an indoor air pollutant – both emitted directly from combustion processes and formed on various surfaces – and can react with amines to form carcinogenic compounds [4, 5]. NO_2 is proposed as a precursor to HONO formation via heterogeneous reactions. In order to examine the exchange of HONO between the biosphere and atmosphere and the role of NO_2 in this exchange, we have developed a dual-laser spectrometer to simultaneously measure both gases.

Several factors make accurate HONO measurements difficult. It is unstable so certified reference gases for HONO do not exist. Its reactivity and solubility also make it prone to sampling losses and artifacts. Consequently, inter-comparisons between different techniques often exhibit significant discrepancies [2, 6]. Further progress on understanding HONO sources and sinks requires a sensitive and unambiguous measurement method.

There are many methods to detect HONO, but they do not fully satisfy the need for sensitivity, selectivity and fast time response. Analytical techniques based on derivatization partition gaseous HONO into a liquid and subsequently measure the nitrite ion or its derivative by ion or liquid chromatography, long-path photometry or chemiluminescence [4, 7-9]. Although these methods can be very sensitive, the need to scrub HONO into solution may introduce sensitivity to any other gas-phase species that react with the solution [6]. Such interferences can be corrected if the chemically active species is quantifiable [10]. Furthermore, the need for long extraction integration times (a few minutes) precludes the application of these methods to eddy-covariance flux measurements.

Absorption spectroscopy directly measures atmospheric trace gases without the need for chemical extraction, with calibrations that are based on constant absorption cross-sections (line-strengths) and specificity that can be confirmed by spectral identification. However, absorption spectroscopic analytical methods tend to be expensive, and for many trace gases the fundamental sensitivity is relatively low, requiring either long absorption paths or increased signal averaging time. Both open-path (differential optical absorption spectroscopy, DOAS) [1, 11, 12] and closed-path (tunable diode laser absorption spectroscopy, TDLAS) [13, 14] systems have been utilized to measure HONO. Based on a prior implementation of nitric acid (HNO_3) and NO_2 TDLAS [15-17], we have developed a dual-channel tunable infrared laser differential absorption spectrometer (TILDAS) using continuous-wave quantum-cascade lasers instead of diode lasers to measure HONO and NO_2. The advantages of using cw-QC lasers in TILDAS over diode lasers in TDLAS are greater mode stability, higher laser power output and the ability to operate both lasers and detectors near room temperature without the need for cryogenic cooling, which facilitates long-term field measurements. The spectrometer is coupled with sample handling and

calibration schemes intended to minimize inlet artifacts and provide quality-assurance that the system is working properly. Section 2 describes the spectrometer design and quantifies performance. Section 3 presents results from the investigation of HONO line-strengths and peak-positions. Section 4 describes the sampling scheme and presents preliminary results from field measurements demonstrating the absence of positive and negative artifacts.

2.2. Instrument

The main components of the optical table (Figure 1) include two light sources, a reference cell, multi-pass sampling cell and two detectors. For the light source, the spectrometer uses two thermo-electrically cooled QC lasers (Alpes Lasers) operated in continuous-wave mode that output light in the 6-micron spectral region. The laser light is scanned across a frequency spectrum in time by controlling its temperature, which is coarsely tuned with a Peltier element and finely tuned on a milli-Kelvin scale by providing the lasers with a programmable current ramp using a high compliance current source (ILX Lightwave). The resulting laser frequency scan covers approximately 0.2 cm^{-1} with a resolution of about 0.001 cm^{-1} per channel. The instrumental line-widths for both lasers are less than 0.001 cm^{-1} (half-width at half-maximum), which is smaller than Doppler broadened widths. The tuning rates of each laser are determined with a germanium etalon.

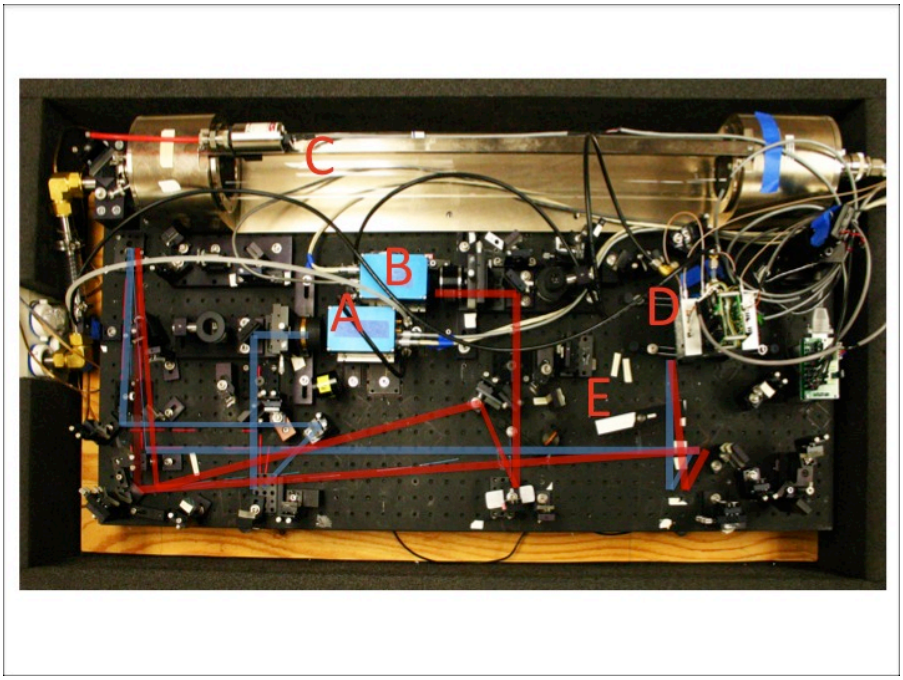

Figure 2.1. Optical table of the dual cw-QC laser spectrometer. A = QC laser (1660 cm^{-1}, HONO); B = QC laser (1604 cm^{-1}, NO_2); C = astigmatic multi-pass sampling cell; D = thermo-electrically cooled detector; E = reference cell filled with NO_2 and HONO. The blue and red traces represent paths traveled by the HONO (1660 cm^{-1}) and NO_2 (1604 cm^{-1}) laser light, respectively. The traces for the reference cell and normalization are not shown. The optical table has a footprint of 2 ft × 4 ft (0.6 m × 1.2 m).

The two lasers are spatially and temporally multiplexed so that even though light from each laser traverses distinct paths inside and outside the sampling cell, both beams are collected by a single detector at alternate times on the order of 1 ms for each laser. The spectra for NO_2 (1604.5 to 1604.7 cm^{-1}) and HONO (1659.5 to 1659.7 cm^{-1}) are repeatedly scanned one after the other at a total rate of about 3 kHz and are subsequently averaged in real-time to improve the signal to noise ratio. Approximately 10% of the duty cycle is dedicated to measuring the detector zero light level when both lasers are off. The spectral fitting software (TDLWintel, also responsible for the laser control) determines the absorbance by performing a non-linear fit according to a set of Voigt line shape functions to the recorded spectra and a low-order polynomial fit to the spectral baseline. Mixing ratios are calculated by accounting for the sample pressure and temperature along with spectral broadening and IR line-strengths archived in the HITRAN database for NO_2 [18] and determined experimentally here for HONO (discussed below). Figure 2 shows transmission spectra of HONO and NO_2 observed during calibration gas additions.

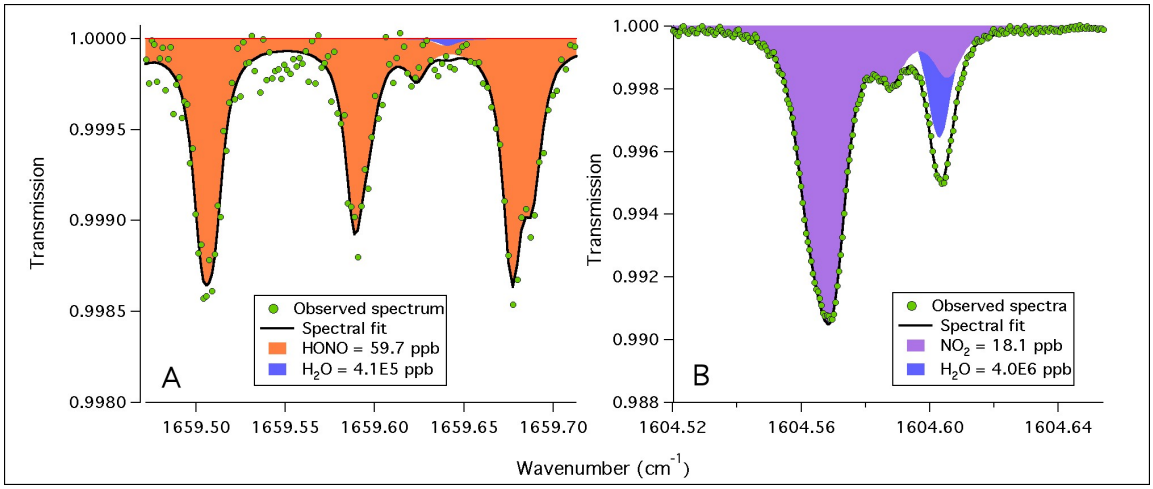

Figure 2.2. Transmission spectra, averaged over 30-seconds, of (A) HONO and (B) NO_2 at 40 torr. The colored areas represent the fits to the observed spectra (green dots) according to the known peak-position, line-strength and recorded pressure and temperature.

Ambient air is sampled through an inlet and transported in tubing (discussed below) to the sampling cell, which is maintained at a constant reduced pressure to minimize spectral overlap with other infrared-light absorbing species (especially water), while maintaining sufficient absorption depths for high sensitivity. Light from each laser enters the multi-pass cell and reflects between two astigmatic mirrors with multilayer dielectric coatings (reflectivity ~0.998, LohnStar Optics, Inc.). The mirrors are spaced 0.88 m apart and obtain 238 passes, resulting in a total path-length of 210 m. The light exits the cell through the entrance coupling-hole and is directed onto a thermo-electrically cooled detector (Vigo). It should be noted that a liquid-nitrogen cooled HgCdTe detector – which due to its larger active detector area is less susceptible to aiming changes – could be used to improve overall stability. However, the costs and measurement interruptions associated with liquid nitrogen fills for a comparable level of sensitivity with the HgCdTe detectors, make the thermo-electrically cooled detectors a preferred option.

The optical table also includes secondary and tertiary light paths, both external to the sampling cell – derived from the reflections off the front and back surfaces of a transmission beam splitter. One path is directed through a 7 cm path-length reference cell filled with gaseous HONO and NO_2. The spectra of this transmitted light is continuously measured by a second detector and is used to "lock" the lasers to the desired absorption features of HONO and NO_2, which is necessary when ambient levels of the species of interest are too low to observe significant absorbance in real-time and also preferred for the routine additions of zero-air, or ambient air scrubbed of these gases. The third beam and detector could be used to normalize out power variability associated with the light source, if desired, but has not been implemented. Details regarding the laser control, optical trace and alignment, data acquisition system, spectral

fitting software, detectors and sampling cell have been discussed at length previously [17, 19-22].

Absorbance precisions less than 3×10^{-6} $Hz^{-1/2}$ (1.4×10^{-10} cm^{-1} $Hz^{-1/2}$) and 5×10^{-6} $Hz^{-1/2}$ (1.9×10^{-10} cm^{-1} $Hz^{-1/2}$) are achieved for HONO and NO_2, respectively. The NO_2 channel is slightly noisier due to the inherent variability of this particular QC device. We achieve the same absorbance precision as that of HONO by utilizing normalization [22]. Normalization with intermittent peak-position locking could be implemented in this dual detector configuration, however, it does not improve HONO sensitivity. Furthermore, at the low HONO mixing ratios expected in rural environments, intermittent line-locking is not adequate to maintain the laser tuning. We sacrifice some NO_2 sensitivity, which is not needed for typical ambient NO_2 levels, to ensure accurate HONO spectroscopy. For measurements at cell pressure of 40 torr, the one-second 1-σ precisions for HONO and NO_2 are 100 and 10 ppt (6 ppt if absorbance precision observed for HONO is achieved for NO_2), respectively. Long-term stability is limited by optical fringes that change with temperature, causing drifts in the spectral baseline. These effects may be minimized by frequent background spectrum subtractions obtained by flushing the cell with HONO and NO_2 scrubbed air, or zero-air, which is generated by passing ambient air over a heated palladium catalyst. This source of zero-air does not significantly alter the water-vapor mixing ratio, which is critical because there are weakly absorbing H_2O features in both the HONO and NO_2 scans (Figure 2). Time averaging improves the precision of HONO and NO_2 measurements by a factor of 10 or better over an integration time of 30 minutes, which is a typical interval to compute eddy covariance over a forest canopy, with background spectra subtractions conducted once every 5 minutes (Figure 3).

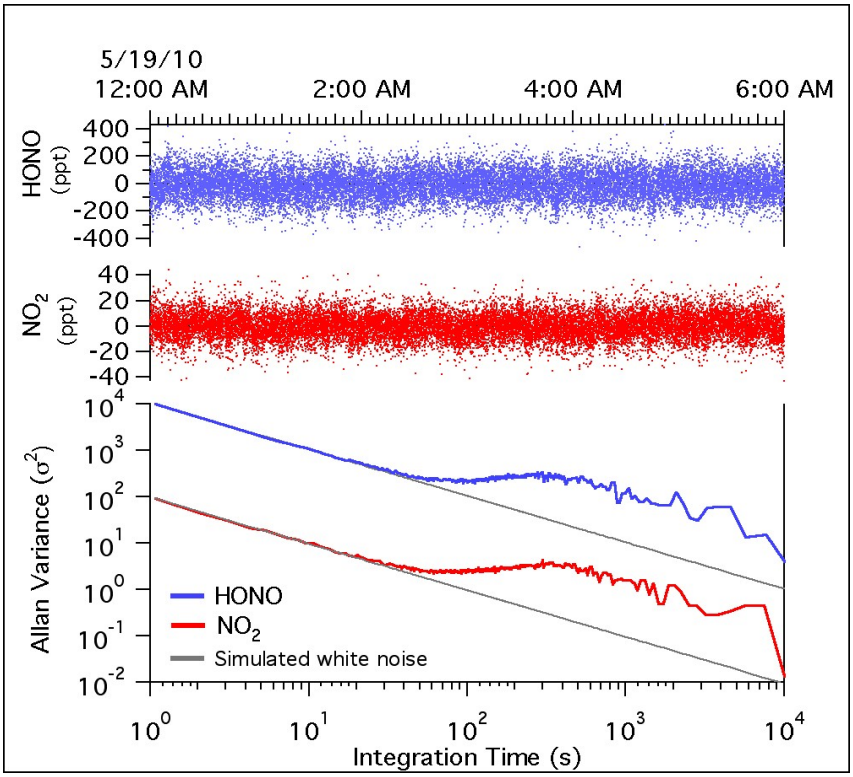

Figure 2.3. The top two panels show HONO (blue) and NO_2 (red) mixing ratios in ppt (pmol/mol) measured in zero-air at 40 torr. The Allan variance plot on the bottom panel shows the decrease in instrument variance with time averaging for both species. Deviation from pure white or random noise occurs due to slow-moving temperature-driven optical fringes, but is addressed with frequent spectral background subtractions, here conducted every fifth minute for 30 seconds (20 seconds to obtain an average background spectrum and 10 seconds of flush time). The y-intercepts on the Allan variance plot representing the 1-second 1σ measurement noise for HONO and NO_2 are 9.4×10^{3} and 8.8×10^{1} ppt^2 Hz^{-1}, or 97 and 9.4 ppt $Hz^{-1/2}$, respectively.

An optimal spectral region is selected based upon the maximum absorption cross-section and minimum absorbance by other gases that may be present in the sample. We selected the 6-micron region (Figure 2) where lasers, detectors and mirrors were all available allowing simultaneous measurements of HONO and NO_2. There are, however, alternative spectral regions where HONO absorbs mid-infrared light much more strongly, which may improve sensitivity. In particular, HONO absorption lines at 1708.998, 1713.511, 1247.165 and 1273.598 cm^{-1} may increase precision by a factor of three to five, however, the 8.0 micron region would be costly for NO_2 measurement sensitivity and at this time no appropriate lasers are available in the 5.8 micron region.

2.3. Line-strengths

The accuracy of the mixing ratios obtained using absorption spectroscopy largely depends on the accuracy of the absorption cross-section or line-strength. For long-lived gases and other well-studied species such as NO_2, the absorption parameters are well characterized and available in publications and in databases such as HITRAN [18]. For HONO, however, there are fewer published studies and greater uncertainty in absolute values, which required us to re-evaluate the HONO spectra.

We determined the amount of infrared (1659.1 to 1660.2 cm^{-1}) light absorbed by the *cis* conformer of HONO while sampling a known amount of total (*cis* + *trans*) HONO at the given constant temperature of 303 K, hence at a constant *cis* to *trans* ratio. This *effective* line-strength of *cis*-HONO was obtained by introducing high levels of gaseous HONO (between 300 and 800 ppb) – generated by passing HCl vapor over powdered $NaNO_2$ [23] – into the sampling cell at low pressures (< 9 torr) to minimize absorption line overlap while maintaining high signal to

noise. In parallel, we quantitatively converted the same HONO source to NO using a heated molybdenum catalyst and quantified NO with a pulsed-mode QC laser (1906.73 cm^{-1}, Hamamatsu Photonics) spectrometer calibrated against a traceable NO standard to determine the absolute HONO concentration. Because NO is relatively inert, it is less susceptible to line-losses and can be accurately calibrated using traceable gas mixtures.

Deviation of the sample from the temperature at which our effective line-strengths were determined will result in a change in the *cis* to *trans* ratio. The effective line-strengths can be corrected knowing the *cis-trans* energy barrier, for which there is a large discrepancy amongst reported values [24-28]. In practice, a constant sample temperature is well maintained by heating the inlet, tubing, the optical table and its protective cover. Furthermore, routine calibration gas additions are conducted in the field to ensure the accuracy of the measurements, as discussed in the next section. Lastly, because the time required for isomerization to occur is much shorter ($\sim 10^{-12}$ seconds) than that needed for ambient air to travel through the inlet and subsequent tubing to the sampling cell (~1 second), we expect the HONO conformers to be in thermal equilibrium and independent of changing ambient conditions.

Line positions and effective line-strengths used in the spectral fits in Figure 2 are listed in Table 1. Additional details regarding this experiment, along with comparison of the relative absorption strengths between *cis* and *trans* conformers, determination of the pressure-broadening coefficient, comparison to values in the ATMOS database and to a high-resolution FTIR spectrum are part of an ongoing analysis that is not yet complete.

Peak position (cm^{-1})	Effective line-strength (cm^2 molecule^{-1} cm^{-1}) $\times 10^{-21}$
1659.5031	9.571
1659.5099	8.810
1659.5887	10.15
1659.5968	3.283
1659.6238	1.863
1659.6770	12.92
1659.6886	7.419

Table 2.1. Peak-position and *effective* line-strength of *cis*-HONO between 1659.5 and 1659.7 cm^{-1} measured at 303 K.

2.4. Sampling technique

Figure 4 shows a schematic of the inlet manifold we use for minimizing contact between sampled ambient air and moist surfaces, for removing coarse particles by inertial separation and for routine additions of reference gases and zero-air. HONO (Henry's Law constant, K_H = 50 M atm^{-1}) – though not nearly as soluble as HNO_3 (K_H =2.1´10^5 M atm^{-1}) – is still photo-chemically active, relatively soluble compared to NO (1.4´10^{-3} M atm^{-1}) and NO_2 (1.2´10^{-2} M atm^{-1}), and mostly dissociated above pH 3.3 [29-32]. In addition to the high probability of HONO equilibrating with accumulated particles and moist surfaces, there is strong evidence for heterogeneous reactions converting precursors to HONO [33]. Consequently, both positive and negative HONO artifacts are a concern, leading us to minimize opportunities for the sample to contact humid surfaces and aerosol that would accumulate on a particle filter.

Surface-adsorbed water is minimized by 1) using a siloxyl-coated quartz inlet to make its surface hydrophobic, 2) heating the inlet, the downstream tubing and sampling cell and 3) reducing the pressure by drawing the sample through a critical orifice built into the inlet (Figure 4). The divergent flows after the orifice – with exhaust vented in line with the incoming flow and the sample air forced to make a 180° turn – cause particles with diameters 4 mm or larger to be separated out of the sample flow by inertia [34, 35]. The inlet and subsequent tubing are shielded from light to avoid photolytic losses and photo-enhanced reactions involving surface adsorbed nitrate ions leading to HONO production [33]. A similarly designed inlet was used successfully to measure formaldehyde, formic acid and ammonia, which are also highly surface active [36, 37].

Frequent in-field artifact testing is an integral part of the instrument system. The manifold is equipped with ports at the entrance of the inlet to allow for routine additions of standards and

zero-air (Figure 4). An outlet adjacent to the flow-restricting orifice is used to draw a subsample of the ambient matrix to a heated Mo catalyst to convert all reducible nitrogen oxides to NO, followed by quantification of the NO by O_3-chemilumiscence. HONO generated from the HCl + $NaNO_2$ source, which typically is > 97% pure, is dynamically mixed with zero-air, added at the inlet entrance in excess of the total sample flow-rate and sampled by both instruments, thereby providing an independent check on the measurements by tying the observations to traceable NO standards. A similar test is applied for NO_2, which is supplied from either compressed gas standards or a permeation tube.

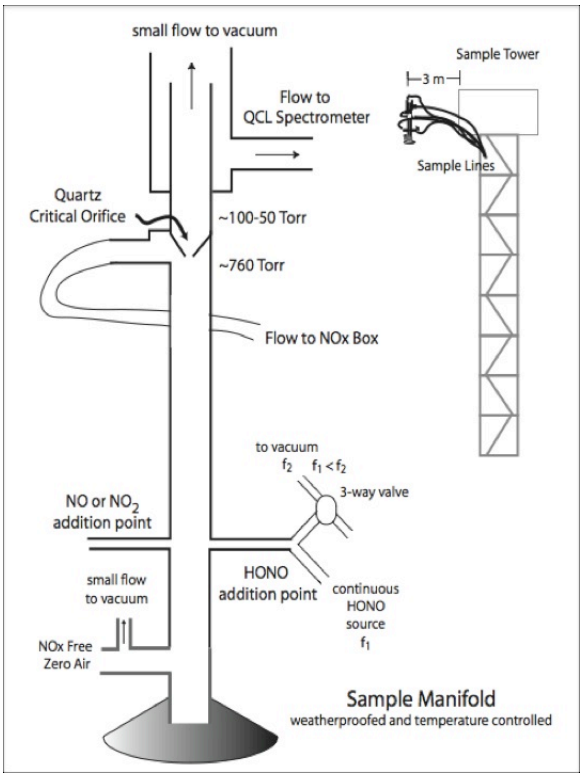

Figure 2.4. Schematic of the quartz inlet manifold. The inlet and subsequent tubing are shielded from light to prevent photolysis and photo-induced surface reactions.

Standard gas additions can also test for temporary surface adsorption that attenuates atmospheric variations. The rise and fall in absorbance when a standard is switched on or off should be nearly instantaneous, with only some delay associated with the flushing time defined by the pumping speed through the inlet, tubing and sampling cell as well as smearing due to mixing and diffusion. These response times can be determined by fitting the mixing ratio time series during standard gas additions to a single exponential curve. A slower response of HONO compared to that of an inert gas would suggest some uptake of HONO on the surfaces. For the current instrumental configuration, HONO response is compared to that of NO_2, which also is generally not attenuated by wall interactions [15-17]. A prototype of this inlet system was deployed at the Study of Houston Atmospheric Radical Precursor (SHARP) campaign in April and May 2009, during which polluted, humid air was sampled through the inlet and 40 ft (12.2 m) of 3/8'' O.D. (9.5 mm) PFA Teflon tubing. Figure 5 shows indistinguishable response times between HONO and NO_2 during additions of both gases at SHARP.

The possibility for positive artifacts from the inlet, tubing or cell surface reactions forming HONO is checked by introducing NO_2 into the inlet in addition to the ambient air matrix. An increase in HONO mixing ratios during these additions would indicate reactions involving NO_2 yielding HONO. During the SHARP campaign, we did not observe any artifact HONO when NO_2 was added to ambient air (Figure 6). Even at NO_2 levels exceeding 100 ppb – well above the range of observed values – there was no change in the HONO mixing ratio, demonstrating freedom from positive artifacts based on NO_2.

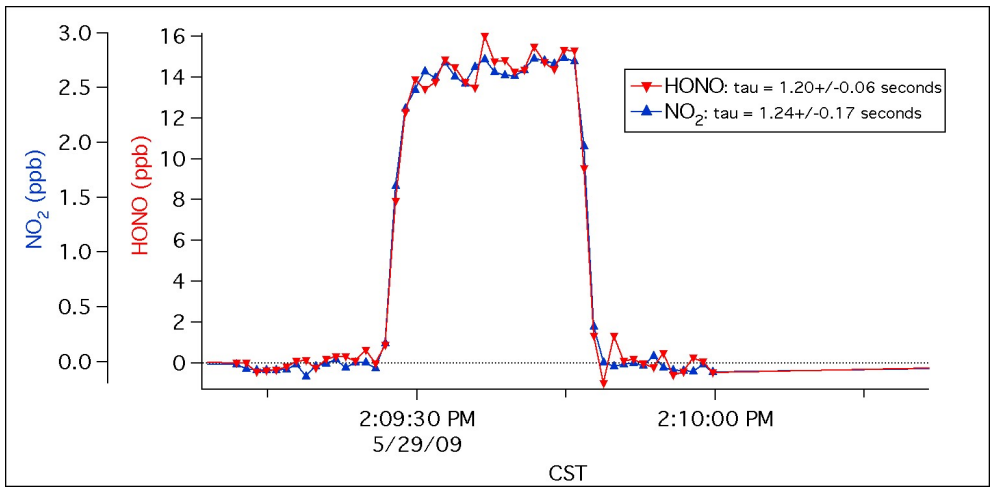

Figure 2.5. One-second mixing ratios of HONO and NO_2 during calibration gas additions, observed during the Study of Houston Atmospheric Radical Precursor (SHARP) campaign in April and May of 2009. The response times (tau) – determined by the pumping speed and cell volume (5 L) – of HONO and NO_2 are indistinguishable, indicating no preferential loss of HONO through the inlet, tubing and sampling cell.

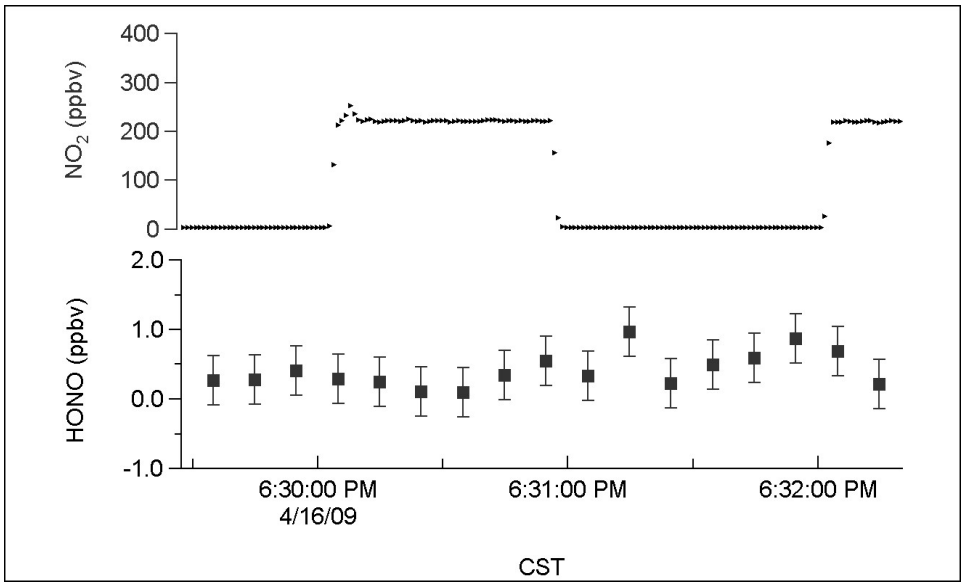

Figure 2.6. One-second mixing ratios of NO_2 (top) and ten-second average mixing ratios of HONO (bottom) during a high-concentration NO_2 addition through 40-feet (12.2 m) of unheated tubing at ambient pressure, conditions under which surface reactions are favored. Note that there is no HONO formed during or immediately following high levels of NO_2 under humid conditions (no positive artifact). The error bars represent the standard deviation of 10-second averaged data.

Figure 7 shows the mixing ratios of HONO and NO_2 measured during the SHARP campaign. The levels of the two species typically co-vary in time as a result of common or co-located emission sources and mixing in the atmosphere. Higher levels are usually observed in the early morning and in the evening when weaker vertical mixing and shallow boundary layer heights promote accumulation of pollutants and photo-chemical losses are reduced compared to mid-day conditions.

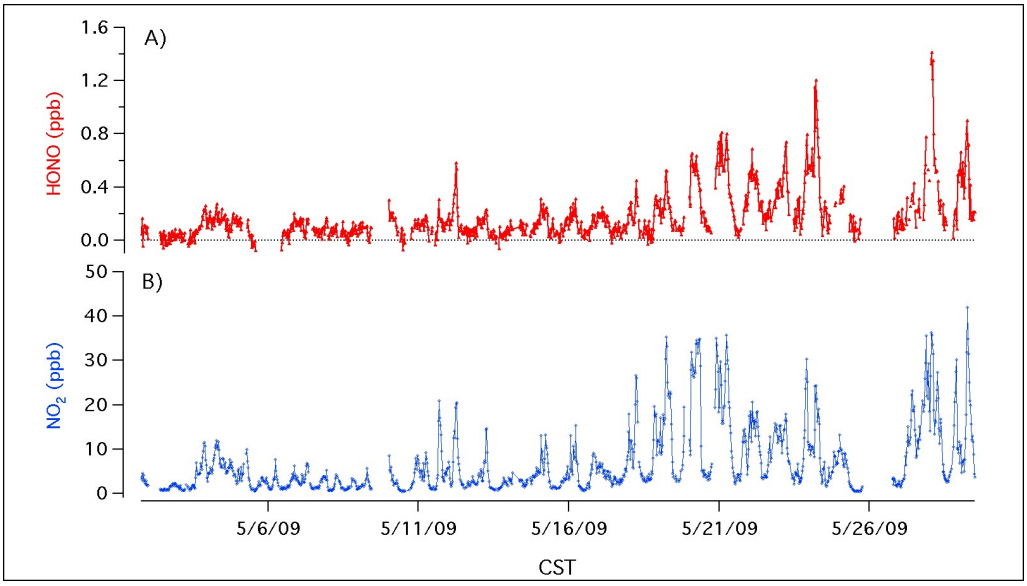

Figure 2.7. Observed 30-minute averaged mixing ratios in ppb (nmol/mol) of HONO (A) and NO_2 (B) during the entire SHARP campaign. Gaps in the data are due to maintenance operations, inlet attenuation/artifact tests and instrument shutdown from power failures.

2.5. Conclusions

This dual continuous-wave mode quantum cascade laser spectrometer has achieved one-second detection limits (S/N = 3) for HONO and NO_2 of 300 and 30 ppt, respectively. Spectral averaging with frequent background subtractions allows further reduction in signal noise, improving the HONO and NO_2 detection limits (S/N = 3) to 35 and 3 ppt, respectively, over a 30-minute integration period. The detection limit for HONO is higher than that for NO_2 – despite better absorbance precision on this channel – due to much weaker line-strengths for *cis*-HONO between 1659 and 1660 cm^{-1} compared to NO_2 at 1604 cm^{-1}. A sample-handling scheme that minimizes adsorbed water on the inlet and subsequent tubing that bring sample into the optical cell is effective at preventing both positive and negative HONO artifacts. The system is designed to allow inlet checks to be a part of routine field operation and provide frequent quality checks on the measurement.

The instrument described in this study was adapted from a previously deployed instrument with a large optical table and near 1 m base-length multi-pass cell. With insulation and a protective cover, the instrument is 3 ft × 6 ft (0.9 m × 1.8 m). The performance demonstrated by this implementation points to the possibility of using a re-designed astigmatic multi-pass cell with a base-length of 47.5 cm and 200 m of absorption path-length. This cell fits on an optical table measuring 43 × 65 cm. Its smaller volume of 1 L allows faster response times and will be more easily portable for field use without any sacrifice in detection limit [38].

The chief advantages of this dual cw-QC TILDAS spectrometer over previous diode laser and pulsed-mode QC laser systems are higher power output and narrower laser line-widths, which provide improved precision and enable thermo-electrically cooled detectors to be used instead of cryogenically cooled detectors that present logistical challenges for long-term, remote

operation in the field. This spectrometer has been deployed at a rural forest to measure the diurnal and seasonal trends in the exchange of HONO and NO_2 between the biosphere and atmosphere.

Acknowledgments

The authors gratefully acknowledge the assistance of Ryan McGovern, Stanley Huang and Daniel Glen of Aerodyne Research, Inc., Josh McLaren and Bruce Daube of Harvard University, and the entire SHARP research team. This work was supported by the National Science Foundation Awards No. AGS – 0813617 and 0814202. Additional funding for the SHARP campaign was provided by the Houston Advanced Research Center Grant No. H113.

References

1. Alicke, B., et al., *OH formation by HONO photolysis during the BERLIOZ experiment*. Journal of Geophysical Research-Atmospheres, 2003. **108**(D4): p. -.

2. Liao, W., et al., *Observations of HONO by laser-induced fluorescence at the South Pole during ANTCI 2003*. Geophysical Research Letters, 2006. **33**(9): p. -.

3. Zhou, X.L., et al., *Summertime observations of HONO, HCHO, and O-3 at the summit of Whiteface Mountain, New York*. Journal of Geophysical Research-Atmospheres, 2007. **112**(D8): p. -.

4. Park, S.S., et al., *Investigation of nitrous acid concentration in an indoor environment using an in-situ monitoring system*. Atmospheric Environment, 2008. **42**(27): p. 6586-6596.

5. Sleiman, M., et al., *Formation of carcinogens indoors by surface-mediated reactions of nicotine with nitrous acid, leading to potential thirdhand smoke hazards*. Proceedings of the National Academy of Sciences of the United States of America, 2010. **107**(15): p. 6576-6581.

6. Kleffmann, J., et al., *Intercomparison of the DOAS and LOPAP techniques for the detection of nitrous acid (HONO)*. Atmospheric Environment, 2006. **40**(20): p. 3640-3652.

7. Dibb, J.E., et al., *Soluble reactive nitrogen oxides at South Pole during ISCAT 2000*. Atmospheric Environment, 2004. **38**(32): p. 5399-5409.

8. Heland, J., et al., *A new instrument to measure gaseous nitrous acid (HONO) in the atmosphere*. Environmental Science & Technology, 2001. **35**(15): p. 3207-3212.

9. Zhou, X.L., et al., *A method for the measurement of atmospheric HONO based on DNPH derivatization and HPLC analysis*. Environmental Science & Technology, 1999. **33**(20): p. 3672-3679.

10. Kleffmann, J. and P. Wiesen, *Technical Note: Quantification of interferences of wet chemical HONO LOPAP measurements under simulated polar conditions*. Atmospheric Chemistry and Physics, 2008. **8**: p. 6813-6822.

11. Kurtenbach, R., et al., *Investigations of emissions and heterogeneous formation of HONO in a road traffic tunnel*. Atmospheric Environment, 2001. **35**(20): p. 3385-3394.

12. Platt, U., et al., *Observations of Nitrous-Acid in an Urban Atmosphere by Differential Optical-Absorption*. Nature, 1980. **285**(5763): p. 312-314.

13. Li, Y.Q., J.J. Schwab, and K.L. Demerjian, *Fast time response measurements of gaseous nitrous acid using a tunable diode laser absorption spectrometer: HONO emission source from vehicle exhausts*. Geophysical Research Letters, 2008. **35**(4): p. -.

14. Schiller, C.L., et al., *Atmospheric measurements of HONO by tunable diode laser absorption spectroscopy*. Journal of Atmospheric Chemistry, 2001. **40**(3): p. 275-293.

15. Horii, C.V., et al., *Fluxes of nitrogen oxides over a temperate deciduous forest*. Journal of Geophysical Research-Atmospheres, 2004. **109**(D8): p. -.

16. Horii, C.V., et al., *Atmospheric reactive nitrogen concentration and flux budgets at a Northeastern US forest site*. Agricultural and Forest Meteorology, 2005. **133**(1-4): p. 210-225.

17. Horii, C.V., et al., *Nitric Acid and Nitrogen Dioxide Flux Measurements: a new Application of Tunable Diode Laser Absorption Spectroscopy*. Proceedings of SPIE, 1999. **3758**: p. 152-161.

18. Rothman, L.S., et al., *The HITRAN 2004 molecular spectroscopic database*. Journal of Quantitative Spectroscopy & Radiative Transfer, 2005. **96**(2): p. 139-204.

19. McManus, J.B., *Paraxial matrix description of astigmatic and cylindrical mirror resonators with twisted axes for laser spectroscopy*. Applied Optics, 2007. **46**(4): p. 472-482.

20. McManus, J.B., et al., *Comparison of cw and pulsed operation with a TE-cooled quantum cascade infrared laser for detection of nitric oxide at 1900 cm(-1)*. Applied Physics B-Lasers and Optics, 2006. **85**(2-3): p. 235-241.

21. Nelson, D.D., et al., *Sub-part-per-billion detection of nitric oxide in air using a thermoelectrically cooled mid-infrared quantum cascade laser spectrometer*. Applied Physics B-Lasers and Optics, 2002. **75**(2-3): p. 343-350.

22. Zahniser, M.S., et al., *Infrared QC laser applications to field measurements of atmospheric trace gas sources and sinks in environmental research: enhanced capabilities using continuous wave QCLs*. Proceedings of SPIE, 2009. **7222, 72220H**.

23. Febo, A., et al., *Evaluation of a High-Purity and High-Stability Continuous Generation System for Nitrous-Acid*. Environmental Science & Technology, 1995. **29**(9): p. 2390-2395.

24. Bongartz, A., et al., *Near-Uv Absorption Cross-Sections and Trans Cis Equilibrium of Nitrous-Acid*. Journal of Physical Chemistry, 1991. **95**(3): p. 1076-1082.

25. Jones, L.H., R.M. Badger, and G.E. Moore, *The Infrared Spectrum and the Structure of Gaseous Nitrous Acid*. Journal of Chemical Physics, 1951. **19**(12): p. 1599-1604.

26. Mcgraw, G.E., D.L. Bernitt, and Hisatsun.Ic, *Infrared Spectra of Isotopic Nitrous Acids*. Journal of Chemical Physics, 1966. **45**(5): p. 1392-&.

27. Sironneau, V., et al., *Absolute line intensities of HONO and DONO in the far-infrared and re-determination of the energy difference between the trans- and cis-species of nitrous acid*. Journal of Molecular Spectroscopy, 2010. **259**(2): p. 100-104.

28. Varma, R. and R.F. Curl, *Study of N2o3-H2o-Hno2 Equilibrium by Intensity Measurements in Microwave Spectroscopy*. Journal of Physical Chemistry, 1976. **80**(4): p. 402-409.

29. Becker, K.H., et al., *Solubility of nitrous acid (HONO) in sulfuric acid solutions*. Journal of Physical Chemistry, 1996. **100**(36): p. 14984-14990.

30. Chameides, W.L., *The Photochemistry of a Remote Marine Stratiform Cloud*. Journal of Geophysical Research-Atmospheres, 1984. **89**(Nd3): p. 4739-4755.

31. Goretski, J., O.C. Zafiriou, and T.C. Hollocher, *Steady-State Nitric-Oxide Concentrations during Denitrification*. Journal of Biological Chemistry, 1990. **265**(20): p. 11535-11538.

32. Lelieveld, J. and P.J. Crutzen, *The Role of Clouds in Tropospheric Photochemistry*. Journal of Atmospheric Chemistry, 1991. **12**(3): p. 229-267.

33. Zhou, X.L., et al., *Photochemical production of nitrous acid on glass sample manifold surface*. Geophysical Research Letters, 2002. **29**(14): p. -.

34. Loo, B.W. and C.P. Cork, *Development of High-Efficiency Virtual Impactors*. Aerosol Science and Technology, 1988. **9**(3): p. 167-176.

35. Marple, V.A. and C.M. Chien, *Virtual Impactors - a Theoretical-Study*. Environmental Science & Technology, 1980. **14**(8): p. 976-985.

36. Ellis, R.A., et al., *Characterizing a Quantum Cascade Tunable Infrared Laser Differential Absorption Spectrometer (QC-TILDAS) for measurements of atmospheric ammonia*. Atmospheric Measurement Techniques, 2010. **3**: p. 397-406.

37. Herndon, S.C., et al., *Airborne measurements of HCHO and HCOOH during the New England Air Quality Study 2004 using a pulsed quantum cascade laser spectrometer*. Journal of Geophysical Research-Atmospheres, 2007. **112**(D10): p. -.

38. McManus, J.B., et al., *Application of quantum cascade lasers to high precision atmospheric trace gas measurements*. Optical Engineering, 2010. **49**(11).

Chapter 3:

Measurements of nitrous acid in commercial aircraft exhaust at the Alternative Aviation Fuel Experiment[2]

Abstract

The Alternative Aviation Fuel Experiment (AAFEX), conducted in January of 2009 in Palmdale, California quantified aerosol and gaseous emissions from a DC-8 aircraft equipped with CFM56-2C1 engines using both traditional and synthetic fuels. This study examines the emissions of nitrous acid (HONO) and nitrogen oxides (NO_x=NO+NO_2) measured 145 m behind the grounded aircraft. The fuel-based emission index (EI) for HONO increases approximately six-fold from idle to take-off conditions, but plateaus between 65% and 100% of maximum rated engine thrust, while the EI for NO_x increases continuously. At high engine power, NO_x EI is greater when combusting traditional (JP-8) than Fischer-Tropsch fuels, while HONO exhibits the opposite trend. Additionally, hydrogen peroxide (H_2O_2) was identified in exhaust plumes emitted only during engine idle. Chemical reactions responsible for emissions and comparison to previous measurement studies are discussed.

3.1. Introduction

The effects of aircraft exhaust on air quality and climate are a growing concern given the projected global increase in air travel over the coming decades. Uncertainties associated with induced indirect effects related to microphysical processes and heterogeneous chemistry have

[2] Lee, B. H., G. W. Santoni, E. C. Wood, S. C. Herndon, R. C. Miake-Lye, M. S. Zahniser, S. C. Wofsy, J. W. Munger (2011), *Environ. Sci. & Technol.*, **45**, 7648-7654, doi:10.1021/es200921t.

been the focus of numerous previous studies [1-4], which stress among others the importance of characterizing emissions and their driving factors to evaluate the influence of the aviation transportation sector on chemistry, radiative forcing and public health.

Nitrous acid (HONO) is the primary reservoir of hydroxyl radicals (OH) emitted in fresh jet exhaust [5, 6]. HONO during daytime undergoes rapid photolysis, yielding OH, which initiates the oxidation of simultaneously emitted nitrogen oxides (NO_x=NO+NO_2), sulfur dioxide (SO_2) and volatile organic compounds (VOCs). Heterogeneous chemistry on the surface of aircraft-generated particles can further shift the partitioning of in-plume NO_x towards NO_y (=NO_x+HNO_3+HONO+…), altering the impact of emission on ozone (O_3) levels at altitude [7]. Moreover, enhanced reactivity in exhaust from idling and taxiing aircraft adversely affects air quality in and around airports [8]. HONO itself is a lung irritant and reacts with amines to form carcinogenic compounds [9-11].

Fischer-Tropsch (FT) fuels, despite high energy costs of production, have gained much attention as a viable alternative to imported oil because the main feedstocks are readily available (e.g. coal, natural gas and bio-oils). In addition, FT-derived fuels do not contain aromatic-hydrocarbon and sulfur compounds, resulting in emissions that are typically lower in soot and sulfate aerosols. A recent study observed lower NO and higher NO_2 emissions in FT-derived exhaust compared to those combusting traditional JP-8 fuel [12]. Simultaneous measurements of NO_x and HONO during AAFEX provided an opportunity to further investigate fuel-type dependence of nitrogen oxide emissions from jet engines. We present fuel-based emission indices of HONO, NO_x and hydrogen peroxide (H_2O_2) emitted from CFM56-2C1 commercial aircraft engines as a function of engine power.

3.2. Methods

During AAFEX, a DC-8 was chocked on the runway at NASA's Dryden Aircraft Operation Facility in Palmdale, California. Two of its four engines (one on each side) were fired for twelve experiments – each typically lasting a few hours – during which the rated engine thrust was varied to simulate idle to take-off conditions. The left (control) inboard engine was supplied with traditional JP-8 fuel, while the right (experiment) alternated between traditional, two different Fischer-Tropsch fuels and blends of both. JP-8 fuel – utilized by the military – contains additives to enhance lubrication/inhibit icing that are not present in Jet A-1 fuel – most commonly used in commercial aviation – but exhibit similar combustion emission properties [13]. Experiments were conducted from before sunrise to late afternoon over a span of eight days to test the impact of the wide range in ambient conditions on emission characteristics. Composition and mixing ratios of particles and various trace gases were measured 1 and 30 m behind both engines and at a distance of 145 m in-line with the right inboard engine relative to the direction of the aircraft. This downstream location observed a mixture of naturally diluted and cooled exhaust from both engines and is the focus of the present study. Table 1 lists a brief description of the experimental conditions, with fuller details given by *Bulzan et al*. [14].

Mixing ratios of HONO, H_2O_2, nitrous oxide (N_2O) and methane (CH_4) were measured simultaneously by a tunable infrared laser differential absorption spectrometer (TILDAS) utilizing a continuous-wave quantum cascade laser (Alpes Lasers) operating near the 8 mm (1275 cm^{-1}) spectral region. Infrared light from the laser is directed into a multi-pass sample cell where the laser light reflects 238 times between two astigmatic high-reflectivity (R=0.993) mirrors spaced 0.88 m apart to achieve a total absorption path-length of 210 m. Light exits the sample cell and is directed onto a cryogenically-cooled HgCdTe detector (Vigo). An absorbance

Experiment no.	Date	Fuel‡	Ambient temperature (°C)	Relative humidity (%)
1	Jan. 26	JP-8	5	60
2	Jan. 27	JP-8	10	30
3	Jan. 28	JP-8	-3	30
4	Jan. 28	FT1	10	30
5	Jan. 29	FT1	0	60
6	Jan. 30	FT1‡‡	2	55
7	Jan. 30	FT2	14	25
8	Jan. 31	FT2	0	75
9	Jan. 31	FT2‡‡	14	30
10	Jan. 31	JP-8	17	20
11	Feb. 2	JP-8	2	60
12	Feb. 2	JP-8	12	25

Table 3.1. Fuel used, average ambient temperature and relative humidity for each experiment during AAFEX.

‡ Fuel utilized by the right inboard engine. The left inboard engine powered by JP-8 for all experiments. FT1 derived from natural gas. FT2 derived from coal.

‡‡ Right inboard engine fueled with 50/50 mixture by volume of JP-8/FT blend.

precision less than 6×10^{-6} $Hz^{-1/2}$ in one second was achieved in the field, which translated to detection limits (S/N = 3) of 450 ppt (pmol/mol), 1,200 ppt and 900 ppt for HONO, H_2O_2 and N_2O, respectively, in one second. Figure 1 shows typical one-second spectra observed while sampling plumes emitted during 7% (a, b) and 85% (c, d) of maximum rated engine thrust.

Special attention was paid to the sample handling to minimize HONO loss and artifact formation on instrument surfaces. Sample air – a variable mixture of exhaust and background air – was continuously pulled through a quartz inlet (length approx. 6 inches (15.2 cm); inner diameter approx. 0.25 inch (6.4 mm)), which was treated with siloxyl coating and shielded from sunlight to reduce surface chemistry. The sample subsequently passed through a critical orifice (0.04 inch diameter (1.0 mm)), to accelerate the flow and reduce the pressure, then diverged in two paths – a vent-flow parallel and sample-flow perpendicular to the direction of flow through the orifice. Inertial separation prevented coarse particles with diameters greater than about 4 μm from entering the sample cell [15]. This design was utilized instead of a particle filter, which would present a large surface area where loss or production of "sticky" gases could occur. The sample then traveled through approximately 40 feet (12.2 m) of 3/8'' (9.5 mm) outer diameter PFA tubing to the siloxyl-coated multi-pass sample cell in which the pressure was maintained at approximately 30 torr. With a total flow-rate of about 10 standard liters per minute (SLPM) the sample residence times (1/e) in the inlet, tubing and cell were on average 0.3, 0.2 and 1.2 seconds, respectively. Additional details regarding the instrumentation and sampling schemes are provided elsewhere [15]. Results for N_2O and CH_4, measured by a second TILDAS instrument connected in series with this system are presented by *Santoni et al.* [16].

Introduction of air infused with HONO and CH_4 at the end of the eight-day campaign showed indistinguishable response times between the two gases (Supporting Information, figure B1),

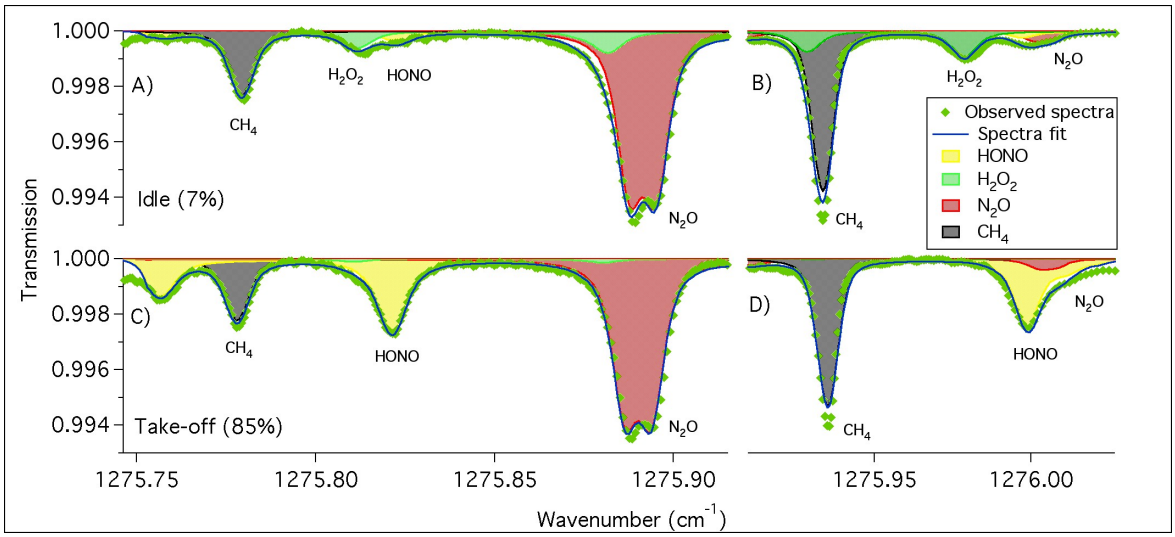

Figure 3.1. One-second spectra observed in aircraft exhaust emitted during 7% (a, b) and 85% (c, d) rated engine thrust. The above snapshots at idle and take-off conditions represent CH_4, N_2O, HONO and H_2O_2 values of 2000, 335, 10, 35 ppb and 1875, 325, 75, 5 ppb, respectively. For most of AAFEX, the spectral window shown in a) and c) was scanned, save for one day (experiment no. 11 & 12) when the window in b) and d) was scanned. The filled-in color areas are simulations of the retrieved mixing ratios.

indicating no reversible loss of HONO on the inlet/tubing/cell surfaces. Laboratory tests prior to deployment that compared the signal of HONO standard introduced through the sampling inlet/tubing to the signal when HONO was introduced directly into the cell demonstrated no detectable loss of HONO on inlet/tubing walls. However, the same addition tests under field conditions could not be repeated during the experiments. Similar tests for H_2O_2 were not conducted because a steady source was not available in the field. Though the reduced pressure in the sample line and use of hydrophobic siloxyl coating minimize water activity on surfaces, we cannot discount the potential for loss of H_2O_2 given that the Henry's law constant for H_2O_2 is 82,000 M atm^{-1} compared to 50 M atm^{-1} for HONO [17, 18]. In addition, spectral overlap between HONO and H_2O_2 absorption lines around 1275.82 cm^{-1} (figure 1a, 1c) during experiments 1-10 (table 1) resulted in artificial enhancement of the retrieved H_2O_2 mixing ratios in the presence of high HONO. This was not observed when H_2O_2 was scanned near the 1275.98 cm^{-1} region (figure 1b, 1d), where its absorption lines were free of overlap. As a result, H_2O_2 data from only experiments 11 and 12 are reported. In-field additions of high levels of H_2O_2 showed no significant influence by H_2O_2 on calculated HONO mixing ratios.

Calibrations with a constant HONO source were not possible in the field. Instead, measurements relied on the accuracy of absorption line strengths. Line positions and relative line strengths for HONO were initially obtained from high-resolution FTIR spectra provided by *Herman et al*. [19-21]. Absolute values were derived in the laboratory by measuring the absorbance of a high-purity HONO source with the TILDAS system. Total HONO in the generated source was simultaneously converted via molybdenum (Mo) catalysis to NO followed by quantification with a second calibrated TILDAS system [22]. We found that the previous

aircraft emission study by *Wood et al*. [23] used incorrect line strength values that resulted in measurements of HONO to be low by a factor of approximately 2.4 (discussed below). Absorption parameters for H_2O_2, CH_4 and N_2O are obtained from the HITRAN database [24].

The NO_x mixing ratio – the sum of NO and NO_2 – was measured using Mo-catalysis ozone chemiluminescence (ThermoElectron 42i). The Mo catalyst converts other species besides NO_2, but because the converter was preceded by a particle filter and 40 ft of tubing maintained near ambient pressure, it is unlikely that reducible NO_y species such as HONO and HNO_3 were transmitted. Mixing ratios of CO_2 were measured using a non-dispersive infrared absorption spectrometer (Li-Cor 6262). The flow-rate was approximately 0.5 SLPM for each of these two instruments connected in parallel to tubing dedicated to NO_x and CO_2 measurements, resulting in sample residence times (1/e) of less than one second in each instrument.

To derive emission indices we compute slopes from linear regression of each species against CO_2 and convert to a fuel-based emission index (g of species per kg of fuel consumed) by scaling with the emission index for CO_2 (carbon content of the fuel). Regression slopes provide a more robust estimate of EI, with associated uncertainty, in downwind plumes with highly variable mixing ratios than the background-subtracted ratio of the average mixing ratio to CO_2 [25]. Note that the EI for HONO and H_2O_2 are scaled by their respective molecular masses, while EI for NO_x is reported using the molecular mass of NO_2.

$$EI_x = m_{x,CO_2} \times \frac{M_x}{M_{CO_2}} \times EI_{CO_2},$$

where EI_x is emission index of species *x* (g of *x* per kg fuel), $m_{X,CO2}$ is slope of the linear regression between species *x* and CO_2, M is molecular weight (g of *x* per mole of *x*) and EI_{CO2} is

g of CO_2 emitted per kg fuel consumed determined for each fuel-type by C/H fuel analysis [14]. The analyses presented here utilize a single EI_{CO2} value for all experiments because the extent of mixing of exhaust from the two engines was unknown.

Figure 2 (a, b) shows a brief 1 hertz time-series of HONO, NO_x, H_2O_2 and CO_2 mixing ratios. All gases co-vary in time. This is also reflected in the correlation of that same plume of HONO, NO_x and H_2O_2 versus CO_2 mixing ratio (figure 2c). The mean uncertainty in the emission indices – determined as the standard error of the regressed slopes – for HONO, NO_x and H_2O_2 are 0.03, 0.4 and 0.01 g kg^{-1}, respectively, which are about a factor of three less than the observed plume-to-plume variability as seen in figure 3.

3.3. Results and Discussion

3.3.1 HONO and NO_x EI – chemistry and fuel dependence

Figure 3 (a, b) shows the emission indices for NO_x and HONO plotted as a function of the percentage of maximum rated engine thrust. The EI for NO_x – driven primarily by the Zeldovich reactions [26] – increases continuously with engine thrust, hence gas temperature during combustion. The EI for HONO in comparison levels off between 65% and 100% engine setting, an unexpected trend assuming OH production – presumably from the reaction between water vapor and $O(^1D)$ in the combustor – also increases continuously with engine power. Thermal decomposition (R_{-1}) alone may explain the flattening of HONO EI above 65% of rated engine thrust as proposed by *Wood et al.*, however, that HONO production is also underestimated at low engine power points to missing reactions and/or inaccurate kinetic constants [23]. Notably, published values for HONO self-reaction rate (R_4) differ by six orders of magnitude [27].

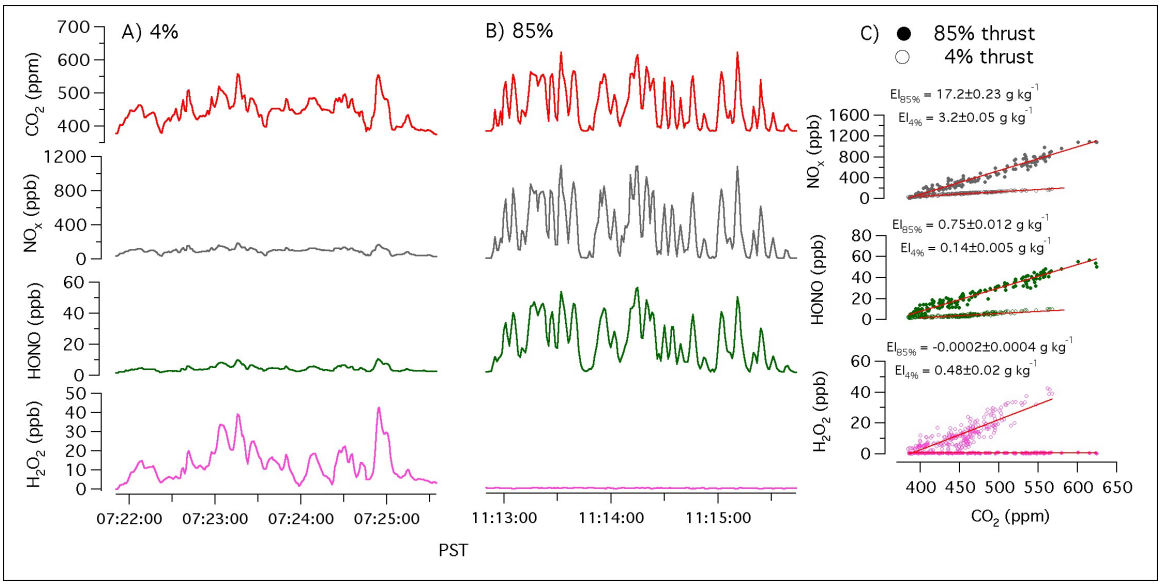

Figure 3.2. Mixing ratios of CO_2, NO_x, HONO and H_2O_2 measured 145 m downwind of the aircraft in plumes emitted during 4% (a) and 85% (b) rated engine thrust. Correlation plots (c) of NO_x, HONO and H_2O_2 versus CO_2 for the same time periods from (a) and (b), along with corresponding emission indices and standard errors.

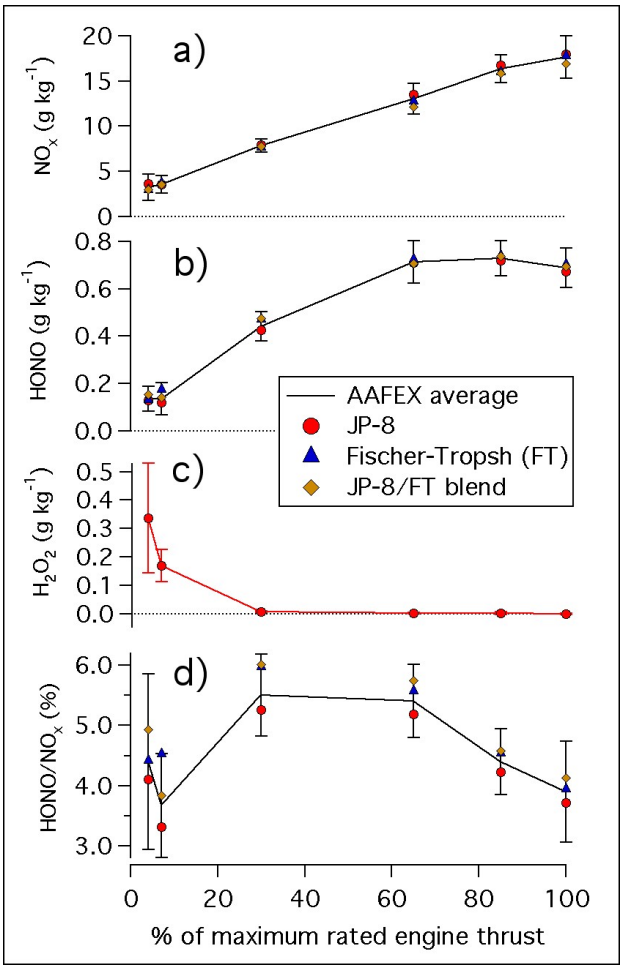

Figure 3.3. Emission indices (EI = g per kg of fuel) of NO_x (a), HONO (b) and H_2O_2 (c) plotted against % of maximum rated engine thrust, along with HONO to NO_x ratio (d). Each symbol represents the fuel-experiment average while the black trace is the campaign average ± one standard deviation of the mean at each engine power, except for c) which shows results for JP-8 fuel experiments 11 and 12 only.

R_1) $NO + OH + M \leftrightarrow HONO + M$

R_2) $NO_2 + HO_2 \rightarrow HONO + OH$

R_3) $HONO + OH \rightarrow H_2O + NO_2$

R_4) $HONO + HONO \rightarrow H_2O + NO + NO_2$

Ab-initio calculation by *Xia and Lin* of reaction rate R_3 reveals a change from negative to positive temperature dependence above 1000 K [28], which is consistent with our observed trend in HONO EI as the rate of HONO loss by OH becomes significant with increasing combustion temperature and OH levels. Though targeted measurements of NO_2 – the product of reaction R_3 – were not made during AAFEX, results from a previous campaign Aircraft Particle Experiment-3 (APEX-3) show an increase in NO_2 EI at high engine power (figure 4). Underestimation of reaction R_3 in previous studies may also help reconcile the large discrepancy between engine exit OH levels predicted at cruise (9.0-13.2 ppm) [6] and observed under take-off conditions (90 ppb) [29]. Self-reaction of OH is ruled out because modeling studies [6, 30] report near-complete titration of OH by excess NO, and because this reaction would result in the production of H_2O_2, which was not observed at high engine power (discussed below). Heterogeneous chemistry, as well, plays a small role [31].

A weak fuel-type dependence was observed for NO_x, which on average exhibited lower EI values during FT and FT-blend versus JP-8 fuel combustion experiments (table 2). This is consistent with measurements made near engine exit at AAFEX and in a previous study in which NO_x EI values were 5-11% lower in FT-derived exhaust [12, 32]. Table 2 summarizes the JP-8 normalized emission indices of NO_x and HONO for FT/FT-blend experiments. Note that a bias is introduced for these experiments because a constant non-fuel-type specific EI_{CO2} value is used

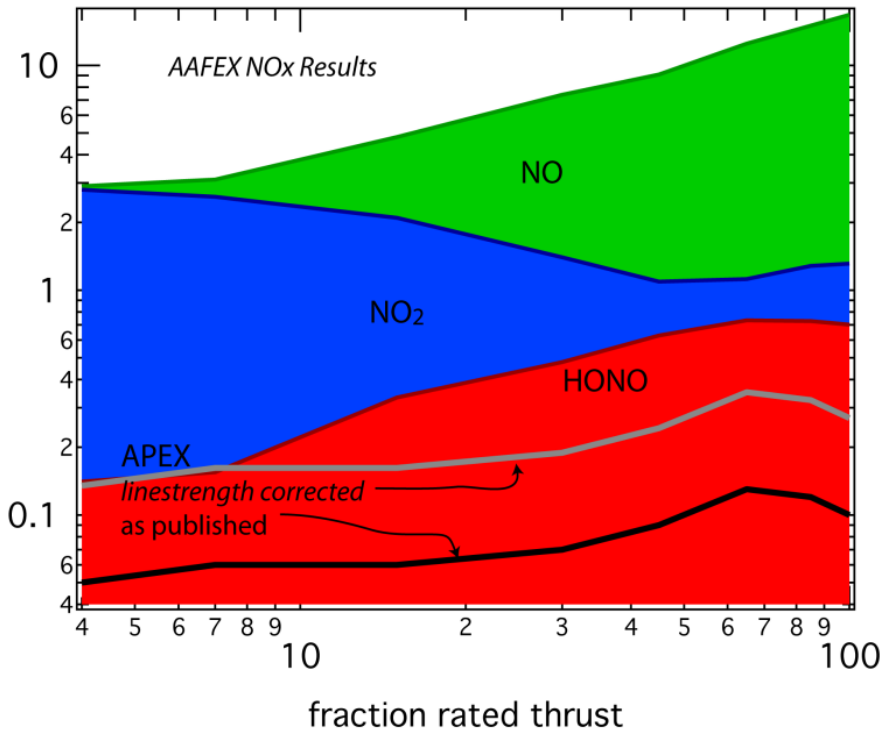

Figure 3.4. Emission index of HONO observed during the APEX-3 (black line). Revised APEX-3 values (grey line) using corrected line strength values overlaid on top of observations from AAFEX (red). Emission indices for NO_2 (blue) and NO (green) from APEX-3 are shown as well.

		4% (low)	7% (idle)	30% (approach)	65% (cruise)	85% (climb-out)	100% (takeoff)
NO_x	FT	0.82	1.03	0.97	0.95	0.96	0.99
	blend	0.83	0.99	0.98	0.90	0.95	0.94
HONO	FT	1.02	1.45	1.10	1.02	1.03	1.04
	blend	1.20	1.17	1.16	1.00	1.02	1.03

Table 3.2. NO_x and HONO emission indices for FT and blended fuel experiments normalized by those for JP-8.

since we do not know the relative contribution of exhaust from each engine measured at 145 m. This can account for at most 2% of the EI difference in the extreme case that exhaust from only the "experiment" engine was sampled during FT experiments. Moreover, we at times observe lower NO_x EI for FT-blend than FT-only experiments, though we expect FT-blend values to be an average of the JP-8 and FT [12]. Ambient conditions that affect engine chemistry and measurement downstream including temperature, humidity, sunlight, transport time from emission to sampling and the extent of the mixing of exhaust from the two engines could not be adjusted in a controlled manner, complicating direct comparisons between experiments.

HONO showed a fuel-type dependence opposite to that of NO_x (table 2), which cannot be attributed to the use of a constant EI_{CO2}. *Timko et al*. [12] observed lower NO and higher NO_2 EI in FT-derived plumes compared to those utilizing only JP-8 fuel. That NO_2 and HONO – both byproducts of reactions involving NO – exhibit a fuel-type dependence trend that is opposite to that of NO indicates an environment that is more favorable to oxidation during FT-fuel combustion, perhaps a result of the absence of aromatics and sulfur compounds. Future experiments with speciated measurements of individual nitrogen oxide species under identical ambient conditions are required to determine whether the total amount of NO_y produced or only the partitioning between species is affected by the use of synthetic fuels.

NO_x EI exhibit a positive dependence on ambient temperature (0.19 ± 0.04 g kg^{-1} K^{-1}) at the maximum rated engine thrust (Figure B2), consistent with the ICAO database [33]. A temperature dependence for HONO was not observed (Figure B2), suggesting the chemical processes governing HONO production and loss are not sensitive to ambient temperatures.

3.3.2. Comparison to previous campaigns

HONO EI trend with increasing engine power observed during AAFEX is consistent with those from previous field campaigns [23, 34]. Figure 4 shows good agreement at low engine power between HONO EI from AAFEX to those observed at the APEX-3 (using corrected line strengths), during which HONO was measured 1 m behind engine exit [23]. HONO EI from APEX-3 was lower by a factor of approximately three at higher engine thrust. The discrepancy may simply be explained by difference in engine type and age, both of which can influence aircraft NO_x emissions [35]. However, because results agree well under some engine conditions but not others (figure 4), a more likely explanation is incomplete HONO formation during APEX-3. *Tremmel et al*. [6] simulate HONO formation via R_1 continuing for several milliseconds following engine exit, therefore, at higher engine power (i.e. higher exhaust velocity), HONO formation may not be complete at a distance of 1 m downstream as the remaining OH is quenched by the inlet probe. Consequently, HONO measured at 1 m may underestimate total production, suggesting sampling of reactive gases should be conducted farther downstream to ensure completion. Metal probes used to sample hot exhaust near engine exit and heating/dilution to prevent condensation in inlet lines during APEX-3 may have promoted HONO surface losses or thermal dissociation leading to underestimation of HONO.

Figure 3d shows HONO to NO_x ratios observed during AAFEX ranging from 3-6%, which is consistent with predicted value of 4.5% in jet engine exhaust [30] and considerably higher than 0.29-0.8% reported for on-road vehicles, with diesel-powered engines emitting a higher ratio than their gasoline-powered counterparts [36, 37]. Sampling exhaust from a diesel-powered generator during AAFEX revealed HONO/NO_x of 0.82±0.05% (figure B3). Lastly, recent measurements of exhaust from 8 different commercial aircraft in flight [38] show decreasing

HONO/NO_y with increasing NO_x EI, as also observed during AAFEX for engine settings simulating cruise conditions (~65% maximum rated engine thrust) and beyond.

3.3.3. H_2O_2 chemistry

Hydrogen peroxide was detected in aircraft exhaust only at low/idle engine power. H_2O_2 EI for JP-8 fuel at low power (4%) is 0.34±0.19 (1σ) g per kg fuel and decreases to below detection limit beyond 30% of maximum rated engine thrust. EI for H_2O_2 exhibits no dependence on ambient temperature. During combustion H_2O_2 can be formed by the self-reactions of HO_2 (R_5) and OH (R_6). The H_2O_2 EI trend with respect to rated engine thrust reflects that of NO_2 (figure 4), which *Wood et al*. [23] proposed is primarily generated during combustion by reaction involving HO_2 (R_7) and exhibits the opposite trend of HONO, formed primarily by reaction involving OH (R_1). Therefore, HO_2 by reaction R_6 and not OH by reaction R_5 is the likely H_2O_2 precursor in jet-fuel combustion. HO_2 is likely formed from the OH-driven oxidation of incomplete combustion byproducts such as carbon monoxide and formaldehyde, both of which exhibit EI trends similar to that of H_2O_2 [39].

R_5) $\quad OH + OH + M \rightarrow H_2O_2$

R_6) $\quad HO_2 + HO_2 + M \rightarrow H_2O_2 + O_2$

R_7) $\quad HO_2 + NO \rightarrow NO_2 + OH$

Identification of H_2O_2 at levels comparable to those of HONO (figure 2) at low engine thrust represents an additional airport-related source of HO_x precursors to the boundary layer, though given its slow rate of photolysis and loss via deposition its impact on the HO_x budget is likely to

be much smaller than that of HONO. Though this was the first spectroscopic measurement of H_2O_2 in aircraft exhaust, the reported values for H_2O_2 from AAFEX should be qualified because of the yet uncharacterized potential for attenuation during sampling.

3.3.4 Impact on atmospheric chemistry

Emission indices of HONO observed during AAFEX are higher than those previously reported [23, 34]. We calculate photolysis of idle-aircraft-emitted HONO at engine exit will yield OH at a rate of about 1000 ppt sec^{-1}, which is roughly three orders of magnitude faster than observed in a typical sunny urban atmosphere. With increasing engine power (at higher altitudes), HONO goes from a dominant to nearly sole source of HO_x in jet exhaust [40], which can influence photochemistry in heavily traveled flight corridors. Consequently, HO_x precursors emitted simultaneously with pollutants of interest should be included in models aimed at understanding the evolution of plumes from emission sources, particularly given the non-linearity and cycling of NO_x-HO_x chemistry prior to termination. Moreover, reported discrepancies on the potential significance of ClNO production [41-43] – a driver of catalytic stratospheric ozone destruction – due to HONO and HCl uptake on the surface of H_2SO_4 aerosols require more information of, among other variables, HONO levels in aircraft exhaust. This study characterizing emission indices as a function of engine power, ambient conditions and fuel-type – in addition to gaining insight into engine chemistry – provides a useful tool for such applications.

Acknowledgements

This research was supported in part by the National Science Foundation (Awards No. AGS – 0813617 and 0814202). The authors gratefully acknowledge W. Berk Knighton of Montana State

University, Michael T. Timko and Zhenhong Yu of Aerodyne Research, Inc., Bruce E. Anderson of NASA Langley Research Center and all of the support staff and scientists of the AAFEX team.

Supporting Information Available

The supporting information section includes three figures showing, 1) the response times of HONO and CH_4 during a standard addition test in the field at the end of the AAFEX campaign, 2) temperature dependence of NO_x and HONO emission indices at high engine power, and 3) the HONO to NO_x ratio measured in diesel-generated exhaust at AAFEX. This information is available free of charge via the Internet at http://pubs.acs.org/.

References

1. Brasseur, G. P.; Cox, R. A.; Hauglustaine, D.; I, I.; Lelieveld, J.; Lister, D. H.; Sausen, R.; Schumann, U.; Wahner, A.; Wiesen, P., European scientific assessment of the atmospheric effects of aircraft emissions. *Atmospheric Environment* **1998,** *32*, (13), 2329-2418.

2. National Research Council (U.S.). Panel on Atmospheric Effects of Aviation., *Atmospheric effects of aviation : a review of NASA's subsonic assessment project*. National Academy Press: Washington, D.C., 1999; p xii, 41 p.

3. National Research Council (U.S.). Panel on Atmospheric Effects of Aviation., *A review of NASA's atmospheric effects of stratospheric aircraft project*. National Academy Press: Washington, D.C., 1999; p ix, 50 p.

4. Toohey, D.; McConnell, J.; Avallone, L.; Evans, W., Aviation and Chemistry and Transport Processes in the Upper Troposphere and Lower Stratosphere. *Bulletin of the American Meteorological Society* **2010,** *91*, (4), 485-+.

5. Beier, K.; Schreier, F., Modeling of Aircraft Exhaust Emissions and Infrared-Spectra for Remote Measurement of Nitrogen-Oxides. *Annales Geophysicae-Atmospheres Hydrospheres and Space Sciences* **1994,** *12*, (10-11), 920-943.

6. Tremmel, H. G.; Schlager, H.; Konopka, P.; Schulte, P.; Arnold, F.; Klemm, M.; Droste-Franke, B., Observations and model calculations of jet aircraft exhaust products at cruise altitude and inferred initial OH emissions. *Journal of Geophysical Research-Atmospheres* **1998,** *103*, (D9), 10803-10816.

7. Sovde, O. A.; Gauss, M.; Isaksen, I. S. A.; Pitari, G.; Marizy, C., Aircraft pollution - a futuristic view. *Atmospheric Chemistry and Physics* **2007,** *7*, (13), 3621-3632.

8. Tesseraux, I., Risk factors of jet fuel combustion products. *Toxicology Letters* **2004,** *149*, (1-3), 295-300.

9. Jarvis, D. L.; Leaderer, B. P.; Chinn, S.; Burney, P. G., Indoor nitrous acid and respiratory symptoms and lung function in adults. *Thorax* **2005,** *60*, (6), 474-479.

10. Pitts, J. N.; Grosjean, D.; Vancauwenberghe, K.; Schmid, J. P.; Fitz, D. R., Photo-Oxidation of Aliphatic-Amines under Simulated Atmospheric Conditions - Formation of Nitrosamines, Nitramines, Amides, and Photo-Chemical Oxidant. *Environmental Science & Technology* **1978,** *12*, (8), 946-953.

11. Sleiman, M.; Gundel, L. A.; Pankow, J. F.; Jacob, P.; Singer, B. C.; Destaillats, H., Formation of carcinogens indoors by surface-mediated reactions of nicotine with nitrous acid, leading to potential thirdhand smoke hazards. *Proceedings of the National Academy of Sciences of the United States of America* **2010,** *107*, (15), 6576-6581.

12. Timko, M. T.; Yu, Z.; Onasch, T. B.; Wong, H. W.; Miake-Lye, R. C.; Beyersdorf, A. J.; Anderson, B. E.; Thornhill, K. L.; Winstead, E. L.; Corporan, E.; DeWitt, M. J.; Klingshirn, C. D.; Wey, C.; Tacina, K.; Liscinsky, D. S.; Howard, R.; Bhargava, A., Particulate Emissions of Gas Turbine Engine Combustion of a Fischer-Tropsch Synthetic Fuel. *Energy & Fuels* **2010,** *24*, 5883-5896.

13. Miller, D. L.; Lenhert, D. B.; Cernansky, N. P., The oxidation of JP-8, Jet-A, and their surrogates in the low and intermediate temperature regime at elevated pressures. *Combustion Science and Technology* **2007,** *179*, (5), 845-861.

14. Bulzan, D.; Anderson, B.; Wey, C.; Howard, R.; Winstead, E. H.; Beyersdorf, A.; Corporan, E.; DeWitt, M. J.; Klingshirn, C. D.; Herndon, S. C.; Miake-Lye, R.; Wood, E. C.; Tacina, K.; Liscinsky, D. S.; Hagen, D.; Lobo, P.; Whitefield, P. In *Gaseous and Particulate Emissions Results of the NASA Alternative Aviation Fuel Experiment (AAFEX)*, ASME Turbo Expo 2010: Power for Land, Sea, and Air (GT2010), Glasgow, UK, June 14-18, 2010, 2010; ASME: Glasgow, UK, 2010; pp 1195-1207.

15. Lee, B. H.; Wood, E. C.; Zahniser, M. S.; McManus, J. B.; Nelson, D. D.; Herndon, S. C.; Santoni, G. W.; Wofsy, S. C.; Munger, J. W., Simultaneous measurements of atmospheric HONO and NO2 via absorption spectroscopy using tunable mid-infrared continuous-wave quantum cascade lasers. *Applied Physics B-Lasers and Optics* **2011,** *102*, (2), 417-423.

16. Santoni, G. W.; Lee, B. H.; Wood, E. C.; Herndon, S. C.; Miake-Lye, R. C.; Wofsy, S. C.; McManus, J. B.; Nelson, D. D.; Zahniser, M. S., Aircraft Emissions of Methane and Nitrous Oxide during the Alternative Aviation Fuel Experiment. *Environmental Science & Technology*, accepted, **2011**.

17. Becker, K. H.; Kleffmann, J.; Kurtenbach, R.; Wiesen, P., Solubility of nitrous acid (HONO) in sulfuric acid solutions. *Journal of Physical Chemistry* **1996,** *100*, (36), 14984-14990.

18. OSullivan, D. W.; Lee, M. Y.; Noone, B. C.; Heikes, B. G., Henry's law constant determinations for hydrogen peroxide, methyl hydroperoxide, hydroxymethyl hydroperoxide, ethyl hydroperoxide, and peroxyacetic acid. *Journal of Physical Chemistry* **1996,** *100*, (8), 3241-3247.

19. Guilmot, J. M.; Godefroid, M.; Herman, M., Rovibrational Parameters for Trans-Nitrous Acid. *Journal of Molecular Spectroscopy* **1993,** *160*, (2), 387-400.

20. Guilmot, J. M.; Melen, F.; Herman, M., Rovibrational Parameters for Cis-Nitrous Acid. *Journal of Molecular Spectroscopy* **1993,** *160*, (2), 401-410.

21. Melen, F.; Herman, M., Vibrational Bands of Hxnyoz Molecules. *Journal of Physical and Chemical Reference Data* **1992,** *21*, (4), 831-881.

22. Nelson, D. D.; Shorter, J. H.; McManus, J. B.; Zahniser, M. S., Sub-part-per-billion detection of nitric oxide in air using a thermoelectrically cooled mid-infrared quantum cascade laser spectrometer. *Applied Physics B-Lasers and Optics* **2002,** *75*, (2-3), 343-350.

23. Wood, E. C.; Herndon, S. C.; Timko, M. T.; Yelvington, P. E.; Miake-Lye, R. C., Speciation and chemical evolution of nitrogen oxides in aircraft exhaust near airports. *Environmental Science & Technology* **2008,** *42*, (6), 1884-1891.

24. Rothman, L. S.; Gordon, I. E.; Barbe, A.; Benner, D. C.; Bernath, P. E.; Birk, M.; Boudon, V.; Brown, L. R.; Campargue, A.; Champion, J. P.; Chance, K.; Coudert, L. H.; Dana, V.; Devi, V. M.; Fally, S.; Flaud, J. M.; Gamache, R. R.; Goldman, A.; Jacquemart, D.; Kleiner, I.; Lacome, N.; Lafferty, W. J.; Mandin, J. Y.; Massie, S. T.; Mikhailenko, S. N.; Miller, C. E.; Moazzen-Ahmadi, N.; Naumenko, O. V.; Nikitin, A. V.; Orphal, J.; Perevalov, V. I.; Perrin, A.; Predoi-Cross, A.; Rinsland, C. P.; Rotger, M.; Simeckova, M.; Smith, M. A. H.; Sung, K.; Tashkun, S. A.; Tennyson, J.; Toth, R. A.; Vandaele, A. C.; Vander Auwera, J., The HITRAN 2008 molecular spectroscopic database. *Journal of Quantitative Spectroscopy & Radiative Transfer* **2009,** *110*, (9-10), 533-572.

25. Herndon, S. C.; Shorter, J. H.; Zahniser, M. S.; Nelson, D. D.; Jayne, J.; Brown, R. C.; Miake-Lye, R. C.; Waitz, I.; Silva, P.; Lanni, T.; Demerjian, K.; Kolb, C. E., NO and NO2 emission ratios measured from in-use commercial aircraft during taxi and takeoff. *Environmental Science & Technology* **2004,** *38*, (22), 6078-6084.

26. Lavoie, G. A., Spectroscopic Measurements of Nitric Oxide in Spark Ignition Engines. *Combustion and Flame* **1970,** *15*, (2), 97-&.

27. Mebel, A. M.; Lin, M. C.; Melius, C. F., Rate constant of the HONO+HONO -> H2O+NO+NO2 reaction from ab initio MO and TST calculations. *Journal of Physical Chemistry A* **1998,** *102*, (10), 1803-1807.

28. Xia, W. S.; Lin, M. C., Ab initio MO/statistical theory prediction of the OH plus HONO reaction rate: evidence for the negative temperature dependence. *Physchemcomm* **2000**, (1-14), -.

29. Bockle, S.; Einecke, S.; Hildenbrand, F.; Orlemann, C.; Schulz, C.; Wolfrum, J.; Sick, V., Laser-spectroscopic investigation of OH-radical concentrations in the exhaust plane of jet engines. *Geophysical Research Letters* **1999,** *26*, (13), 1849-1852.

30. Garnier, F.; Baudoin, C.; Woods, P.; Louisnard, N., Engine emission alteration in the near field of an aircraft. *Atmospheric Environment* **1997,** *31*, (12), 1767-1781.

31. Brown, L. R.; Farmer, C. B.; Rinsland, C. P.; Toth, R. A., Molecular Line Parameters for the Atmospheric Trace Molecule Spectroscopy Experiment. *Applied Optics* **1987,** *26*, (23), 5154-5182.

32. Timko, M. T.; Herndon, S. C.; De la Rosa Blanco, E.; Wood, E. C.; Yu, Z.; Miake-Lye, R. C.; Knighton, W. B., Combustion Products of Jet Fuel, Fischer Tropsch Synthetic Fuel, and Biomass Jet Fuel for a Gas Turbine Engine. *Combustion Science and Technology*, in review, **2011**.

33. DuBois, D.; Paynter, G. C., Fuel Flow Method2 for Estimating Aircraft Emissions. *Society of Automotive Engineers* **2006**.

34. Wormhoudt, J.; Herndon, S. C.; Yelvington, P. E.; Miake-Lye, R. C.; Wey, C., Nitrogen oxide (NO/NO2/HONO) emissions measurements in aircraft exhausts. *Journal of Propulsion and Power* **2007,** *23*, (5), 906-911.

35. Lukachko, S. P.; Waitz, I. A., Effects of Engine Aging on Aircraft NOx Emissions. In *International Gas Turbine & Aeroengine Congress & Exhibition*, Engineers, A. S. o. M., Ed. Orlando, Florida, 1997.

36. Kirchstetter, T. W.; Harley, R. A.; Littlejohn, D., Measurement of nitrous acid in motor vehicle exhaust. *Environmental Science & Technology* **1996,** *30*, (9), 2843-2849.

37. Kurtenbach, R.; Becker, K. H.; Gomes, J. A. G.; Kleffmann, J.; Lorzer, J. C.; Spittler, M.; Wiesen, P.; Ackermann, R.; Geyer, A.; Platt, U., Investigations of emissions and heterogeneous formation of HONO in a road traffic tunnel. *Atmospheric Environment* **2001,** *35*, (20), 3385-3394.

38. Jurkat, T.; Voigt, C.; Arnold, F.; Schlager, H.; Kleffmann, J.; Aufmhoff, H.; Schauble, D.; Schaefer, M.; Schumann, U., Measurements of HONO, NO, NO(y) and SO(2) in aircraft exhaust plumes at cruise. *Geophysical Research Letters* **2011,** *38*.

39. Yelvington, P. E.; Herndon, S. C.; Wormhoudt, J. C.; Jayne, J. T.; Miake-Lye, R. C.; Knighton, W. B.; Wey, C., Chemical speciation of hydrocarbon emissions from a commercial aircraft engine. *Journal of Propulsion and Power* **2007,** *23*, (5), 912-918.

40. Wood, E. C.; Herndon, S. C.; Timko, M. T.; Yu, Z.; Miake-Lye, R. C.; Lee, B. H.; Santoni, G. W.; Wofsy, S. C.; Munger, J. W.; Knighton, W. B.; Anderson, B., Aircraft emissions, plume chemistry, and alternative fuels: results from the APEX and AAFEX campaigns. In *AGU*, 2009.

41. Fenter, F. F.; Rossi, M. J., Heterogeneous kinetics of HONO on H2SO4 solutions and on ice: Activation of HCl. *Journal of Physical Chemistry* **1996,** *100*, (32), 13765-13775.

42. Longfellow, C. A.; Imamura, T.; Ravishankara, A. R.; Hanson, D. R., HONO solubility and heterogeneous reactivity on sulfuric acid surfaces. *Journal of Physical Chemistry A* **1998,** *102*, (19), 3323-3332.

43. Zhang, R. Y.; Leu, M. T.; Keyser, L. F., Heterogeneous chemistry of HONO on liquid sulfuric acid: A new mechanism of chlorine activation on stratospheric sulfate aerosols. *Journal of Physical Chemistry* **1996,** *100*, (1), 339-345.

Chapter 4:

Reactive chemistry in aircraft exhaust: Implications on air quality[3]

Abstract

Exhaust emitted from jet engines contain high concentrations of combustion by-products, some of which are damaging to human and ecosystem health. As these pollutants mix with the surrounding air, they undergo chemical reactions that eventually break them down to their water-soluble or inert forms. To date, the reactivity of aircraft exhaust has been largely unexplored, and it is not known whether state-of-the-art models account for chemistry at the plume level, which directly relates to air quality downwind of airports. To a large extent, the concentrations of hydroxyl (OH) and hydroperoxyl (HO_2) radicals – collectively called HO_x – present in emitted plumes determine the rate at which components of the exhaust are oxidized. In January of 2009, we quantified emissions of all HO_x precursors including nitrous acid (HONO), formaldehyde (HCHO), acetaldehyde (CH_3CHO) and ozone (O_3) at the Alternative Aviation Fuels Experiment in Palmdale, California. We report that 1) HO_x production rate due to direct emission of these precursors is orders of magnitude faster in the exhaust plume than in "normal" urban air, 2) Concentration of pollutants in plumes do not reach typical ambient levels until it has been diluted by a factor of about 6,000 and that 3) Photolysis of HONO in these plumes is by far the biggest source of HO_x during daytime. Analyses of the reactions involving HO_x demonstrate that propagation of these radicals is favored over termination, which indicate chemical reactivity will continue to be enhanced in these plumes even after it has been diluted down to ambient levels.

[3] Lee, B. H., E. C. Wood, R. C. Miake-Lye, S. C. Herndon, J. W. Munger, S. C. Wofsy (2011), *Transportation Research Record: Journal of the Transportation Research Board*, **No. 2206**, pp. 19-23, doi: 10.3141/2206-03.

4.1. Introduction

There is growing concern regarding aviation emission and its effect on air quality, particularly given the projected increase in global air travel over the coming decades [1-3]. The impact of airports on local air quality and public health is not well understood [4]. Knowledge of emissions of trace gases and particulate matter has improved in the past decade from measurements close behind aircraft engines in operation [5-8]. These measurements of emission indices can be used to generate emission inventories of airports to be utilized as input variables in air quality models. The relationship, however, between emissions and resulting pollutant concentrations is complex and dependent on many variables including transport and mixing, strength and duration of emission source, proximity to the source and chemical processing within the atmosphere. Air quality models that do not account for all of these parameters are unlikely to make accurate forecasts.

Recent studies have shown that the chemistry in the evolving, diluting exhaust plume is drastically enhanced compared to that of the ambient atmosphere [9]. Reaction rates are magnified relative to normal conditions due to concentrated levels of directly emitted reactive species such as volatile organic compounds (VOCs), carbon monoxide (CO), sulfur dioxide (SO_2) and nitrogen oxides (NO_x), all of which are categorized as either a criteria air pollutant or a precursor by the Environmental Protection Agency [10].

The species central to the chemical breakdown of these primarily emitted pollutants in the atmosphere are the hydroxyl (OH) and hydroperoxyl (HO_2) radicals, collectively known – due to the fast inter-conversion between themselves – as HO_x radicals. HO_x species play a key

role in the non-linear, highly coupled dynamics of atmospheric chemistry (see Figure 1). For instance, oxidation of VOCs by HO_x lowers the concentration of the parent VOC, but leads to the formation of potentially more harmful secondary organic aerosols and oxygenated VOCs. Increased chemical activity also leads to the formation of tropospheric ozone (O_3), another criteria air pollutant and greenhouse gas, as well as a major OH precursor.

At the Alternative Aviation Fuels Experiment (AAFEX) conducted in January of 2009, we observed mixing ratios of all of the dominant HO_x precursors emitted in aircraft exhaust, including nitrous acid (HONO), formaldehyde (HCHO), acetaldehyde (CH_3CHO) and O_3. Measurements show that photolysis of these HO_x precursors during daytime results in plumes that are drastically more reactive than air unperturbed by emissions. Analyses suggest that the enhanced reactivity persists even after plumes have diluted down to ambient levels several km downwind. These results call for the need to account for these species that are driving the chemistry, in order to properly assess impact of airports on downwind air quality.

4.2. Methods

Measurements of a whole suite gaseous species and particulate matter were made during AAFEX at various distances (between 3 m and approximately 150 m) behind a DC-8 jet, which was choked on the runway at the NASA Dryden Flight Research Center in Palmdale, California. A total of twelve experiments, each lasting several hours, were conducted over a span of a week at various times of the day to test the wide range of ambient conditions as variables on emissions. Different fuel types (traditional and synthetic) were fed into the engine, which during each experiment was varied from idle to take-off conditions. A detailed report on the experimental setup, mission goals and summary results are presented by *Bulzan et al*. [11].

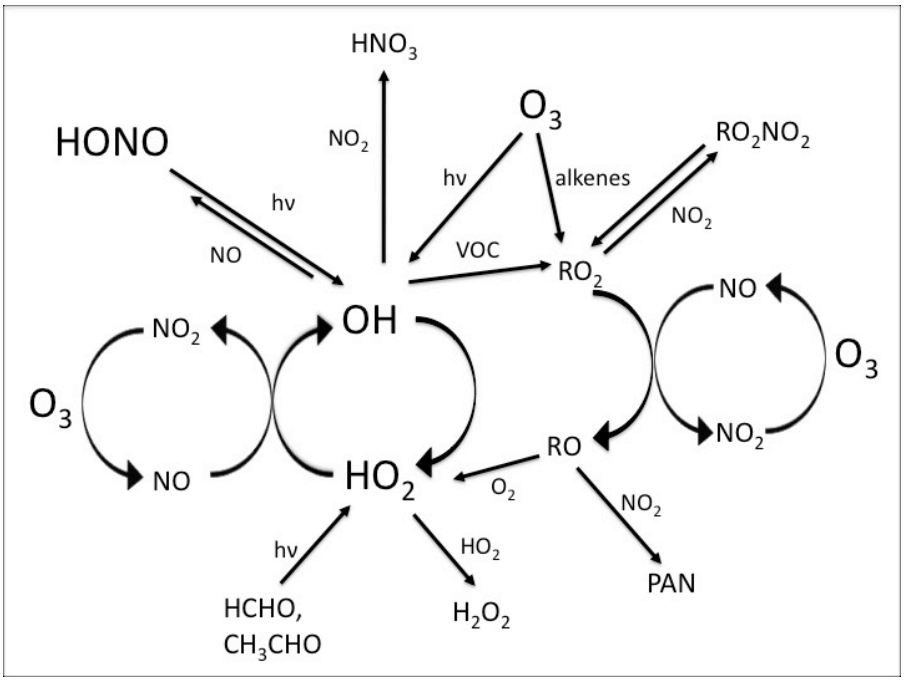

Figure 4.1. A simplified schematic of chemical reactions occurring in the troposphere. OH and HO_2, collectively known as HO_x, are responsible for the breakdown of VOCs and other reactive species. Note the cyclic nature of both HO_x (=OH+HO_2) and NO_x (=NO+NO_2), inter-converting between one another while generating O_3 with each cycle. This cycling is ultimately terminated by the reaction between NO_2 and OH forming nitric acid (HNO_3), which is eventually deposited and lost from the atmosphere.

In this study, we focus on HO_x radical precursors such as formaldehyde and ethene (measured by a dual pulsed-mode infrared laser absorption spectrometer), acetaldehyde and propene (proton-transfer reaction mass spectrometer) and nitrous acid (continuous-wave-mode infrared laser absorption spectrometer). In addition, measurements of carbon dioxide were made using a non-dispersive infrared gas analyzer. The various instrumentation – though they differ in technique – essentially operate by drawing ambient air through an inlet composed of a particle filter or inertial separator (to keep the instruments free of interfering particles) through tubing (to keep instrument out of the path of jet exhaust) and into the instrument where concentrations are quantified. All of the instruments were set up to allow sampling response times of less than one second to be able to resolve the rapid fluctuations in the level of pollutants in the exhaust.

4.3. Results

Figure 2 shows a brief time-series of HONO and CO_2 mixing ratios observed during AAFEX. In figure 2a,b note how the levels of both gases co-vary together in time because of their common emission source and due to atmospheric mixing similarly processing both gases from engine exit to the sampling point. The slope of the correlation plot between HONO and CO_2 (figure 2c) is commonly called the emission *ratio* (ER) and is significant because it quantifies the emission signature of the species of interest (in this case, HONO) relative to CO_2, which is a main by-product of fossil-fuel combustion and readily traceable to the amount of fuel consumed. To adhere to International Civil Aviation Organization standards, we report here the emission *index* (EI) in units of mass (*g*) of *x* per mass (*kg*) of fuel consumed,

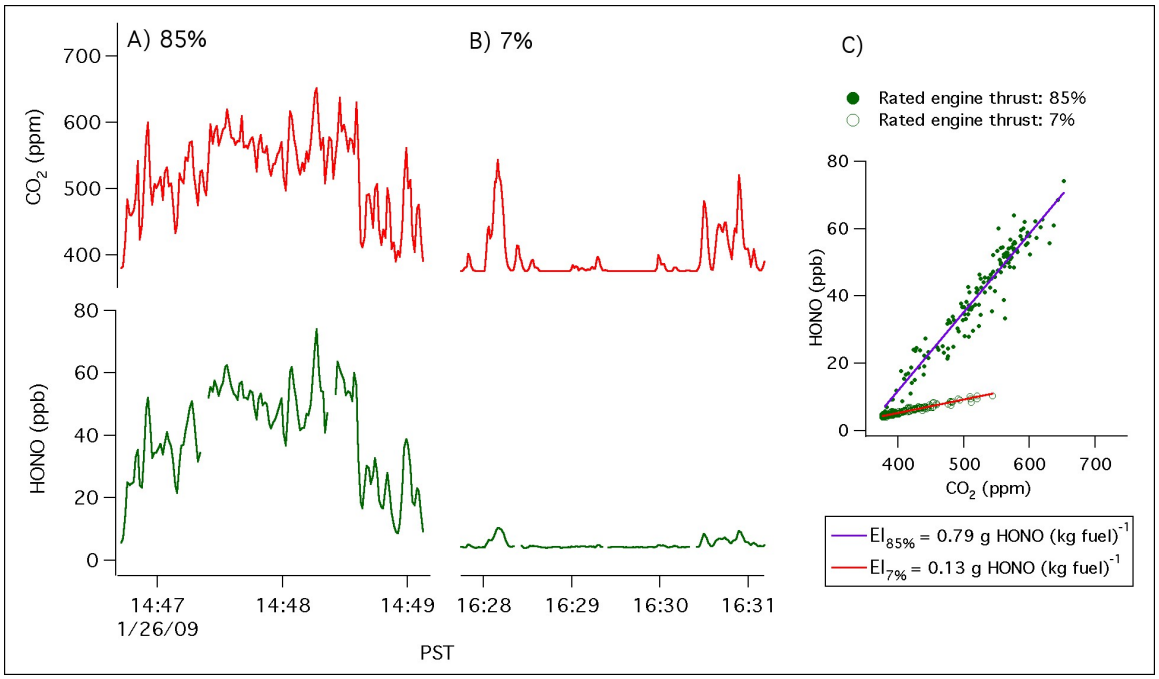

Figure 4.2. Mixing ratios of HONO (parts per billion, ppb) and CO_2 (parts per million, ppm) observed in aircraft exhaust. Twelve experiments were conducted over a period of a week under widely varying ambient conditions and engine settings, which ranged from idle to full thrust. Above is brief excerpt of 1-second time-resolution data. Note how the levels of HONO and CO_2 co-vary together in time at A) high engine power (85% thrust) as well as at B) low engine power (7% thrust). C) HONO plotted against CO_2 clearly shows the dependence of their relationship on engine setting.

$$EI\ \ x = \left(\frac{moles\ \ of\ \ x}{moles\ of\ \ CO_2} \right) \times \left(\frac{molecular\ \ mass\ \ of\ \ x}{molecular\ \ mass\ \ of\ \ CO_2} \right) \times EI\ \ CO_2$$

where EI CO_2 is the emission index of CO_2, which for jet fuel is 3,160 g of CO_2 emitted per kg of fuel consumed.

Figure 3 shows the EI of HONO plotted as a function of rated engine thrust. Each data point at a given engine setting in figure 3 is the AAFEX campaign averaged value, which is composed of hundreds of emission indices calculated from individual plumes lasting anywhere from a few to 30 seconds. Approximately 0.1 g of HONO is emitted on average for every kg of fuel consumed at engine idle (~7% rated engine thrust), and increases nearly seven-fold at 60% rated engine thrust, beyond which EI for HONO remains fairly constant. HONO is formed within the engine primarily by the gas-phase reaction between nitric oxide (NO) and OH. As the engine power is increased from idle thrust, the concentrations of both NO and OH in the engine increase, resulting in greater HONO EI values. HONO EI is *not* significantly affected by ambient temperature (which ranged from slightly below 0°C to 23°C), relative humidity (20 to 70%), presence of sunlight, wind speed or direction, or fuel type (traditional jet fuel, coal-derived or natural-gas derived synthetic fuels). The dominant variable influencing HONO EI is the engine power setting (Figure 3).

4.4. Discussion

In typical unperturbed ambient atmosphere, HO_x is predominantly generated by sun-light induced photolysis of O_3 and HCHO with some contributions from the photolysis of HONO and

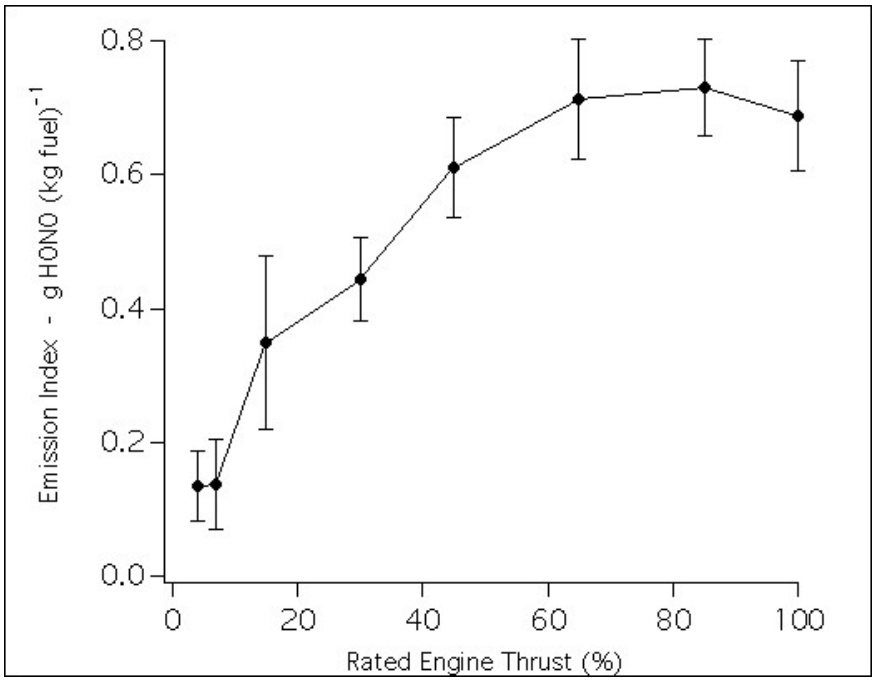

Figure 4.3. HONO emission index from a single CFM-56 jet engine plotted as a function of rated engine thrust. Each EI value represents the campaign average of all observed individual plumes, each lasting from a few seconds to approximately 30 seconds. The error bars represent the 1-σ of the average.

the ozonolysis reaction between O_3 and various alkenes (mainly ethene and propene), as illustrated by the reactions listed below.

(R1a) $O_3 + h\nu \rightarrow O_2 + O(^1D)$

(R1b) $O(^1D) + H_2O \rightarrow 2OH$

(R2a) $HCHO + h\nu \rightarrow HCO + H$

(R2b) $H + O_2 + M \rightarrow HO_2 + M$

(R2c) $HCO + O_2 + M \rightarrow CO + HO_2 + M$

(R3a) $CH_3CHO + h\nu \rightarrow CH_3CO + H$

(R3b) $H + O_2 + M \rightarrow HO_2 + M$

(R4) $HONO + h\nu \rightarrow NO + OH$

(R5a) $O_3 + \text{alkene} \rightarrow \text{products} + OH + RO_2 + HO_2$

where $h\nu$ represents the energy from sunlight absorbed by the reactants.

The rates at which these reactions proceed are dependent on the reactant concentrations and the rate constants, which for the photolysis reactions (R1-R4) are a function of the intensity and wavelength of the incident radiation. Consequently, since each of the five chemical reactions (R1-R5) listed above yield at least one HO_x radical (either OH or HO_2), the total HO_x production rate is given by the sum of the reaction rates R1 through R5.

(R6) $P(HO_x) = R1 + R2 + R3 + R4 + R5$

$= 2\times j_{1b}\times[O(^1D)][H_2O] + 2\times j_2\times[HCHO] + 2\times j_3\times[CH_3CHO] + j_4\times[HONO] +$

$k_4\times[O_3]\times[\text{alkene}](HO_x \text{ yield})$

where the "j values" are photolysis rate constants and "k values" are the reaction rate constants. Table 1 lists the photolysis rates for O_3, HCHO, CH_3CHO and HONO under typical cloudless sky conditions at 30° solar zenith angle obtained using NCAR's (National Center for Atmospheric Research) TUV model [12]. The concentration of the reactant species at engine exit is calculated from the emission ratios with respect to CO_2 observed at AAFEX. Since the concentration of CO_2 at the engine exit is well known (2.1% at engine idle and 4% at high power), the corresponding concentration of the species of interest at engine exit is simply the product of the emission ratio and the CO_2 concentration at engine exit.

Figure 4a shows the production rate of HO_x in exhaust plumes due to the photolysis of emitted precursors relative to what is typically observed in the ambient atmosphere, plotted as a function of plume dilution. A dilution factor of one represents conditions at engine exit before any mixing or dilution has taken place. Emission rate of precursors used in the calculation here are representative of those observed at engine idle and photolysis rates are from conditions listed in table 1. From this figure, the HO_x production rate is several orders of magnitude faster inside the exhaust plume at the engine exit and only reaches those observed in normal air after being diluted by a factor of about 6,000. A breakdown of the relative strengths of the precursors show that HONO is the biggest contributor to HO_x production due in part to its fast photolysis rate

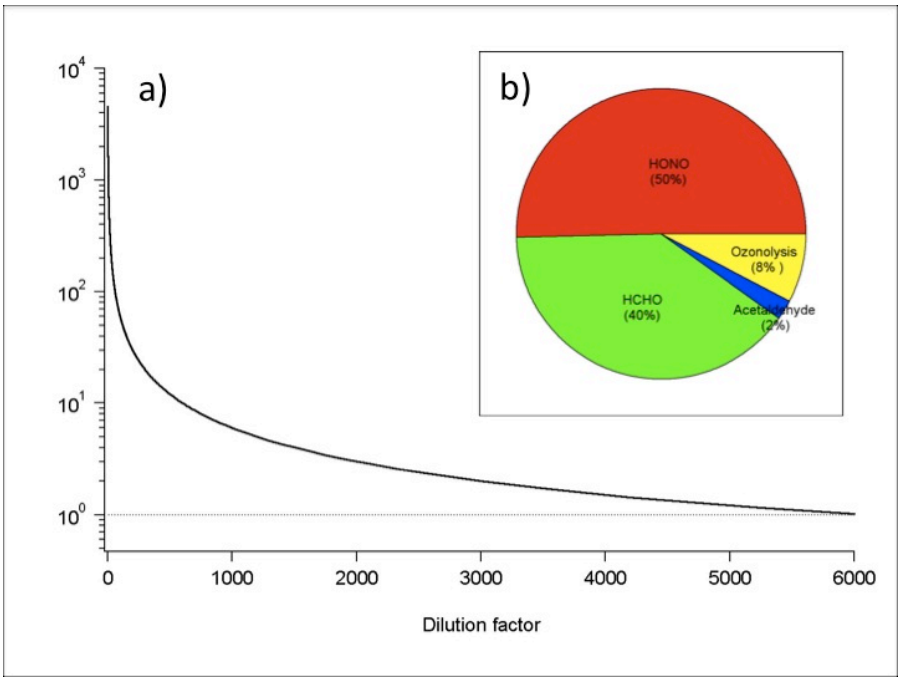

Figure 4.4. a) Ratio of HO_x radical production rate in jet exhaust relative to those under "typical" urban conditions (~0.5 parts per trillion per second), plotted versus plume dilution factor. HO_x is produced from the photolysis of precursors including HONO, HCHO, CH_3CHO and the ozonolysis reactions between O_3 and alkenes. b) Relative strengths of HO_x sources in jet exhaust.

Table 4.1. Shows the photolysis rates of HO_x precursors emitted from jet exhaust. Rates are calculated for typical cloud-less winter mid-day conditions at 30° solar zenith angle.

Reaction	Precursor	Photolysis rate (sec^{-1})
R1a	**O_3**	**3.4×10^{-5}**
R2a	**HCHO**	**3.2×10^{-5}**
R3a	**CH_3CHO**	**5.4×10^{-6}**
R4	**HONO**	**2.1×10^{-3}**

(table 1), followed by HCHO, then the ozonolysis reactions of ethene and propene, and lastly CH_3CHO (figure 4b).

Relating dilution factor to actual distance from emission source is problematic, since the rate at which dilution occurs in the ambient atmosphere is governed by numerous factors including wind speed, wind shear and geographic conditions. Figure 5 shows dilution factors estimated from measured CO_2 levels (relatively inert at these time-scales) observed in diluting, evolving plumes sampled at various distances from airports in numerous field campaigns including AAFEX. Observations from these campaigns with varying ambient conditions and geographic layouts indicate that dilution due to mixing occurs at a relatively predictable rate at these distances and that concentration of an emitted species reaches background levels of normal air between approximately 1 and 4 km (0.6 and 2.4 miles) downwind of airports.

It is, however, important to stress here that based on previous measured emission indices of reactive gases and the rates at which they are oxidized by HO_x radicals, we calculate that > 95% of the OH radical produced in these plumes react with VOCs and CO because they are emitted in large quantities from idling engines due to inefficient fuel combustion. These reactions tend to favor cycling between OH and HO_2 while generating noxious gases such as O_3 and alkyl peroxyl radicals. This branching of chemistry (figure 1), thus represents propagation of HO_x. The reaction between OH and NO_2 forming nitric acid (HNO_3) – which is readily lost from the atmosphere through deposition thus terminating the cycling between OH and HO_2 – occurs less frequently. In short, the regeneration of HO_x species due to the rapid cycling between OH and HO_2 is favored in these plumes over termination. The decrease in HO_x production rate diagrammed in figure 4 only takes into account dilution and not the propagation due to cycling.

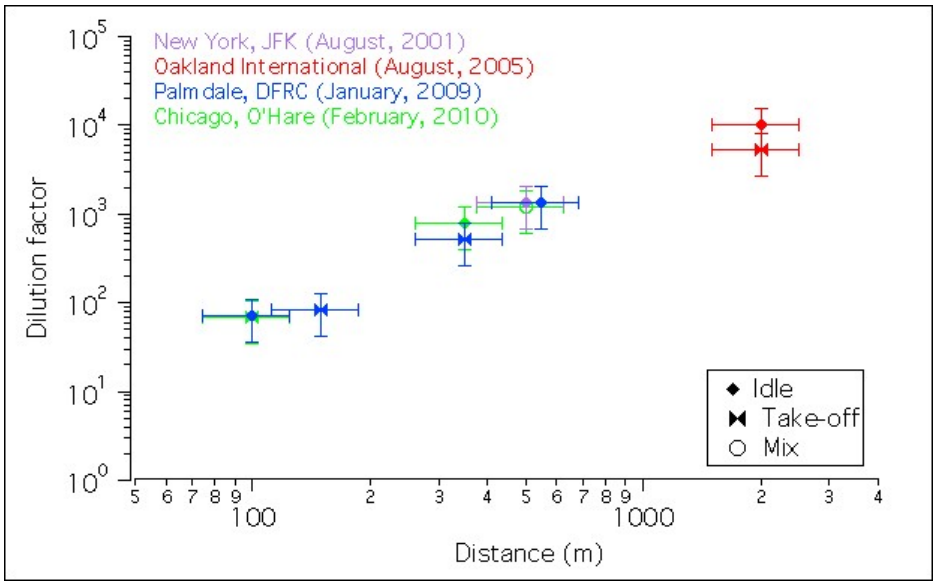

Figure 4.5. Plume dilution factor calculated from CO_2 measurements made at varying distances from the emission source, plotted versus distance.

Consequently, enhanced reactivity (faster HO_x production than in normal air) is sure to persist farther downwind than the 1 to 4 km calculated above.

Lastly, it should be noted that HO_x production in these plumes occurs only during daytime through sun-light induced photolysis of emitted precursors. During nighttime, emissions from airports would lead to the buildup of these HO_x precursors as well as the other emitted pollutants such as VOCs, NO_x and SO_2 in the nighttime air. This nighttime build-up is enhanced because of the so-called nocturnal boundary layer as it traps emissions at the surface due to an inversion in the vertical temperature profile. Therefore, nighttime emissions can serve as a significant pulse of reactivity in the morning immediately following sunrise when photolysis commences.

4.5. Conclusion

We report measurements of HO_x precursors in aircraft exhaust made during the AAFEX field campaign in January of 2009 at the NASA Dryden Flight Research Center. Analyses show photolysis of nitrous acid (50%) is the dominant source of HO_x in exhaust plumes, followed by photolysis of formaldehyde (40%), the ozonolysis reactions between ozone and light alkenes (8%), then photolysis of acetaldehyde (2%). Due to the enhanced levels of precursors, the reactivity of emitted plumes reach HO_x production rates usually observed in ambient air after it is diluted by three to four orders of magnitude, or approximately between 1 and 4 km downwind of emission sources. However, due to the cyclic nature – reaction followed by regeneration – of the HO_x radicals, enhanced chemistry likely persists much farther downwind.

Analyses presented here provide strong evidence for the need to account for HO_x precursors in engine exhaust due to it role in driving chemistry. This is required in order to realistically translate airport emission inventories to enhancements in the pollutant levels downwind, and ultimately to assess the effects on the health of nearby communities. Species such as tropospheric ozone and secondary organic aerosols are not directly emitted from engines but are harmful by-products of the transformations driven by chemistry. The measurements made during AAFEX will help bridge that gap in understanding between emissions and impact, and allow future modeling efforts to improve assessments.

All of the HO_x precursors discussed above are in some form already monitored by the International Civil Aviation Organization, which sets certification guidelines for aviation-related emissions of CO, NO_x and total VOCs. HONO is indirectly included in the NO_x inventory, as are HCHO, CH_3CHO, ethene and propene in the total VOC inventory. Therefore, explicit regulation of these gases is likely not necessary, however, determining the scaling of these particular species to their respective inventories would greatly aid future modeling programs.

Acknowledgments

The authors gratefully acknowledge the Transportation Research Board for the Airport Cooperative Research Program Award.

Rerferences

1. Lee, D. S.; Fahey, D. W.; Forster, P. M.; Newton, P. J.; Wit, R. C. N.; Lim, L. L.; Owen, B.; Sausen, R., Aviation and global climate change in the 21st century. *Atmospheric Environment* **2009,** *43*, (22-23), 3520-3537.

2. Mohn, T. At German Airports, Bees Help Monitor Air Quality. http://www.nytimes.com/2010/06/29/business/29airports.html?ref=air_pollution (September 4, 2010),

3. Penner, J. E., *Aviation and the global atmosphere*. Cambridge University Press: Cambridge, 1999; p 373 p.

4. Klemm, R.; Wyzga, R.; Thomas, E., Daily Mortality and Air Pollution in Atlanta: August 1998-December 2006. *Epidemiology* **2009,** *20*, (6), S223-S223.

5. Anderson, B. E.; Chen, G.; Blake, D. R., Hydrocarbon emissions from a modern commercial airliner. *Atmospheric Environment* **2006,** *40*, (19), 3601-3612.

6. Miake-Lye, R. C.; Anderson, B. E.; Cofer, W. R.; Wallio, H. A.; Nowicki, G. D.; Ballenthin, J. O.; Hunton, D. E.; Knighton, W. B.; Miller, T. M.; Seeley, J. V.; Viggiano, A. A., SOx oxidation and volatile aerosol in aircraft exhaust plumes depend on fuel sulfur content. *Geophysical Research Letters* **1998,** *25*, (10), 1677-1680.

7. Spicer, C. W.; Holdren, M. W.; Smith, D. L.; Hughes, D. P.; Smith, M. D., Chemical-Composition of Exhaust from Aircraft Turbine-Engines. *Journal of Engineering for Gas Turbines and Power-Transactions of the Asme* **1992,** *114*, (1), 111-117.

8. Yelvington, P. E.; Herndon, S. C.; Wormhoudt, J. C.; Jayne, J. T.; Miake-Lye, R. C.; Knighton, W. B.; Wey, C., Chemical speciation of hydrocarbon emissions from a commercial aircraft engine. *Journal of Propulsion and Power* **2007,** *23*, (5), 912-918.

9. Wood, E. C.; Herndon, S. C.; Timko, M. T.; Yelvington, P. E.; Miake-Lye, R. C., Speciation and chemical evolution of nitrogen oxides in aircraft exhaust near airports. *Environmental Science & Technology* **2008,** *42*, (6), 1884-1891.

10. United States. National Air Pollution Control Administration., *Air quality criteria for photochemical oxidants*. [For sale by the Supt. of Docs.: Washington;, 1970; p 1 v. (various pagings).

11. Bulzan, D.; Anderson, B.; Wey, C.; Howard, R.; Winstead, E. H.; Beyersdorf, A.; Corporan, E.; DeWitt, M. J.; Klingshirn, C. D.; Herndon, S. C.; Miake-Lye, R.; Wood, E. C.; Tacina, K.; Liscinsky, D. S.; Hagen, D.; Lobo, P.; Whitefield, P. In *Gaseous and Particulate Emissions Results of the NASA Alternative Aviation Fuel Experiment (AAFEX)*, ASME Turbo Expo 2010: Power for Land, Sea, and Air (GT2010), Glasgow, UK, June 14-18, 2010, 2010; ASME: Glasgow, UK, 2010; pp 1195-1207.

12. Hutzinger, O., The Handbook of environmental chemistry. In Springer-Verlag: Berlin ; New York, 1980; p v.

Chapter 5:

Effective line strengths of *trans*-nitrous acid near 1275 cm^{-1} and *cis*-nitrous acid at 1660 cm^{-1} using cw-QC TILDAS[4]

Abstract

We determined the effective line strengths of the *trans* conformer of nitrous acid (HONO) near 1275 cm^{-1} (R-branch of ν_3 mode, N-O-H bend) and of the *cis* conformer at 1660 cm^{-1} (R-branch of ν_2 mode, N=O stretch), both at a spectral resolution of 0.001 cm^{-1} by tunable infrared laser differential absorption spectroscopy (TILDAS) utilizing continuous wave quantum cascade lasers. Absorbance of one conformer was measured while simultaneously quantifying the mixing ratio of total HONO by catalytic conversion to nitric oxide (NO) followed by calibrated absorption spectroscopy. Line strengths obtained here are consistent with band strengths reported by *Kagann and Maki* [1] for the *trans* conformer but are lower by a factor of approximately 2.4 for the *cis* conformer.

5.1. Introduction

Nitrous acid (HONO) is a short-lived atmospheric reservoir of nitric oxide (NO) and the hydroxyl radical (OH). Photolysis of HONO – subsequent to formation by a pathway not involving OH or the hydroperoxyl radical (HO_2) – represents a net source of HO_x (=OH+HO_2), collectively, one of the main drivers of atmospheric oxidation. Nighttime buildup beneath the boundary layer due to combustion emissions and heterogeneous reaction of nitrogen dioxide

[4] Lee, B. H., Wood, E. C., Wormhoudt, J., Shorter, J. H., Herndon, S. C., Zahniser, M. S., Munger, J. W. (2012), *Journal of Quantitative Spectroscopy & Radiative Transfer*, submitted.

(NO_2) provides the dominant source of reactivity in the early morning [2, 3]. Recent reports of HONO levels exceeding those expected at photostationary state suggest a secondary daytime source that may constitute a significant portion of the daily HO_x budget in urban [4-6], rural [7-10] and remote [11-13] atmospheres. In indoor environments, combustion from cooking directly releases HONO and NO_x (=NO+NO_2), which react to generate additional HONO. At enhanced levels (from few part-per-billion to several hundred ppb), HONO by itself is a minor lung and eye irritant [14, 15]. Reactions with amines present in the gas phase [16] and as residue on surfaces previously exposed to cigarette smoke yield carcinogenic nitrosamines, the effect of which has been commonly called "third-hand" smoke [17]. However, the chemical mechanism, rate and nature of the substrate on which production takes place remain uncertain.

Many HONO measurement techniques rely on wet-chemical extraction, by which gaseous HONO is captured in liquid form, derivatized then quantified via photometry or chromatography [18-21]. Though offering near part-per-trillion (ppt) sensitivity, they are potentially prone to chemical interferences and have not always shown good agreement with optical techniques [22, 23]. Absorption spectroscopy – applied previously in open-path [2-4, 24] and enclosed cell [25-29] systems to measure ambient air and combustion exhaust – offers a more direct method with greater specificity. However, the fundamental rotational-vibrational transitions of HONO in the mid-infrared spectral region are not accurately represented in any comprehensive linelist [30, 31].

We report *effective* line strengths – the absorbance of light by one conformer per unit column density of total (*cis* + *trans*) HONO – determined for the *cis* conformer at 1660 cm^{-1} and the *trans* near 1275 cm^{-1} at 303 K. The *absolute* line strengths – absorbance of light per unit column density of that particular conformer – could be calculated given the *cis-trans* equilibrium

constant, but the accuracy would be limited by large uncertainty in equilibrium constant [32]. The effective strength, along with line position and air-broadened halfwidth at half maximum, γ_{air} (cm^{-1} atm^{-1}), provide the necessary parameters to quantify the concentration of total HONO by TILDAS. As thermal equilibrium between the two conformers via isomerization occurs nearly instantaneously (~10^{-12} seconds), maintaining the sample at a constant temperature for a few seconds ensures accurate total HONO quantification that is independent of thermal changes in the ambient atmosphere. We compare these results to previous effective band strength studies and discuss optimal spectral regions in which to measure HONO.

5.2. Experimental Methods

Figure 1 is a schematic of the experimental setup. Concentrated gaseous HONO was introduced into the sample cell of a dual-laser TILDAS system, in which the absorbance of *cis*-HONO (1659.25-1660.10 cm^{-1}; Alpes Lasers) and NO_2 (1604.56 cm^{-1}; Alpes Lasers) were simultaneously measured over an absorption path length of 210 m at reduced pressures. Total HONO at the same time was quantified via complete reduction of the sub-sampled mixture by molybdenum catalysis (TEI) to NO, which was continuously measured by a calibrated single-laser TILDAS instrument. Other reducible nitrogen oxide species that may have been generated along with HONO were accounted for by monitoring the NO mixing ratio prior to conversion by O_3-chemiluminescence (ThermoElectron 42i), and NO_2 by absorption spectroscopy. Additions were conducted over a range of cell pressures (6 to 70 torr) to determine γ_{air}. The dual-laser instrument was then reconfigured to concurrently measure the absorbance of both *cis* and *trans* conformers. HONO was again introduced at various cell pressures. The effective line strength and γ_{air} of the *trans* conformer (1273.38-1273.47 cm^{-1}; 1273.57-1273.62 cm^{-1}; 1274.26-1274.36

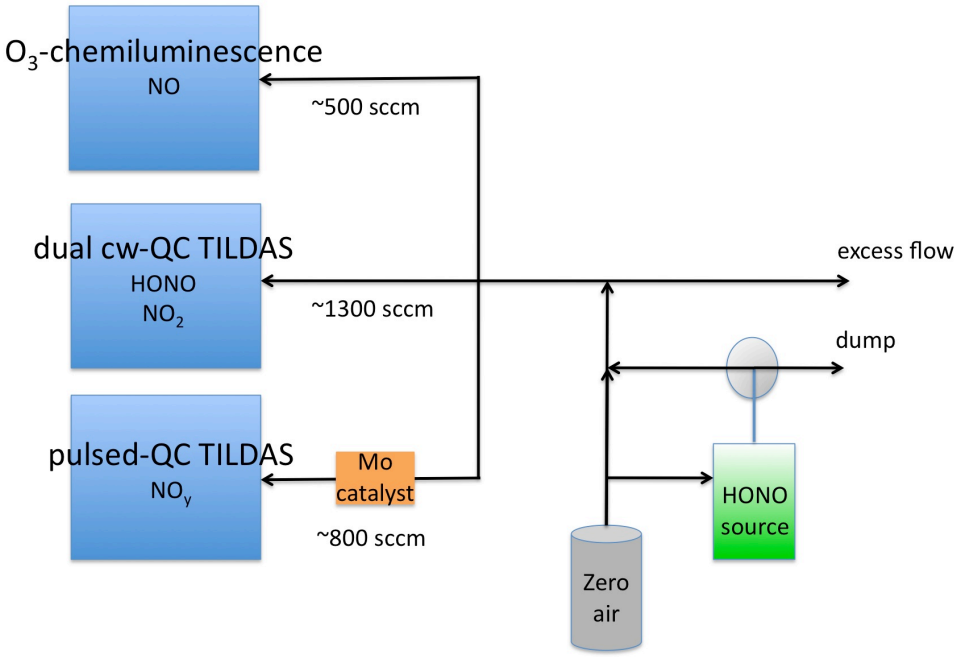

Figure 5.1. Schematic of the instrumental setup used to determine absorption parameters for the *cis* conformer.

cm^{-1}; 1275.74-1275.84 cm^{-1}; Hamamatsu Photonics) was determined from the total HONO value obtained using the previously determined *cis* conformer absorption parameters.

Laser temperature control, data acquisition and spectral fitting for the laser-based systems were controlled by the software TDLWintel (Aerodyne Research, Inc.). Thermo-electrically cooled QC lasers were spectrally tuned by providing them with a programmable current ramp from a high-compliance source (ILX Lightwave) to induce a milli Kelvin-scale temperature change to tune the output light over a range of approximately 0.2 cm^{-1}. The QC lasers for both HONO conformers and NO_2 were scanned at a rate of 150 Hz (a factor of approximately 10 slower than typical operational conditions) to ensure line shape symmetry. The instrumental line widths for all three lasers were less than the 0.001 cm^{-1} spectral resolution. This was determined by scanning nearby lines of water vapor, for which absorption parameters are well known [31], at cell pressures below 2 torr to minimize collisional broadening. Details regarding the optical layout, signal detection and sensitivity of the spectrometers are provided elsewhere [33, 34].

Gas additions typically lasted between 30 to 120 seconds, over which the mixing ratios (and spectra) were averaged in time to reduce the variance of the final values used in the line strength calculations, described below. Flow rates were maintained to ensure sufficient mixing and to minimize residence times inside tubing and sample cells. Perfluoroalkoxy tubing was utilized and the sample cells of the TILDAS systems were treated with a siloxyl coating to reduce surface chemistry. Figure 2a shows a brief time series of mixing ratios when NO_2 generated from a permeation device (Valco Instruments Co. Inc.) was introduced. The agreement between NO_2 quantified directly with the QC laser using HITRAN absorption parameters [31] and NO resulting from catalytic conversion (figure 2a), exhibits the purity of the laser mode. We also observed agreement in water vapor measurements between the two QC lasers at 1605.675 cm^{-1}

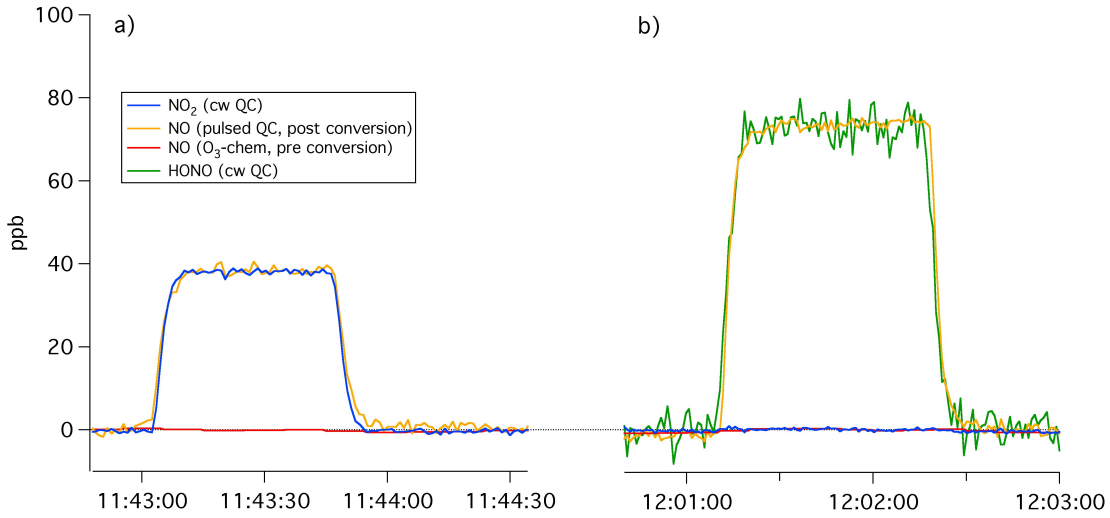

Figure 5.2. Time series (1-hertz) of HONO, NO_2 and NO (measured by two different instruments) mixing ratios (ppb) during two gas addition experiments. Addition of a) NO_2 from a permeation device and from generated b) HONO.

and 1660.467 cm^{-1} (not pictured), establishing the laser mode purity of the *cis*-HONO laser. Moreover, additions of varying levels of NO_2 from a tank source and its absence downstream of the catalytic converter demonstrated complete conversion efficiency. We assume unity efficiency in reduction for HONO as well, as previously reported [35].

The single-channel TILDAS system used to quantify the post-conversion NO mixing ratio was calibrated using a NO tank source (Scott Specialty, 34.6 ppm ± 1%), which tested to within 1% of another NO tank (Airgas "Primary Standard", 250.6 ppm) owned by NASA-Glenn (Changlie Wey). A five-point calibration procedure for NO was conducted for the TILDAS and O_3-chemiluminescence NO instruments before and after the line strength quantification experiment. The sensitivity, hence calibration, of the O_3-chemiluminescence instrument is affected by humidity and was taken into account by conducting calibrations at the same water vapor mixing ratio observed during the addition experiments. Output flow rates from a dynamic gas calibrator (ThermoElectron, model 146i) used during NO calibrations were compared to two calibrated (Gilibrator and Bios Dry Cal) flow meters and showed agreement to within 3%. The transducer (MKS, 0 to 1000 torr) measuring the pressure inside the sample cell was calibrated at 0 torr and at ambient pressure using a Hg-manometer.

Figure 2b shows a brief time series of mixing ratios during an addition of gaseous HONO, generated by flowing UltraPure air (Middlesex gases) first through a gas-washing bottle filled with dilute hydrochloric acid (Sigma Aldrich, 30% wt.) then through a 50-mL round-bottom (1 inch diameter) Pyrex chamber loaded with approximately 5 g sodium nitrite granules (Sigma-Aldrich, 99.999%) where HONO was produced via reaction R_1 [36]. Side products NO and NO_2 likely produced by reaction R_2 accounted for less than 3% by mixing ratio of total HONO and were explicitly taken into account. Nitric acid (HNO_3) – also reducible to NO by molybdenum

catalysis – was not directly measured during the experiments. Addition of gaseous HNO_3 from a permeation device and measured as NO following catalytic conversion exhibited a much slower response time through the system due to surface interaction (not pictured) than those exhibited by NO and NO_2 (figure 2), gases unlikely to strongly interact with surfaces. We assert negligible amounts of HNO_3 via reaction R_3 were generated alongside HONO, which exhibited response times through the system similar to those of NO and NO_2 (figure 2b). We assume nitrosyl chloride (ClNO) was also a negligible contributor due to its slow formation rate [37] and the fact that HONO output levels were positively dependent on the concentration of the HCl solution, indicating HCl was the limiting reagent thus unavailable for reaction R_4 downstream of the $NaNO_2$ chamber. Potential interferences from other reducible nitrogen oxide species such as NO_3, N_2O_4 and N_2O_5 were assumed to be nonexistent due to the short residence times in the system and the absence of an ozone precursor.

R_1) $HCl(g) + NaNO_2(s) \rightarrow HONO(g) + H_2O$

R_2) $HONO(g) + HONO(ads) \rightarrow NO(g) + NO_2(g) + H_2O$

R_3) $HONO(g) + NO_2(g) \rightarrow NO(g) + HNO_3(g)$

R_4) $HCl(g) + HONO(g) \rightarrow ClNO(g) + H_2O$

Top panels of figures 3 and 4 show the observed absorbance during HONO addition experiments for the *cis* and *trans* conformers, respectively. Effective line strengths were calculated by taking into account the total HONO concentration, laser light path length, instrumental line width and sample cell pressure and temperature, using an algorithm called SELECTLINES [38] (Igor Pro, version 4.2, WaveMetrics, Inc.) developed by Aerodyne

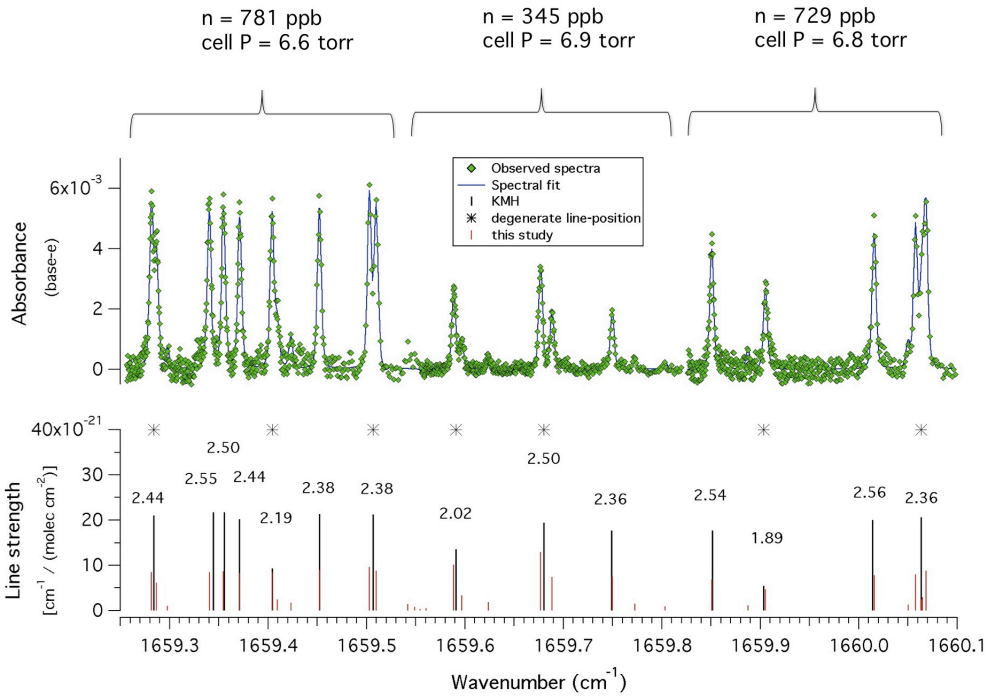

Figure 5.3. Absorbance (base e) spectra of *cis*-HONO (top panel) and effective line strengths (bottom panel) from KMH (black) and this study (red), all plotted as a function of wavenumber (cm^{-1}). Listed numbers represent the ratio of KMH strengths to those from this study. Brackets above the figure summarize each experimental condition. Asterisks point to degenerate entries in KMH due to limited spectral resolution.

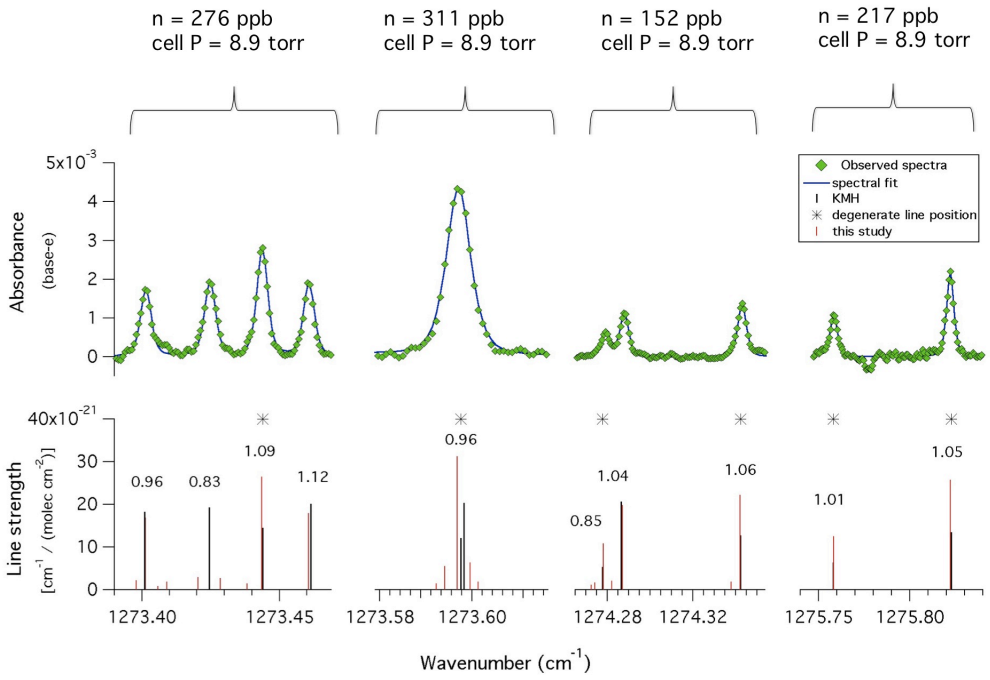

Figure 5.4. Same as figure 3, for *trans*-HONO.

Research, Inc. The program first determines the line position given an initial guess then calculates the strength of each line by fitting a Voigt line profile to the observed absorbance spectrum. Absolute HONO line positions were determined relative to those of nearby water vapor and/or nitrous oxide along with laser tuning rates determined by recorded spectra of a germanium etalon, all except for experiments conducted when scanning between 1659.25 and 1659.55 cm^{-1} and between 1659.85 and 1660.10 cm^{-1}. In these instances, HONO line positions were based on those obtained from a broad-band FTIR spectrum with resolution better than 0.005 cm^{-1} ranging from 700 to 4,000 cm^{-1}, provided by *M. Herman* (personal communication). The same spectrum provided relative line strengths, which were scaled to absolute line strengths of the *trans* ν_3 mode from the ATMOS database [30], whose strengths are based upon band strengths reported by *Kagann and Maki* [1]. The resulting line strengths are hereafter referred to as KMH and serve as the basis of comparison to other studies discussed below.

The air-broadened half-width at half-maximum (γ_{air}) was obtained by iteratively varying γ_{air} by 0.0010 cm^{-1} atm^{-1} to optimize the spectral fits to each observed spectrum at eight different pressures from 6.6 to 72.1 torr. A common value of 0.0980 ± 0.0050 cm^{-1} atm^{-1} for γ_{air} was obtained for both conformers for all line scanned. All experiments were conducted at 303 K. Uncertainty in the reported line strengths is less than 6%, estimated by aggregating the errors associated with the accuracy of the NO tank (1%), NO calibration (0.5% in slope), mass flow rate (1% for small head, 2% for large head) and pressure transducer (1%).

5.3. Results and Analysis

The top panels of figures 3 and 4 show the observed absorbance spectra and their corresponding least-square non-linear fits using the calculated line strength, line position and γ_{air}

values. The bottom panels compare our line strengths to those of KMH, described above. Tables 1 and 2 list the line position and strengths obtained from this study for the *cis* and *trans* conformers, respectively.

Whereas the cumulative strengths for each of the 10 discernible peaks for the *trans* conformer near 1275 cm^{-1} (figure 4, top panel) are on average consistent with those of KMH, the 14 peaks for the *cis* conformer at 1660 cm^{-1} (figure 3, top panel) are lower than those of KMH by a factor of approximately 2.4. This discrepancy for the *cis* ν_2 band is likely a result of the difficulty – caused by the presence of lines of interfering species – associated with accurately integrating the broad-band spectrum of *Kagann and Maki* [1]. Figure 5 compares two sets of absorbance spectra of the ν_2 bands of *cis* and *trans*-HONO centered around 1640 and 1699 cm^{-1}, respectively. The solid black line represents FTIR observations made by *Sharpe et al.* [39], who also normalized their broad-band HONO spectrum by the ν_3 band strength value of *Kagann and Maki* [1]. The dotted grey line is a simulated spectrum generated using the KMH line strengths and positions under the same experimental conditions of *Sharpe et al.* [39], hereafter referred to as S04. Note the KMH spectrum shows comparable absorbance depths for the ν_2 bands of the *cis* and *trans* conformers, as does the spectrum observed by *Kagann and Maki* [1] (top panel of their figure 3). S04, on the other hand, exhibits absorbance by the *cis* conformer that is about half that of KMH, consistent with observation of this study.

One critical difference between these experiments is the method of generating gaseous HONO. The spectra presented here and by S04 were obtained from a near-pure source of gaseous HONO, generated according to the protocol of *Febo et al.* [36]. *Kagann and Maki* [1], on the other hand, obtained HONO as a minor byproduct from the heterogeneous reactions between water vapor and nitrogen oxides sealed in a static vessel. Consequently, spectral

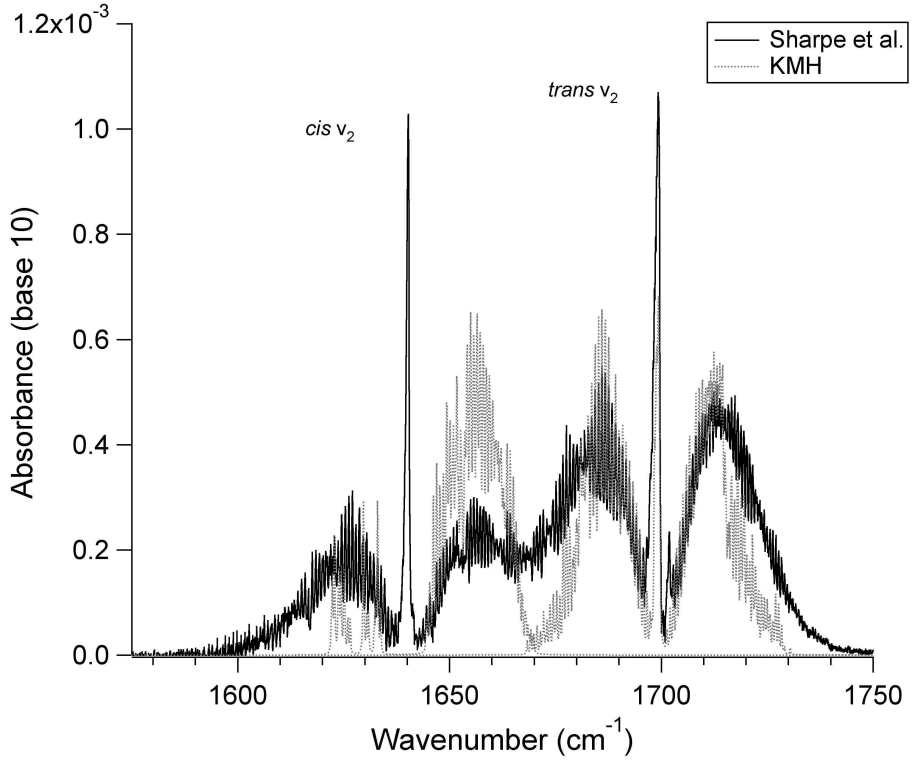

Figure 5.5. Absorbance spectra (base 10) obtained by S04 (black) and KMH (grey) of the ν_2 bands of *cis* and *trans*-HONO centered around 1640 and 1699 cm^{-1}, respectively. While there is good agreement between the two spectra for the *trans* conformer, the S04 spectrum is lower than that of KMH by about a factor of two for the *cis* conformer.

Table 5.1. Line positions and effective line strengths for *cis*-HONO at 303 K.

Line position cm^{-1}	Line strength cm^{-1} / (molec-cm^{-2}) $\times 10^{-22}$
1659.281714	84.99
1659.286911	61.68
1659.298047	10.49
1659.340462	85.30
1659.354836	86.99
1659.371374	82.90
1659.404336	84.47
1659.409714	24.11
1659.423318	16.95
1659.452315	89.83
1659.503076	95.71
1659.509912	88.10
1659.542224	14.09
1659.549186	8.30
1659.554688	3.54
1659.560453	4.88
1659.588721	101.50
1659.596820	32.83
1659.623827	18.63
1659.676974	129.20
1659.688638	74.19
1659.749633	74.88
1659.772514	15.57
1659.803308	9.34
1659.850733	69.18
1659.887624	11.23
1659.905308	46.62
1660.015667	77.78
1660.050167	13.57
1660.057681	79.63
1660.063576	24.24
1660.064774	28.94
1660.068246	87.64
1660.068246	87.64

Table 5.2. Line position and effective line strengths for *trans*-HONO at 303 K.

Line position cm^{-1}	Line strength cm^{-1} / (molec-cm^{-2}) $\times 10^{-22}$
1273.397922	22.30
1273.401383	168.50
1273.405927	8.29
1273.409133	19.27
1273.420385	29.12
1273.424695	17.63
1273.428455	17.63
1273.438182	15.00
1273.443661	264.80
1273.460643	179.20
1273.593035	15.04
1273.594676	55.26
1273.597142	312.80
1273.599613	63.20
1273.601263	18.53
1274.272566	11.12
1274.274129	16.36
1274.278059	108.10
1274.281960	20.63
1274.286922	197.80
1274.337689	18.62
1274.341812	222.00
1275.758141	125.20
1275.822070	257.00

subtraction of interfering species was required to obtain the HONO spectrum. We note, for instance, the presence of the much stronger NO_2 absorption structure at the same spectral region as that of the ν_2 band of *cis*-HONO (bottom panel of figure 3 in *Kagann and Maki* [1]). Any biasing errors associated with the NO_2 line shape or concentration would have affected the spectral subtraction, hence, the retrieved HONO band strength. We rule out the difference in *cis*/*trans* ratio resulting from the different way in which gaseous HONO was generated, as the cause of the line/band strength discrepancy for *cis*-HONO. Given an isomerization energy barrier of 9.7 kcal mol^{-1} [40], equilibrium between the two conformers is reached on the order of pico-seconds even in the extreme case that only one conformer is initially generated by the method of *Febo et al.* [36]. Deviation from *cis*/*trans* equilibrium by infrared light absorption-induced isomerization, likewise, did not play a role since the low energy cutoff occurs around 3,200 cm^{-1} [40].

Our findings are supported by two independent studies [41-43], which validate the ν_3 band strength of the *trans* conformer using its absorption cross section in the ultraviolet region near 340-380 nm. Moreover, ambient observations from the Study of Houston Atmospheric Radical Precursor campaign (Apr-May, 2009) show total HONO measurements using the *cis* absorption lines between 1659.45 and 1659.75 cm^{-1} agree to within 6% of those made by three other independent instruments. Detailed analysis on the HONO inter-comparison is being prepared by *J. Pinto et al.* (personal communication). The results here, however, are inconsistent with those of *Becker et al.* [44], which report effective strengths of nine absorption lines near 1255 cm^{-1} (P-branch of *trans* ν_3 mode) that are exactly half of what is expected given the band strengths reported by *Kagann and Maki* [1] and *Maki* [45]. The cause for this discrepancy remains undetermined. A key difference between the current study and that of *Becker et al.* [44] is the

way in which gaseous HONO was quantified. Whereas in the present work, HONO was simultaneously measured by complete conversion followed by continuous NO quantification by calibrated absorption spectroscopy, *Becker et al*. [44] extracted gaseous HONO in a basic liquid trap followed by ion chromatography to quantify the nitrite ion.

Upon rescaling the *cis* ν_2 KMH band using the region between 1650 and 1670 cm^{-1} as a guide to match the S04 spectrum, the values obtained here are still about a factor of 1.4 less than the rescaled KMH line strengths. This is likely due to missing absorption lines resulting from spectral interference in the KMH linelist. This would require scaling existing lines higher than the actual values to compensate for those missing. That there are missing lines in the KMH linelist is evident in the marked difference in the KMH and S04 spectra in the wings of both *cis* and *trans* ν_2 modes (figure 5). Lastly, we note the band strengths of *Kagann and Maki* [1] are based on experimental condition at 296 K, whereas values reported here were obtained at 303 K. Normalizing to the nominal temperature of 296 K – depending on which *cis*/*trans* energy difference is used – changes these values by at most 2%.

5.4. Improving atmospheric measurements

Our current detection limit (1-sec 3-σ) for quantifying total HONO using cw-QC TILDAS is 300 ppt, scanning the *cis* absorption lines near 1660 cm^{-1} and utilizing an astigmatic multi-pass sample cell with a total absorption path length of 210 m at a cell pressure of 30 torr [33]. In addition to increasing the absorption path length or improving the background electronic noise associated with the detector, sensitivity (*i.e*. absorbance) can be enhanced by choosing a spectral region in which HONO absorbs light more strongly. In light of our results and using the KMH linelist as a guide, a factor of about 2 improvement in precision can be readily achieved by

targeting absorption lines for the *trans* conformer at 1247.16 (P-branch of ν_2 mode) or 1273.60 cm^{-1} (R-branch of ν_2 mode), as these lines are relatively free of spectral interference from water vapor and other known absorbers. Precision (1-sec 3-σ) as low as 60 ppt may be obtained under the same conditions with *trans* conformer absorption lines at 1709.00 or 1713.51 cm^{-1} (R-branch of ν_2 mode), for which there is good agreement between the KMH and S04 spectra (figure 5).

A targeted line-by-line study such as the one conducted here is likely required, however, for better accuracy in the retrieved HONO concentrations obtained from these less-studied spectral regions. Figures 4 shows that while on average our *trans*-HONO line strengths agree well with those in the KMH linelist, there may be a difference as high as 17% for a single discernible absorption peak. Discrepancies are more frequent in spectral regions where there is close overlap of absorption lines, pointing to the limited resolution of the KMH linelist. Furthermore, assessments of absorption parameters including the temperature dependence of isomerization and the air-broadened halfwidth are required for remotely measuring HONO and for its inclusion in linelist compilations such as HITRAN [31].

The assertion here that the *cis* ν_2 band strength of *Kagann and Maki* [1] is too high by a factor of about 2.4 implies that previous measurements of HONO concentrations in aircraft exhaust [29] and references therein, should be adjusted accordingly. Examination of Table 1 of ref. [29] shows that correction by a factor of 2.4 of the measurements that utilized the *cis* ν_2 band strength [1], brings them closer to the range observed by measurements that used line strengths that are consistent with the *trans* ν_2 [29] and ν_3 [25] band strengths.

5.5. Conclusion

We report *effective* line strengths for the *cis* and *trans* conformers of HONO. Absorbance of each conformer was recorded using multiple TILDAS systems equipped with cw-QC lasers, while simultaneously quantifying total HONO by catalytic conversion to NO. Line strengths obtained in this study for the *trans* conformer near the 1275 cm^{-1} spectral region are in good agreement with the previously reported *trans* ν_3 band strength [1], confirmed by two independent studies by comparison to the UV absorption cross section [41-43]. Line strengths for the *cis* conformer at 1660 cm^{-1} are, however, lower than reported *cis* ν_2 band strength [1] by about a factor of 2.4. The reason for the *cis* ν_2 line/band strength discrepancy, we submit, is the presence of interfering absorption lines from chemical species other than HONO in the spectra obtained in previous studies [1].

Acknowledgments

This project was funded by the National Science Foundation (Awards No. AGS – 0813617 and 0814202). The authors gratefully acknowledge M. Herman for his contribution of the high resolution FTIR HONO spectrum, and C. Wey for loaning us his NO calibration tank. We would also like to thank J. Kleffmann, T. J. Johnson and S. W. Sharpe for their insights and feedback.

References

[1] Kagann, RH and Maki AG, *Infrared-Absorption Intensities of Nitrous-Acid (Hono) Fundamental Bands*. Journal of Quantitative Spectroscopy & Radiative Transfer, 1983. **30**(1): p. 37-44.

[2] Platt, U, Perner D, Harris GW, Winer AM, and Pitts JN, *Observations of Nitrous-Acid in an Urban Atmosphere by Differential Optical-Absorption*. Nature, 1980. **285**(5763): p. 312-14.

[3] Winer, AM and Biermann HW, *Long Pathlength Differential Optical-Absorption Spectroscopy (Doas) Measurements of Gaseous Hono, No2 and Hcho in the California South Coast Air Basin*. Research on Chemical Intermediates, 1994. **20**(3-5): p. 423-45.

[4] Alicke, B, Geyer A, Hofzumahaus A, Holland F, Konrad S, Patz HW, Schafer J, Stutz J, Volz-Thomas A, and Platt U, *OH formation by HONO photolysis during the BERLIOZ experiment*. Journal of Geophysical Research-Atmospheres, 2003. **108**(D4): p. -.

[5] Harris, GW, Carter WPL, Winer AM, Pitts JN, Platt U, and Perner D, *Observations of Nitrous-Acid in the Los-Angeles Atmosphere and Implications for Predictions of Ozone Precursor Relationships*. Environmental Science & Technology, 1982. **16**(7): p. 414-19.

[6] Ren, XR, Harder H, Martinez M, Lesher RL, Oliger A, Simpas JB, Brune WH, Schwab JJ, Demerjian KL, He Y, Zhou XL, and Gao HG, *OH and HO2 chemistry in the urban atmosphere of New York City*. Atmospheric Environment, 2003. **37**(26): p. 3639-51.

[7] Acker, K, Moller D, Wieprecht W, Meixner FX, Bohn B, Gilge S, Plass-Dulmer C, and Berresheim H, *Strong daytime production of OH from HNO2 at a rural mountain site*. Geophysical Research Letters, 2006. **33**(2): p. -.

[8] Kleffmann, J, Gavriloaiei T, Hofzumahaus A, Holland F, Koppmann R, Rupp L, Schlosser E, Siese M, and Wahner A, *Daytime formation of nitrous acid: A major source of OH radicals in a forest*. Geophysical Research Letters, 2005. **32**(5).

[9] Sorgel, M, Trebs I, Serafimovich A, Moravek A, Held A, and Zetzsch C, *Simultaneous HONO measurements in and above a forest canopy: influence of turbulent exchange on mixing ratio differences*. Atmospheric Chemistry and Physics, 2011. **11**(2): p. 841-55.

[10] Zhou, XL, Zhang N, TerAvest M, Tang D, Hou J, Bertman S, Alaghmand M, Shepson PB, Carroll MA, Griffith S, Dusanter S, and Stevens PS, *Nitric acid photolysis on forest canopy surface as a source for tropospheric nitrous acid*. Nature Geoscience, 2011. **4**(7): p. 440-43.

[11] Beine, HJ, Amoroso A, Esposito G, Sparapani R, Ianniello A, Georgiadis T, Nardino M, Bonasoni P, Cristofanelli P, and Domine F, *Deposition of atmospheric nitrous acid on alkaline snow surfaces*. Geophysical Research Letters, 2005. **32**(10).

[12] Honrath, RE, Lu Y, Peterson MC, Dibb JE, Arsenault MA, Cullen NJ, and Steffen K, *Vertical fluxes of NOx, HONO, and HNO3 above the snowpack at Summit, Greenland*. Atmospheric Environment, 2002. **36**(15-16): p. 2629-40.

[13] Zhou, XL, Beine HJ, Honrath RE, Fuentes JD, Simpson W, Shepson PB, and Bottenheim JW, *Snowpack photochemical production of HONO: a major source of OH in the Arctic boundary layer in springtime*. Geophysical Research Letters, 2001. **28**(21): p. 4087-90.

[14] Beckett, WS, Russi MB, Haber AD, Rivkin RM, Sullivan JR, Tameroglu Z, Mohsenin V, and Leaderer BP, *Effect of Nitrous-Acid on Lung-Function in Asthmatics - a Chamber Study*. Environmental Health Perspectives, 1995. **103**(4): p. 372-75.

[15] Jarvis, DL, Leaderer BP, Chinn S, and Burney PG, *Indoor nitrous acid and respiratory symptoms and lung function in adults*. Thorax, 2005. **60**(6): p. 474-79.

[16] Pitts, JN, Grosjean D, Vancauwenberghe K, Schmid JP, and Fitz DR, *Photo-Oxidation of Aliphatic-Amines under Simulated Atmospheric Conditions - Formation of Nitrosamines, Nitramines, Amides, and Photo-Chemical Oxidant*. Environmental Science & Technology, 1978. **12**(8): p. 946-53.

[17] Sleiman, M, Gundel LA, Pankow JF, Jacob P, Singer BC, and Destaillats H, *Formation of carcinogens indoors by surface-mediated reactions of nicotine with nitrous acid, leading to potential thirdhand smoke hazards*. Proceedings of the National Academy of Sciences of the United States of America, 2010. **107**(15): p. 6576-81.

[18] Dibb, JE, Huey LG, Slusher DL, and Tanner DJ, *Soluble reactive nitrogen oxides at South Pole during ISCAT 2000*. Atmospheric Environment, 2004. **38**(32): p. 5399-409.

[19] Kleffmann, J, Heland J, Kurtenbach R, Lorzer J, and Wiesen P, *A new instrument (LOPAP) for the detection of nitrous acid (HONO)*. Environmental Science and Pollution Research, 2002: p. 48-54.

[20] Park, SS, Hong JH, Lee JH, Kim YJ, Cho SY, and Kim SJ, *Investigation of nitrous acid concentration in an indoor environment using an in-situ monitoring system*. Atmospheric Environment, 2008. **42**(27): p. 6586-96.

[21] Zhou, XL, Qiao HC, Deng GH, and Civerolo K, *A method for the measurement of atmospheric HONO based on DNPH derivatization and HPLC analysis*. Environmental Science & Technology, 1999. **33**(20): p. 3672-79.

[22] Kleffmann, J, Lorzer JC, Wiesen P, Kern C, Trick S, Volkamer R, Rodenas M, and Wirtz K, *Intercomparison of the DOAS and LOPAP techniques for the detection of nitrous acid (HONO)*. Atmospheric Environment, 2006. **40**(20): p. 3640-52.

[23] Liao, W, Case AT, Mastromarino J, Tan D, and Dibb JE, *Observations of HONO by laser-induced fluorescence at the South Pole during ANTCI 2003*. Geophysical Research Letters, 2006. **33**(9): p. -.

[24] Stutz, J, Alicke B, and Neftel A, *Nitrous acid formation in the urban atmosphere: Gradient measurements of NO2 and HONO over grass in Milan, Italy*. Journal of Geophysical Research-Atmospheres, 2002. **107**(D22).

[25] Lee, BH, Santoni GW, Wood EC, Herndon SC, Miake-Lye RC, Zahniser MS, Wofsy SC, and Munger JW, *Measurements of Nitrous Acid in Commercial Aircraft Exhaust at the Alternative Aviation Fuel Experiment*. Environmental Science & Technology, 2011. **45**(18): p. 7648-54.

[26] Li, YQ, Schwab JJ, and Demerjian KL, *Fast time response measurements of gaseous nitrous acid using a tunable diode laser absorption spectrometer: HONO emission source from vehicle exhausts*. Geophysical Research Letters, 2008. **35**(4): p. -.

[27] Schiller, CL, Locquiao S, Johnson TJ, and Harris GW, *Atmospheric measurements of HONO by tunable diode laser absorption spectroscopy*. Journal of Atmospheric Chemistry, 2001. **40**(3): p. 275-93.

[28] Wood, EC, Herndon SC, Timko MT, Yelvington PE, and Miake-Lye RC, *Speciation and chemical evolution of nitrogen oxides in aircraft exhaust near airports*. Environmental Science & Technology, 2008. **42**(6): p. 1884-91.

[29] Wormhoudt, J, Herndon SC, Yelvington PE, Miake-Lye RC, and Wey C, *Nitrogen oxide (NO/NO2/HONO) emissions measurements in aircraft exhausts*. Journal of Propulsion and Power, 2007. **23**(5): p. 906-11.

[30] Brown, LR, Farmer CB, Rinsland CP, and Toth RA, *Molecular Line Parameters for the Atmospheric Trace Molecule Spectroscopy Experiment*. Applied Optics, 1987. **26**(23): p. 5154-82.

[31] Rothman, LS, Gordon IE, Barbe A, Benner DC, Bernath PE, Birk M, Boudon V, Brown LR, Campargue A, Champion JP, Chance K, Coudert LH, Dana V, Devi VM, Fally S, Flaud JM, Gamache RR, Goldman A, Jacquemart D, Kleiner I, Lacome N, Lafferty WJ, Mandin JY, Massie ST, Mikhailenko SN, Miller CE, Moazzen-Ahmadi N, Naumenko OV, Nikitin AV, Orphal J, Perevalov VI, Perrin A, Predoi-Cross A, Rinsland CP, Rotger M, Simeckova M, Smith MAH, Sung K, Tashkun SA, Tennyson J, Toth RA, Vandaele AC, and Vander Auwera J, *The HITRAN 2008 molecular spectroscopic database*. Journal of Quantitative Spectroscopy & Radiative Transfer, 2009. **110**(9-10): p. 533-72.

[32] Sironneau, V, Flaud JM, Orphal J, Kleiner I, and Chelin P, *Absolute line intensities of HONO and DONO in the far-infrared and re-determination of the energy difference between the trans- and cis-species of nitrous acid*. Journal of Molecular Spectroscopy, 2010. **259**(2): p. 100-04.

[33] Lee, BH, Wood EC, Zahniser MS, McManus JB, Nelson DD, Herndon SC, Santoni GW, Wofsy SC, and Munger JW, *Simultaneous measurements of atmospheric HONO and NO2 via absorption spectroscopy using tunable mid-infrared continuous-wave quantum cascade lasers*. Applied Physics B-Lasers and Optics, 2011. **102**(2): p. 417-23.

[34] Nelson, DD, Shorter JH, McManus JB, and Zahniser MS, *Sub-part-per-billion detection of nitric oxide in air using a thermoelectrically cooled mid-infrared quantum cascade laser spectrometer*. Applied Physics B-Lasers and Optics, 2002. **75**(2-3): p. 343-50.

[35] Angeletti, G, Restelli G, Commission of the European Communities. Joint Research Centre. Ispra Establishment., and Commission of the European Communities. Directorate-General for Science Research and Development., *Physico-chemical behaviour of atmospheric pollutants : proceedings of the fourth European symposium held in Stresa, Italy, 23-25 September 1986 ; organized within the framework of the Concerted Action COST 611*. Air pollution research report 2. 1987, Dordrecht ; Boston Norwell, MA, U.S.A.: D. Reidel Pub. Co. ; Sold and distributed in the U.S.A. and Canada by Kluwer Academic Publishers. xiii, 809 p.

[36] Febo, A, Perrino C, Gherardi M, and Sparapani R, *Evaluation of a High-Purity and High-Stability Continuous Generation System for Nitrous-Acid*. Environmental Science & Technology, 1995. **29**(9): p. 2390-95.

[37] Wingen, LM, Barney WS, Lakin MJ, Brauers T, and Finlayson-Pitts BJ, *A unique method for laboratory quantification of gaseous nitrous acid (HONO) using the reaction HONO+HCl -> ClNO+H2O*. Journal of Physical Chemistry A, 2000. **104**(2): p. 329-35.

[38] Harward, CN, Baren RE, and Parrish ME, *Determination of molecular parameters for 1,3-butadiene and propylene using infrared tunable diode laser absorption spectroscopy*. Spectrochimica Acta Part a-Molecular and Biomolecular Spectroscopy, 2004. **60**(14): p. 3421-29.

[39] Sharpe, SW, Johnson TJ, Sams RL, Chu PM, Rhoderick GC, and Johnson PA, *Gas-phase databases for quantitative infrared spectroscopy*. Applied Spectroscopy, 2004. **58**(12): p. 1452-61.

[40] Hall, RT and Pimentel GC, *Isomerization of Nitrous Acid - an Infrared Photochemical Reaction*. Journal of Chemical Physics, 1963. **38**(8): p. 1889-&.

[41] Barney, WS, Wingen LM, Lakin MJ, Brauers T, Stutz J, and Finlayson-Pitts BJ, *Infrared absorption cross-section measurements for nitrous acid (HONO) at room temperature*. Journal of Physical Chemistry A, 2000. **104**(8): p. 1692-99.

[42] Barney, WS, Wingen LM, Lakin MJ, Brauers T, Stutz J, and Finlayson-Pitts BJ, *Infrared absorption cross-section measurements for nitrous acid (HONO) at room temperature (vol 104A, pg 1692, 2000)*. Journal of Physical Chemistry A, 2001. **105**(16): p. 4166-66.

[43] Gratien, A, Lefort M, Picquet-Varrault B, Orphal J, Doussin JF, and Flaud JM, *Experimental intercomparison of the absorption cross-sections of nitrous acid (HONO) in the ultraviolet and mid-infrared spectral regions*. Journal of Quantitative Spectroscopy & Radiative Transfer, 2009. **110**(4-5): p. 256-63.

[44] Becker, KH, Kleffmann J, Kurtenbach R, and Wiesen P, *Line-Strength Measurements of Trans-Hono near 1255 Cm(-1) by Tunable Diode-Laser Spectrometry*. Geophysical Research Letters, 1995. **22**(18): p. 2485-88.

[45] Maki, AG, *High-Resolution Measurements of the Nu-2 Band of Hno3 and the Nu-3 Band of Trans-Hono*. Journal of Molecular Spectroscopy, 1988. **127**(1): p. 104-11.

Chapter 6:

Urban measurements of atmospheric nitrous acid: an alternative assessment of secondary day and nighttime production[5]

Abstract

Numerous studies infer the existence of an "unknown" HONO source from measuring the rate of HONO losses by photolysis and OH-oxidation that exceed production by the gas-phase reaction between NO and OH. Production rates as high as 1.1 ppb hr^{-1} from a secondary source are needed to close this imbalance for photostationary state (PSS), based on measurements obtained during the SHARP campaign in May of 2009. We argue, however, that the PSS assumption of no net production or loss of HONO was not valid because the transport time from nearby emission sources to the measurement site was short relative to HONO's lifetime. Using a chemical box model, we demonstrate that there is initially net HONO formation in fresh exhaust as NO – the main component of vehicle-derived NO_x emissions – rapidly reacts with ambient OH. Production is followed by a period of net HONO loss, that is sustained on the order of several minutes to hours depending on solar radiation. The presence of relatively fresh diluted vehicle exhaust can in part, if not fully, account for this measured imbalance. We also show that a large fraction of the observed increase in HONO:NO_x ratio at night can be explained by NO_2 oxidation.

6.1. Introduction

[5] Lee, B. H., Wood, E. C., Herndon, S. C., Lefer, B. L., Luke, W. T., Brune, W. H., Nelson, D. D., Zahniser, M. S., J. W. Munger, *to be submitted to Geophysical Research Letters*.

The three gas-phase reactions that are typically considered to govern daytime HONO levels – ignoring heterogeneous chemistry – are formation by the reaction (R1) between nitric oxide (NO) and the hydroxyl radical (OH), and losses by photolysis (R2) and oxidation (R3) by OH.

R1)	$OH + NO + M \rightarrow HONO + M$	k_1
R2)	$HONO + h\nu \rightarrow OH + NO$	J_{HONO}
R3)	$HONO + OH \rightarrow H_2O + NO_2$	k_3

At photostationary state (PSS), the net time rate of concentration change due to chemistry is zero. Observations of negative net rates – considering only reactions 1-3 and invoking PSS – have been interpreted as evidence of an unaccounted HONO source [*Alicke et al*., 2002; *Alicke et al*., 2003; *Neftel et al*., 1996; *Sorgel et al*., 2011; *Staffelbach et al*., 1997; *Wong et al*., 2012], as represented by P^* in equation 1 (E1). Numerous formation pathways – the magnitude of which is given by equation 2 (E2) – have been proposed to reconcile the observed imbalance between production (R1) and loss (R2+R3), including heterogeneous reaction enhanced by photo-excited organics [*Stemmler et al*., 2006], long-wave photolysis of nitrogen dioxide (NO_2) [*Li et al*., 2008], direct release of HONO from soil due to excess nitrite ions [*Su et al*., 2011], production on aerosol/soot/TiO_2 surfaces [*Ammann et al*., 1998; *Langridge et al*., 2009; *Monge et al*., 2010; *Stemmler et al*., 2007] and heterogeneous nitrate ion photolysis [*Zhou et al*., 2011; *Ziemba et al*., 2010].

(E1) $$\frac{d[HONO]}{dt} = P^* + k_1[OH][NO] - J_{HONO}[HONO] - k_3[OH][HONO] = 0$$

$$P^* = J_{HONO}[HONO] + k_3[OH][HONO] - k_1[OH][NO] \quad \text{(E2)}$$

, where the concentrations of OH, NO and HONO and J_{HONO} are observed quantities.

Urban HONO levels – measured by a variety of detection techniques – indicate it to be a significant source of daytime radicals [*Mao et al*., 2010; *Ren et al*., 2003; *Ren et al*., 2006; *Su et al*., 2008; *Vogel et al*., 2003]. Photolysis of HONO formed by any pathway not involving OH or the hydroperoxyl radical (HO_2) constitutes a net source of HO_x (=OH+HO_2). Whereas previous studies point to secondary production based on the PSS assumption, we propose that air masses sampled during SHARP (and perhaps at other urban locations) are not in photostationary balance for HONO, based on its atmospheric lifetime and conservatively-estimated transport time from emission sources surrounding the site. Using a chemical box model, we demonstrate that appreciable net HONO loss persists long enough that influence from fresh vehicle exhaust can, at least in part, account for the observed imbalance from PSS.

Lastly, nighttime accumulation of HONO – which initiates photochemistry in the early morning prior to other HO_x precursors [*Winer and Biermann*, 1994] – has largely been attributed to NO_2-driven heterogeneous reaction with minor contribution from direct emissions, by using the HONO:NO_x ratio as a conserved tracer [*Pitts et al*., 1984; *Platt et al*., 1980; *Wong et al*., 2012; *Yu et al*., 2009]. Previous studies, however, failed to account for nighttime NO_x oxidation and deposition, both of which can influence the HONO:NO_x ratio.

6.2. Field Measurements

We present gaseous HONO and NO_2 mixing ratios measured atop the North Moody Tower on the University of Houston (UH) campus, situated approximately 5 km southeast of downtown

Houston (latitude: 29.72°, longitude: -95.34°). Measurements were made as part of the Study of Houston Atmospheric Radical Precursors (SHARP) campaign during May of 2009, described by *Lefer et al*. [citation]. Mixing ratios of gaseous HONO and NO_2 were simultaneously quantified using a dual tunable infrared quantum cascade laser absorption spectrometer. Ambient air was drawn from the top of a four-story scaffolding tower through a custom-built quartz inlet, connected by 30 feet (9.2 m) of 3/8 inch (9.5 mm) outer diameter perfluoroalkoxy (PFA) tubing to the spectrometer, which was housed in a temperature-controlled shed on the roof of the 18-story building. The inlet design removed particles larger than about 4 microns from the sample stream by inertial separation, obviating the need for inlet filters. A critical orifice at the inlet reduced the pressure to about 0.5 bar. Both the inlet and tubing were heated to 35°C and covered by opaque materials. The combination of reduced pressure and heating above ambient temperature was designed to minimize the presence of aqueous films in the sample line. In-field tests conducted during the course of ambient measurements checked for possible artifacts and interferences resulting from the sampling technique. Routine additions of humidity-matched zero-air and gaseous HONO and NO_2 consistently showed equal response times for HONO and NO_2 through the inlet, tubing and sample cell, indicating no reversible loss of HONO during sampling. Additions from a stable source of HONO in laboratory studies exhibited no instantaneous loss due to either the inlet or the tubing. Introducing NO_2 levels >200 ppb mixed with ambient Houston air under conditions conducive to heterogeneous chemistry (*i.e*. unheated tubing, sample near ambient pressure), showed no evidence of HONO production (figure 6 in *Lee et al*. [2011]). The sample residence (1/e) times in the inlet, tubing and cell were on average 0.3, 0.2 and 1.3 seconds, respectively, at a total flow rate of approximately 10 standard liters per minute. During SHARP, the instrumental detection limits (3σ) with one hour spectral averaging

were 40 ppt and 10 ppt (pmol/mol) for HONO and NO_2, respectively. Typical half-hour averaged absorbance spectra obtained by the two lasers during the campaign are shown in the supplemental section (Supplementary figure B4). Additional details on instrument performance, sampling technique and mixing ratio time-series of HONO and NO_2 observed during SHARP are presented by *Lee et al*. [2011].

Quantification of HONO in the field relied on the accuracy of mid-infrared line strengths obtained in the laboratory by measuring the absorbance of HONO by the spectrometer while quantifying HONO by complete catalytic conversion to NO, followed by calibrated absorption spectroscopy [*Lee et al*., 2012]. Comparison to other HONO measurements included in the SHARP campaign corroborates the accuracy of TILDAS. Ambient observations during the campaign by four unique point-measurement instruments showed agreement to within 6% considering all time-matched data. A long path-averaged differential optical absorption spectroscopy (DOAS) measurement was typically lower than the point measurement methods, particularly in the early morning hours, likely due to heterogeneity along the DOAS absorption path that is not represented by the point measurements. Detailed analyses on the inter-comparison will be presented by *J. Pinto* (personal communication).

The other variables utilized in the present analysis include measurements of OH by laser-induced fluorescence [*Faloona et al*., 2004; *Mao et al*., 2010], NO by ozone-chemiluminescence [*Luke et al*., 2010] and HONO photolysis rates, derived from measured NO_2 photolysis rates using the parameterization of *Kraus and Hofzumahaus* [1998]. All three *in situ* measurements were obtained by instruments co-located with the HONO inlet on the scaffolding tower. Additional details regarding the SHARP campaign are presented elsewhere [*Lefer et al*., in preparation].

6.3. Results

During SHARP, the measured HONO levels typically exceeded values calculated by assuming PSS between reactions 1-3 (figure 1a). By definition, measured levels are underestimated by PSS-approximated levels when d[HONO]/dt (E1, with $P^* = 0$) is negative and overestimated when positive (figure 1b). At photostationary state, observed HONO ($[HONO]_{Obs}$) concentrations that are greater than those at PSS ($[HONO]_{PSS}$), suggests unaccounted HONO production and/or overestimation of loss. However, for the PSS approximation to be valid, the time to observation – or reaction time since emission/production – must be several times longer than the atmospheric lifetime of the species being considered [*Steinfeld et al*., 1989; *Turanyi et al*., 1993; *Wayne*, 2000]. The lifetime, τ, defined as the inverse sum of the loss rates (E3), ranged from about ten minutes at midday to several hours during the early morning/late afternoon periods for HONO (Supplementary figure B5).

$$\tau = \frac{1}{\sum_k k_i} = \frac{1}{J_{HONO} + k_2[OH]} \qquad \text{(E3)}$$

The UH campus is approximately 5 km southeast of the center of Houston, where the majority of population is largely confined within a roughly 20 km radius, and is within 5 km of major freeways in all directions. Assuming that emission sources located within 10 km of the site are responsible for the observed enhancements of HONO and NO_x mixing ratios, the mean transport time for the emitted species is approximately 30 minutes given SHARP-averaged daytime wind speed of 5.5 m sec^{-1}. In actuality, sampled air masses are influenced by many

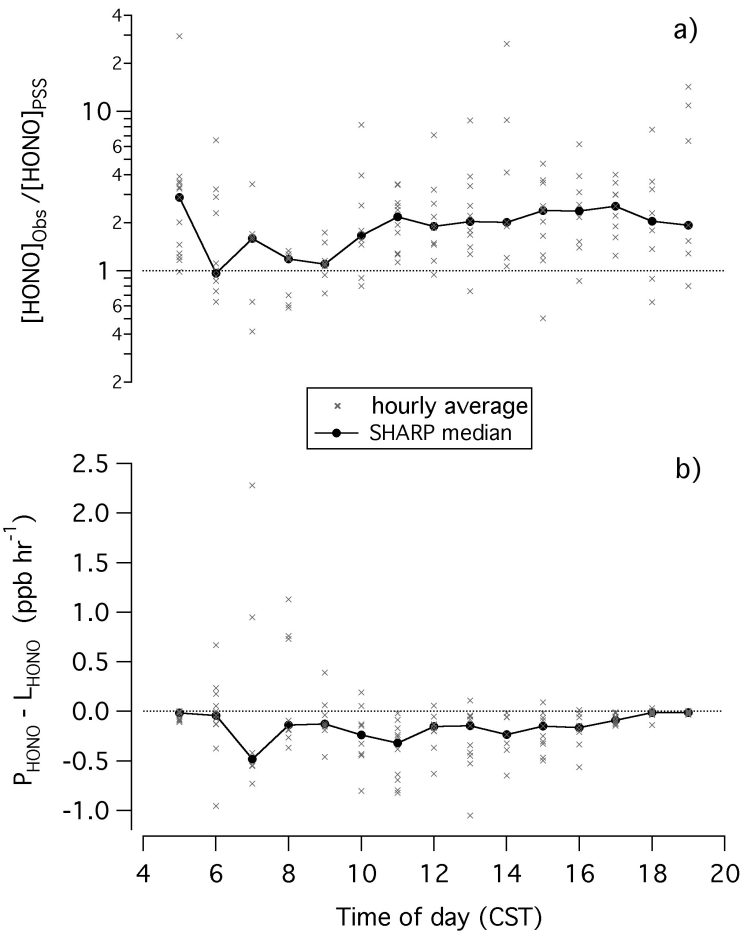

Figure 6.1. a) Small grey symbols show the hourly-averaged measured:PSS ratio and b) sum of HONO production (R1) and loss rates (R2+R3), both plotted as a function of time of day (CST). The large black line-connected markers represent the overall median for each daytime hour during the SHARP campaign.

emission sources during their recent history, resulting in a complex distribution of photochemical ages.

We use a chemical box model to estimate the time rate of change of HONO concentration in vehicle exhaust, the dominant source of nitrogen oxides in the region, as it mixes with NO_x-free background air. HONO mixing ratios were calculated in two ways; by numerical integration ($[HONO]_{time\text{-}integrated}$) and by assuming instantaneous PSS between reactions 1-3 at each time step ($[HONO]_{instantaneous\text{-}PSS}$). Simulations were conducted over observed ranges of OH and J_{HONO} – the two variables driving HONO loss. Reactions 1-6 were considered, with rates for 298 K [*Atkinson et al*., 2004; *Sander et al*., 2011]. The initial $NO/NO_2/HONO$ distribution (0.95/0.042/0.008) in exhaust was obtained from *Kurtenbach et al*. [2001]. Absolute initial concentrations did not affect the simulated ratio. Variation in the numerical integration time steps from 0.1 to 10 seconds, likewise, had no effect. Due to the titration of ambient OH and O_3 by NO in fresh exhaust and the rapid regeneration of OH from photolysis of concentrated HONO, four scenarios were considered to capture the range of possible conditions during initial mixing; i) constant OH (simulation value) and constant O_3 (50 ppb), ii) constant OH with O_3 linearly increasing in time from 0 ppb (t=0) to 50 ppb (t=5 min), iii) OH starting at double the simulation value (t=0) and decreasing linearly to simulation value (t=5 min) with constant O_3 (50 ppb), and iv) both OH and O_3 varying in time.

R4) $NO + O_3 \rightarrow NO_2 + O_2$ k_4

R5) $NO_2 + h\nu \rightarrow NO + O$ k_5

R6) $NO_2 + OH + M \rightarrow HNO_3 + M$ k_6

For all cases, there is initially net production of HONO by reaction 1 (R1). Figures 2a and 2b show that as NO is depleted by reaction with O_3 (R4), a short period (on the order of a few minutes) of net HONO production (from R1) is followed by a longer period (on the order of several minutes to hours) of net HONO loss (from R2 and R3), demonstrating persistent nonzero net rate of change of HONO concentration. Production of HONO is faster if initial O_3 levels are low (case ii) or if initial OH levels are high (case iii) due to their effects on NO. Figure 3 shows the time-integrated:instantaneous-PSS HONO ratios following a reaction time since emission that was assigned randomly with a Gaussian distribution of 30±10 minutes (figure 2d) to represent the complex mixture of photochemical ages sampled. Results in figure 3 are of case ii, determined for 40,000 different combination of OH and J_{HONO} values. The simulated ratio under midday conditions is approximately 1.3 and increases with lower OH and J_{HONO} values. If initial OH levels are low due to slow photolysis and/or suppression by high NO, then there is initially net HONO loss (R1) followed by a period of lower net loss or even net production as OH reacts with excess NO. For instance, the time period between 06:00 and 09:00 – characterized by morning emissions within a shallow mixing layer – experienced anomalously high net HONO loss ($d[HONO]/dt < 0$) on some days and production ($d[HONO]/dt > 0$) on others (figure 1b), likely depending on the history of OH in the sampled air mass and extent of chemical processing at the time of sampling. Moreover, the net rate (figure 1b) – outside of the morning rush hour – exhibited a diurnal trend, which may be evidence of photo-driven secondary HONO production [*Wong et al.*, 2012] or may simply reflect the sunlight dependence of reactions 1-3.

HONO for all cases approaches steady state following a perturbation period, the time that the model allows for OH and O_3 to reach their respective steady state values and which dictates approximately the time since emission when the maximum time-integrated:instantaneous-PSS

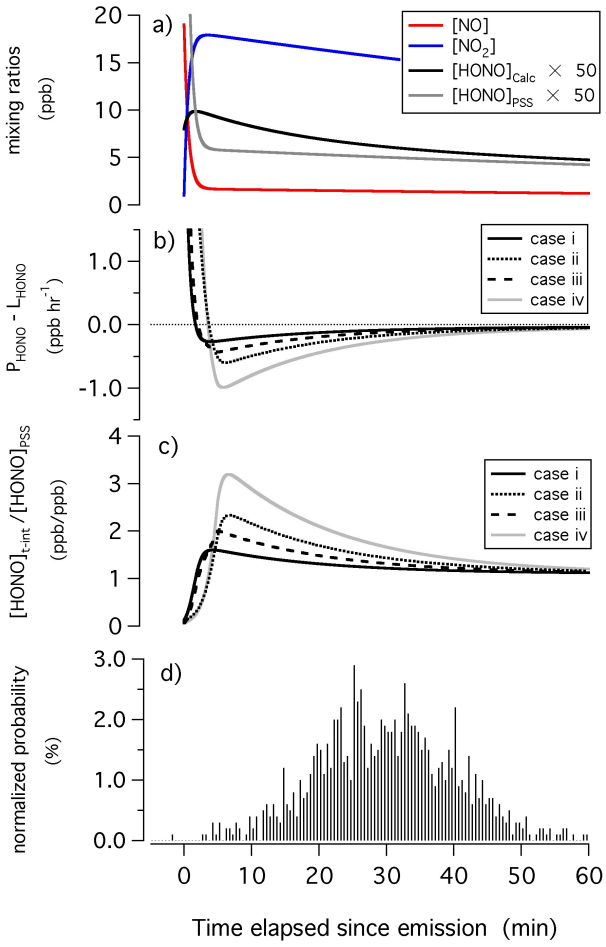

Figure 6.2. Simulated time-series of (a) [NO], [NO_2], $[HONO]_{time\text{-}integrated}$ and $[HONO]_{instantaneous\text{-}PSS}$ in vehicle exhaust for constant [OH] = 0.5 ppt and constant [O_3] = 30 ppb, (b) sum of the production (R1) and loss (R2+R3) rates of HONO and (c) the ratio of time-integrated:instantaneous-PSS HONO for the four cases. (d) Probability distribution of the age of air mass that was assigned to each simulation, the result of which is summarized in figure 3.

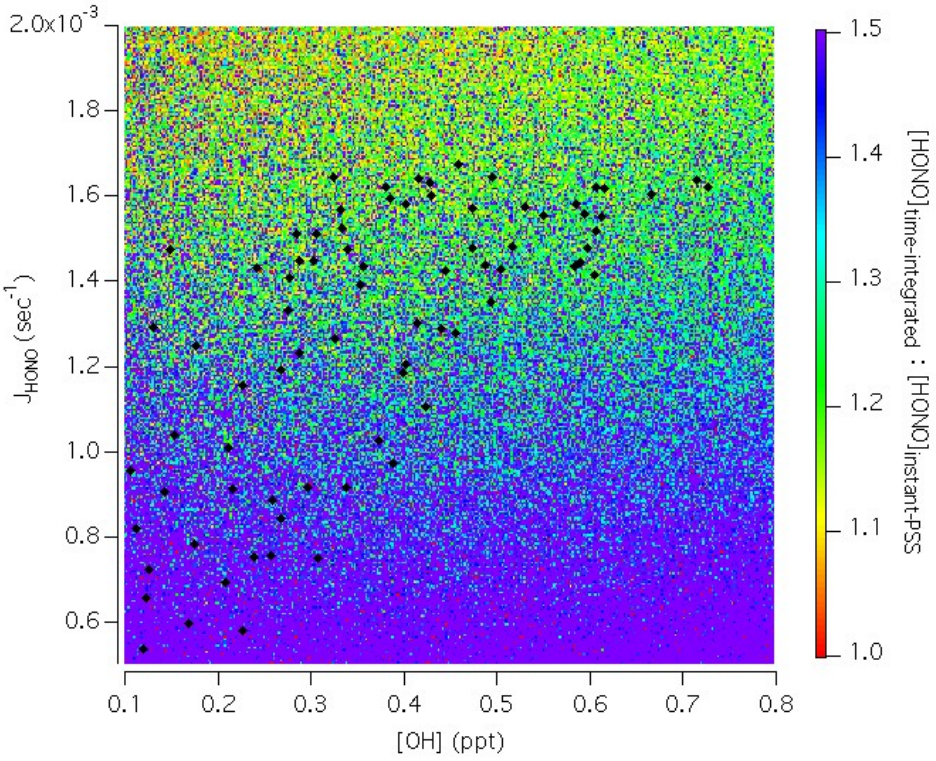

Figure 6.3. The color contours show the ratio of time-integrated:instantaneous-PSS HONO mixing ratios of vehicle exhaust following a time period that was randomly assigned from a Gaussian probability distribution centered at 30±10 minutes (figure 2d). Results here are plotted as a function of OH and J_{HONO}, both of which were held constant throughout each simulation (case ii). The black markers represent OH and J_{HONO} observed during SHARP.

ratio is encountered. Variation in its absolute value – set arbitrarily as five minutes to represent the time required for complete entrainment of background air – has minor effects on the degree of departure from steady state. Considering that the duration of a nonzero net rate of HONO change is inversely proportional to its lifetime, the main implication is that both the extent and duration of deviation from steady state are sensitive to the age of the sampled air mass since emission and photochemical conditions within the plume and of the ambient atmosphere. Daytime HONO concentrations observed during SHARP (and at other urban measurement sites) were frequently greater than those predicted for PSS of reactions 1-3. This analysis shows that reaction R1 can significantly – if not entirely – account for the persistent nonzero net HONO loss rate due to continued entrainment of fresh emissions.

The observed HONO:NO_x ratio increased during most nights (Figure 4a). Previous studies have attributed similar observations to NO_2-fueled heterogeneous HONO production on the ground [*Wong et al*., 2011] or aerosol [*Yu et al*., 2009] surfaces. Direct emissions were discounted when estimating production rates because observed HONO:NO_x ratios exceeded those reported in fresh vehicle exhaust. However, neither the chemical processing of directly-emitted NO_x nor its deposition, the presumed source of HONO production, were taken into account. We consider nocturnal chemistry of NO_x associated with NO_3 and N_2O_5 formation (R7-R12) in a box model to estimate HONO production per deposited NO_2 of a stagnant nighttime air mass.

R7) $NO + O_3 \rightarrow NO_2 + O_2$ k_7

R8) $NO_2 + O_3 \rightarrow NO_3 + O_2$ k_8

R9) $NO + NO_3 \rightarrow NO_2 + NO_2$ k_9

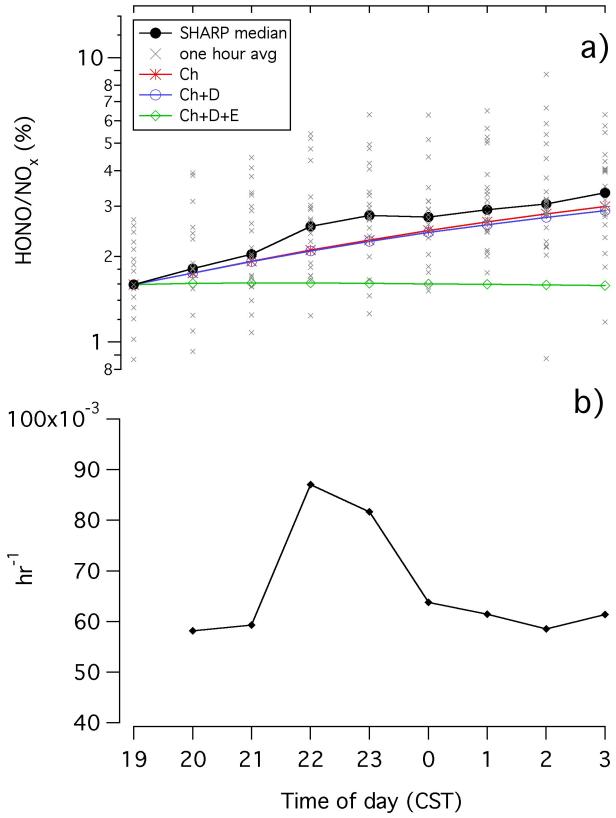

Figure 6.4. (a) Observed (black circles) and modeled (red = chemistry only; blue = chemistry + deposition; green = chemistry + deposition + emissions) HONO:NO_x ratio plotted starting at 19:00 (CST). (b) HONO production rate per NO_2 deposited per time, calculated as the difference between observed (black) and modeled (green), after accounting for NO_x chemistry, deposition and emission.

R10) $NO_2 + NO_3 + M \rightarrow N_2O_5 + M$ k_{10}

R11) $N_2O_5 + M \rightarrow NO_2 + NO_3 + M$ k_{11}

Figure 4a shows results from three simulations of HONO:NO_x ratios following nightfall. The initial value at sunset (19:00) for all cases is set to the corresponding observed median ratio (0.016). The nighttime simulations were conducted with O_3 held constant at 30 ppb and ignoring subsequent reactions and deposition of NO_3 and N_2O_5. The base case (shown in red) considers only O_3-initiated NO_x oxidation (R7-R11) and exhibits an increasing trend in HONO:NO_x that is comparable to observed patterns. Including deposition of HONO and NO_2, both with a deposition velocity of 0.1 cm sec^{-1} integrated over a 100 m boundary layer height, does not significantly alter the HONO:NO_x trend (blue line). In both cases, however, the resulting NO_x level decays to about half the initial value mainly due to conversion of NO_x to NO_3 and N_2O_5. Observed NO_x levels, however, do not show consistent nighttime drawdown (Supplementary figure B6). Maintaining a constant simulated NO_x level by replacing the NO_x lost to chemical reaction with fresh emissions that have a HONO:NO_x ratio of 0.008 [*Kurtenbach et al.,* 2001], results in a lower simulated HONO:NO_x trend (green line). We interpret the difference between the median of the SHARP nighttime observations and this modeled scenario that includes chemistry, deposition and emissions as HONO production at the ground surface. Figure 4b shows that the increase in HONO:NO_x not attributable to NO_2 oxidation or NO_x emission is about 1:15 HONO produced per NO_2 deposited per hour, which is about twice the rate of 1:33 reported by *Stutz et al*. [2002]. Given the simplification of the chemistry and assumption of a stagnant air mass, this difference may not be significant.

6.4. Conclusion

We report direct simultaneous measurements of HONO and NO_2 mixing ratios using a tunable infrared laser differential absorption spectrometer. Rigorous in-field and laboratory tests of the sampling scheme demonstrate the absence of positive and negative artifacts. Given the atmospheric lifetime of HONO, we show – based on conservative approximations of chemistry in mixing air parcels and transport times of directly-emitted vehicle exhaust – that air masses sampled during SHARP can sustain a nonzero net rate of HONO change with continued entrainment of fresh vehicle exhaust. A larger fraction of the discrepancy between measured and PSS-assumed levels may be reconciled if initial OH levels in exhaust plume were high (cases iii and iv) or if the actual distribution of photochemical ages is skewed toward younger ages. This analysis points to the importance of explicitly considering the effects of mixing and transport in the near-field, particularly when sampling in relative close proximity to emission sources. Distinguishing between alternate production pathways for HONO and primary production from OH + NO has important implications for determining the net production of HO_x. During nighttime, we show that NO_x oxidation and emissions are significant. Thus NO_x cannot be considered a conservative tracer for using the HONO:NO_x ratio as an indicator of HONO production. We estimate that 1 HONO molecule is emitted from the ground surface per 15 NO_2 molecules deposited per hour.

References

Alicke, B., U. Platt, and J. Stutz (2002), Impact of nitrous acid photolysis on the total hydroxyl radical budget during the Limitation of Oxidant Production/Pianura Padana Produzione di Ozono study in Milan, *Journal of Geophysical Research-Atmospheres*, *107*(D22).

Alicke, B., A. Geyer, A. Hofzumahaus, F. Holland, S. Konrad, H. W. Patz, J. Schafer, J. Stutz, A. Volz-Thomas, and U. Platt (2003), OH formation by HONO photolysis during the BERLIOZ experiment, *Journal of Geophysical Research-Atmospheres*, *108*(D4), -.

Ammann, M., M. Kalberer, D. T. Jost, L. Tobler, E. Rossler, D. Piguet, H. W. Gaggeler, and U. Baltensperger (1998), Heterogeneous production of nitrous acid on soot in polluted air masses, *Nature*, *395*(6698), 157-160.

Atkinson, R., D. L. Baulch, R. A. Cox, J. N. Crowley, R. F. Hampson, R. G. Hynes, M. E. Jenkin, M. J. Rossi, and J. Troe (2004), Evaluated kinetic and photochemical data for atmospheric chemistry: Volume I - gas phase reactions of O(x), HO(x), NO(x) and SO(x) species, *Atmospheric Chemistry and Physics*, *4*, 1461-1738.

Faloona, I. C., D. Tan, R. L. Lesher, N. L. Hazen, C. L. Frame, J. B. Simpas, H. Harder, M. Martinez, P. Di Carlo, X. R. Ren, and W. H. Brune (2004), A laser-induced fluorescence instrument for detecting tropospheric OH and HO2: Characteristics and calibration, *Journal of Atmospheric Chemistry*, *47*(2), 139-167.

Kraus, A., and A. Hofzumahaus (1998), Field measurements of atmospheric photolysis frequencies for O(3), NO(2), HCHO, CH(3)CHO, H(2)O(2), and HONO by UV spectroradiometry, *Journal of Atmospheric Chemistry*, *31*(1-2), 161-180.

Kurtenbach, R., K. H. Becker, J. A. G. Gomes, J. Kleffmann, J. C. Lorzer, M. Spittler, P. Wiesen, R. Ackermann, A. Geyer, and U. Platt (2001), Investigations of emissions and heterogeneous formation of HONO in a road traffic tunnel, *Atmospheric Environment*, *35*(20), 3385-3394.

Langridge, J. M., R. J. Gustafsson, P. T. Griffiths, R. A. Cox, R. M. Lambert, and R. L. Jones (2009), Solar driven nitrous acid formation on building material surfaces containing titanium dioxide: A concern for air quality in urban areas?, *Atmospheric Environment*, *43*(32), 5128-5131.

Lee, B. H., E. C. Wood, M. S. Zahniser, J. B. McManus, D. D. Nelson, S. C. Herndon, G. W. Santoni, S. C. Wofsy, and J. W. Munger (2011), Simultaneous measurements of atmospheric HONO and NO2 via absorption spectroscopy using tunable mid-infrared continuous-wave quantum cascade lasers, *Applied Physics B-Lasers and Optics*, *102*(2), 417-423.

Lee, B. H., E. C. Wood, M. S. Zahniser, J. Wormhoudt, S. C. Wofsy, and J. W. Munger (2012), Effective line strengths of trans-nitrous acid near 1275 cm-1 and cis-nitrous acid at 1660 cm-1 using cw-QC TILDAS, *Journal of Quantitative Spectroscopy & Radiative Transfer,* submitted.

Li, S. P., J. Matthews, and A. Sinha (2008), Atmospheric hydroxyl radical production from electronically excited NO(2) and H(2)O, *Science*, *319*(5870), 1657-1660.

Luke, W. T., P. Kelley, B. L. Lefer, J. Flynn, B. Rappengluck, M. Leuchner, J. E. Dibb, L. D. Ziemba, C. H. Anderson, and M. Buhr (2010), Measurements of primary trace gases and NO(y) composition in Houston, Texas, *Atmospheric Environment*, *44*(33), 4068-4080.

Mao, J. Q., X. R. Ren, S. A. Chen, W. H. Brune, Z. Chen, M. Martinez, H. Harder, B. Lefer, B. Rappengluck, J. Flynn, and M. Leuchner (2010), Atmospheric oxidation capacity in the summer of Houston 2006: Comparison with summer measurements in other metropolitan studies, *Atmospheric Environment*, *44*(33), 4107-4115.

Monge, M. E., B. D'Anna, and C. George (2010), Nitrogen dioxide removal and nitrous acid formation on titanium oxide surfaces-an air quality remediation process?, *Physical Chemistry Chemical Physics*, *12*(31), 8992-8999.

Neftel, A., A. Blatter, R. Hesterberg, and T. Staffelbach (1996), Measurements of concentration gradients of HNO2 and HNO3 over a semi-natural ecosystem, *Atmospheric Environment*, *30*(17), 3017-3025.

Pitts, J. N., H. W. Biermann, R. Atkinson, and A. M. Winer (1984), Atmospheric Implications of Simultaneous Nighttime Measurements of No3 Radicals and Hono, *Geophysical Research Letters*, *11*(5), 557-560.

Platt, U., D. Perner, G. W. Harris, A. M. Winer, and J. N. Pitts (1980), Observations of Nitrous-Acid in an Urban Atmosphere by Differential Optical-Absorption, *Nature*, *285*(5763), 312-314.

Ren, X. R., H. Harder, M. Martinez, R. L. Lesher, A. Oliger, J. B. Simpas, W. H. Brune, J. J. Schwab, K. L. Demerjian, Y. He, X. L. Zhou, and H. G. Gao (2003), OH and HO2 chemistry in the urban atmosphere of New York City, *Atmospheric Environment*, *37*(26), 3639-3651.

Ren, X. R., W. H. Brune, J. Q. Mao, M. J. Mitchell, R. L. Lesher, J. B. Simpas, A. R. Metcalf, J. J. Schwab, C. X. Cai, Y. Q. Li, K. L. Demerjian, H. D. Felton, G. Boynton, A. Adams, J. Perry, Y. He, X. L. Zhou, and J. Hou (2006), Behavior of OH and HO2 in the winter atmosphere in New York city, *Atmospheric Environment*, *40*, S252-S263.

Sander, S. P., J. Abbatt, J. R. Barker, J. B. Burkholder, R. R. Friedl, D. M. Golden, R. E. Huie, C. E. Kolb, M. J. Kurylo, G. K. Moortgat, V. L. Orkin, and P. H. Wine (2011), Chemical Kinetics and Photochemical Data for Use in Atmospheric Studies, Evaluation No. 17, edited by J. P. Laboratory, JPL Publication 10-6, Pasadena.

Sorgel, M., E. Regelin, H. Bozem, J. M. Diesch, F. Drewnick, H. Fischer, H. Harder, A. Held, Z. Hosaynali-Beygi, M. Martinez, and C. Zetzsch (2011), Quantification of the unknown

HONO daytime source and its relation to NO(2), *Atmospheric Chemistry and Physics*, *11*(20), 10433-10447.

Staffelbach, T., A. Neftel, and L. W. Horowitz (1997), Photochemical oxidant formation over southern Switzerland .2. Model results, *Journal of Geophysical Research-Atmospheres*, *102*(D19), 23363-23373.

Steinfeld, J. I., J. S. Francisco, and W. L. Hase (1989), *Chemical kinetics and dynamics*, xii, 548 p. pp., Prentice Hall, Englewood Cliffs, N.J.

Stemmler, K., M. Ammann, C. Donders, J. Kleffmann, and C. George (2006), Photosensitized reduction of nitrogen dioxide on humic acid as a source of nitrous acid, *Nature*, *440*(7081), 195-198.

Stemmler, K., M. Ndour, Y. Elshorbany, J. Kleffmann, B. D'Anna, C. George, B. Bohn, and M. Ammann (2007), Light induced conversion of nitrogen dioxide into nitrous acid on submicron humic acid aerosol, *Atmospheric Chemistry and Physics*, *7*(16), 4237-4248.

Stutz, J., B. Alicke, and A. Neftel (2002), Nitrous acid formation in the urban atmosphere: Gradient measurements of NO2 and HONO over grass in Milan, Italy, *Journal of Geophysical Research-Atmospheres*, *107*(D22).

Su, H., Y. F. Cheng, M. Shao, D. F. Gao, Z. Y. Yu, L. M. Zeng, J. Slanina, Y. H. Zhang, and A. Wiedensohler (2008), Nitrous acid (HONO) and its daytime sources at a rural site during the 2004 PRIDE-PRD experiment in China, *Journal of Geophysical Research-Atmospheres*, *113*(D14).

Su, H., Y. F. Cheng, R. Oswald, T. Behrendt, I. Trebs, F. X. Meixner, M. O. Andreae, P. Cheng, Y. Zhang, and U. Poschl (2011), Soil Nitrite as a Source of Atmospheric HONO and OH Radicals, *Science*, *333*(6049), 1616-1618.

Turanyi, T., A. S. Tomlin, and M. J. Pilling (1993), On the Error of the Quasi-Steady-State Approximation, *Journal of Physical Chemistry*, *97*(1), 163-172.

Vogel, B., H. Vogel, J. Kleffmann, and R. Kurtenbach (2003), Measured and simulated vertical profiles of nitrous acid - Part II. Model simulations and indications for a photolytic source, *Atmospheric Environment*, *37*(21), 2957-2966.

Wayne, R. P. (2000), *Chemistry of atmospheres : an introduction to the chemistry of the atmospheres of earth, the planets, and their satellites*, 3rd ed., xxix, 775 p. pp., Oxford University Press, Oxford [England] ; New York.

Winer, A. M., and H. W. Biermann (1994), Long Pathlength Differential Optical-Absorption Spectroscopy (Doas) Measurements of Gaseous Hono, No2 and Hcho in the California South Coast Air Basin, *Research on Chemical Intermediates*, *20*(3-5), 423-445.

Wong, K. W., H. J. Oh, B. L. Lefer, B. Rappengluck, and J. Stutz (2011), Vertical profiles of nitrous acid in the nocturnal urban atmosphere of Houston, TX, *Atmospheric Chemistry and Physics*, *11*(8), 3595-3609.

Wong, K. W., C. Tsai, B. Lefer, C. Haman, N. Grossberg, W. H. Brune, X. Ren, W. Luke, and J. Stutz (2012), Daytime HONO vertical gradients during SHARP 2009 in Houston, TX, *Atmospheric Chemistry and Physics*, *12*, 635-652.

Yu, Y., B. Galle, A. Panday, E. Hodson, R. Prinn, and S. Wang (2009), Observations of high rates of NO2-HONO conversion in the nocturnal atmospheric boundary layer in Kathmandu, Nepal, *Atmospheric Chemistry and Physics*, *9*(17), 6401-6415.

Zhou, X. L., N. Zhang, M. TerAvest, D. Tang, J. Hou, S. Bertman, M. Alaghmand, P. B. Shepson, M. A. Carroll, S. Griffith, S. Dusanter, and P. S. Stevens (2011), Nitric acid photolysis on forest canopy surface as a source for tropospheric nitrous acid, *Nature Geoscience*, *4*(7), 440-443.

Ziemba, L. D., J. E. Dibb, R. J. Griffin, C. H. Anderson, S. I. Whitlow, B. L. Lefer, B. Rappengluck, and J. Flynn (2010), Heterogeneous conversion of nitric acid to nitrous acid on the surface of primary organic aerosol in an urban atmosphere, *Atmospheric Environment*, *44*(33), 4081-4089.

Chapter 7:

Absence of daytime/non-surface-NO_2-driven nighttime HONO production observed above a forest

Abstract

Daytime production of HONO in relatively pristine areas is reported to be a significant, yet-unconstrained source of hydroxyl radicals, one of the main atmospheric oxidants, near the Earth's surface. Nearly-continuous, year-long measurements by direct absorption spectroscopy a few meters above the canopy at Harvard Forest, however, show no evidence of sunlight-driven HONO production. The median daytime (10 am to 4 pm, local time) HONO mixing ratio spanning the four seasons is 15 ppt (n=1004, 1-hr avg.), comparable to levels expected given known chemistry. Biosphere-atmosphere exchange of HONO is at all times below instrument eddy covariance flux detection limit (1-hr 3-σ) of about 0.9×10^{-6} mol m^{-2} h^{-1} (550 ppt cm sec^{-1}). Observations indicate secondary daytime HONO production contributes negligibly to the HO_x and NO_x budgets of the overlying atmosphere at Harvard Forest over all seasons. Enhanced nighttime HONO level is observed, with high night-to-night variability exhibited in HONO:NO_2 that cannot be reasonably explained by NO_2 and HONO fluxes. We propose non-NO_2, non-ground/canopy surface related nighttime source.

7.1. Introduction

Recent measurements above forest canopies show daytime HONO mixing ratios elevated above levels calculated assuming photostationary state. Such observations have been interpreted

as evidence of an unaccounted secondary HONO source [*Acker et al*., 2006b; *Kleffmann et al*., 2005; *Ren et al*., 2010a; *Sorgel et al*., 2011; *Zhou et al*., 2007b; *Zhou et al*., 2011]. Numerous sunlight-driven production pathways have been proposed to balance the observed HONO loss rate due to photolysis and OH-oxidation that often exceed the rate of production by the gas-phase reaction between NO and OH [*Stemmler et al*., 2006; *Su et al*., 2011; *Zhou et al*., 2011]. The rate of secondary HONO formation inferred from this photostationary state approximation suggests a significant source of OH radical, as HONO photodissociates with a midday lifetime of around ten minutes during the summer season. Moreover, depending on the mechanism, it may represent a pathway by which deposited nitrogen oxides are repartitioned back into the atmosphere in reactive form [*Zhou et al*., 2003; *Zhou et al*., 2007a].

Accumulation of HONO beneath the nocturnal boundary layer initiates photochemistry in the early morning prior to other HO_x precursors [*Platt et al*., 1980; *Winer and Biermann*, 1994]. Previous studies have attributed nighttime HONO growth to the heterogeneous reaction of NO_2 on humid surfaces [*Barney and Finlayson-Pitts*, 2000; *Finlayson-Pitts et al*., 2003; *Pitts et al*., 1984; *Ramazan et al*., 2006], even in urban areas where this reaction is thought to dominate over direct combustion emissions [*Platt et al*., 1980; *Stutz et al*., 2002]. In the laboratory, the rate of this reaction is first order with respect to the level of NO_2, yielding 1 HONO molecule for every 2 NO_2 deposited. Over a grassy field in an urban environment, *Stutz et al*. [*Platt et al*., 1980; *Stutz et al*., 2002] observed 1 HONO emitted from the ground surface for every 33 NO_2 deposited.

Here we present near-continuous measurements of atmospheric HONO and NO_2 observed above the forest canopy at the Environmental Measurement Site at Harvard Forest from December 2010 to December 2011 (supplemental figure B7). This represents the first extended

campaign simultaneously measuring HONO and NO_2 – a proposed day and nighttime HONO precursor – mixing ratios as well as fluxes by eddy covariance using an absorption spectrometer. Though not as sensitive as the wet-chemical extraction technique [*Dibb et al*., 2004; *Huang et al*., 2002; *Kleffmann et al*., 2002], which to-date have been the only instruments deployed in forested environments, the direct spectroscopic method offers greater specificity as it is less prone to artifacts and interferences [*Kleffmann et al*., 2006; *Liao et al*., 2006] (Supplementary figure B8).

7.2. Methods

Ambient air was continuously drawn through an inlet located about 5 m above the canopy on a 30 m tall tower at the mixed deciduous (~30% red oak by basal area) Harvard Forest. The custom-designed inlet inertially separated large (>4 μm) particles, obviating the need for a filter. The inlet also reduced by about half the pressure of the sample, which subsequently traveled through 180 feet of perfluoroalkoxy tubing (0.375 inch outer diameter) to the ground-based spectrometer. The inlet and tubing were heated to above ambient and shielded from light to minimize the presence of surface water and photochemical reactions. A total flow rate of about 12 standard liters per minute was maintained, resulting in sample residence times (1/e) of about 0.3, 1.6 and 1.3 seconds in the inlet, tubing and sampling cell, respectively. Routine in-field additions of gaseous HONO and NO_2 into the inlet showed equal response times through the inlet, tubing and instrument, exhibiting the absence of slow, reversible loss of HONO through the sampling setup. Additions of gaseous HONO with/without the inlet and with/without the tubing showed no instantaneous loss on the surfaces of either apparatus (Supplementary figure B9). Additions of high levels of NO_2 under conditions conducive to heterogeneous HONO

production (*i.e*. unheated tubing/inlet, sample near ambient pressure) mixed with humid urban air, dry room air and humidity-matched zero-air showed no enhancement of HONO due either to chemical or spectroscopic interference (Supplementary figure B10). These tests demonstrate the absence of positive and negative artifacts from the sampling scheme used.

Calibrations were periodically performed by catalytic conversion of generated HONO to nitric oxide, which was measured by a second co-located instrument [*Munger et al*., 1996]. Supplemented by continuously monitoring the laser stability – the main source of drift with spectroscopic techniques – we confirm the absence of long-term drift in measurements. Short-term variability, driven by thermal perturbations to the instrument, were corrected by frequent spectral background subtractions with additions of zero-air – generated by scrubbing ambient air by heated palladium catalyst – every 180 seconds for 45 seconds. We report detection limits (3σ 1-hr) of 15 and 5 ppt for HONO and NO_2, respectively (Supplementary figure B11). Additional details regarding the instrument performance and sampling scheme are provided elsewhere [*Lee et al*., 2011]. Eddy covariance flux detection limits (3σ 1-hr) for HONO and NO_2 were about 0.9×10^{-6} mol m^{-2} h^{-1} (550 ppt cm sec^{-1}) and 5×10^{-6} mol m^{-2} h^{-1} (2.9 ppb cm sec^{-1}), respectively, determined as the 3σ of the mean of the covariance from -1000 to -500 and +500 to +1000 seconds away from true lag (Supplementary figure B12) [*McKinney et al*., 2011].

7.3. Results and discussion

Figure 1 shows a brief time series exhibiting a typical diurnal trend of HONO and NO_2 mixing ratios at Harvard Forest. Nighttime enhancement of HONO is observed, concomitant with NO_2. The levels of both decrease with the breakup of the nocturnal boundary layer and photolytic loss at sunrise. Figure 2 shows the diurnally averaged HONO mixing ratios

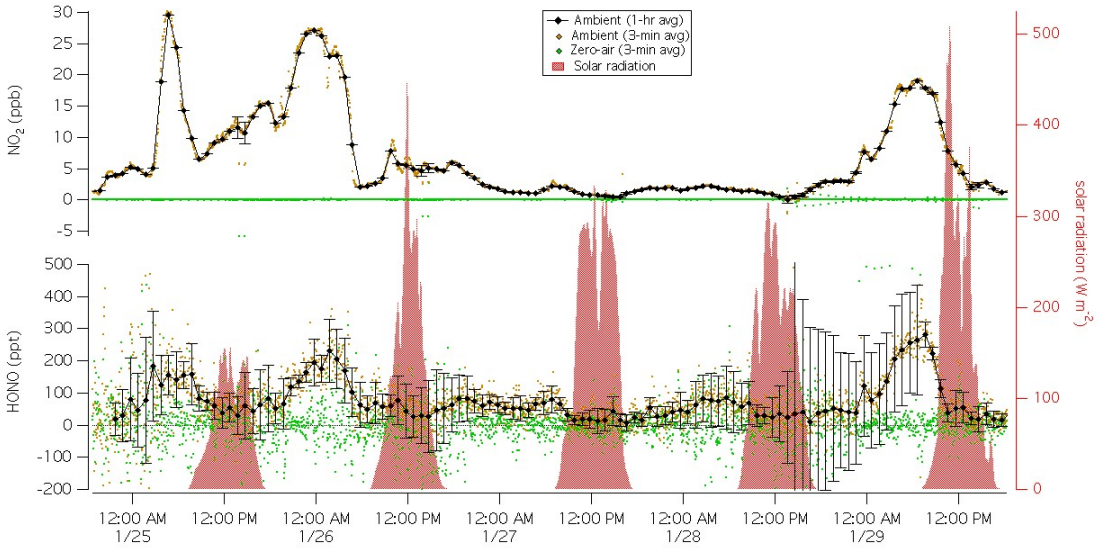

Figure 7.1 Time series of NO_2 (top) and HONO (bottom), with total solar radiation (right).

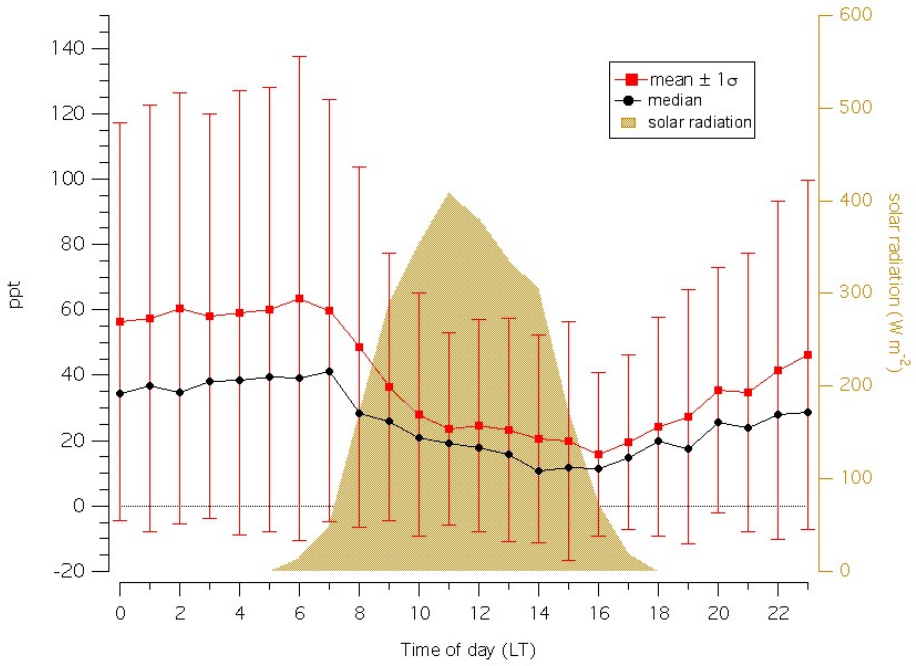

Figure 7.2. Diurnal mean and median of HONO mixing ratio (left) and total solar radiation (right) for December 2010 to December 2011.

encompassing all seasons. The median daytime (10 am to 4 pm) HONO mixing ratio is 15 ppt, much lower than has been previously measured in other rural, forested atmospheres [*Acker et al*., 2006a; *He et al*., 2006; *Kleffmann et al*., 2005; *Sorgel et al*., 2011; *Zhou et al*., 2011]. Previous studies have compared measured values to those inferred assuming that HONO is at photostationary state, that is, that the production rate by the homogeneous reaction between NO and OH (R1) is exactly balanced by the sum of the loss rates by photolysis (R2) and OH-oxidation (R3).

R1 $NO + OH + M \rightarrow HONO + M$

R2 $HONO + h\nu \rightarrow OH + NO$

R3 $HONO + OH \rightarrow H_2O + NO_2$

At photostationary state, the HONO mixing ratio is then given by,

$$[HONO]_{PSS} = \frac{k_1[NO][OH]}{J_2 + k_3[OH]}$$

Given typical rural daytime values of NO, OH and HONO photolysis rate, photostationary state yields HONO mixing ratio around 10 to 20 ppt. Comparable to our observations, *Ren et al*. [2010b] observed daytime HONO levels between 20 and 30 ppt at Blodgett Forest at the foothills of the Sierra Nevada Mountains. *Ren et al*. [2010b], nonetheless, report a secondary daytime HONO source as their measured values were on average a factor of 9 greater that those calculated at PSS. We contend, however, that the PSS-approximated level does not establish a reliable baseline to infer a secondary source. It has been demonstrated that in

order for steady state to be established, a length of time since emission/production several times greater than the lifetime of the reactive species is required [*Steinfeld et al*., 1989; *Turanyi et al*., 1993]. If rapid HONO production is occurring on the surface of canopy leaves [*Zhou et al*., 2011], sampling a few m from the source suggests complete photostationary state is likely not achieved. If production is occurring below the shaded canopy [*Stemmler et al*., 2006; *Su et al*., 2011] where the HONO lifetime is on the order of several tens of minutes, an even longer period of reaction/transport time since production is required for photostationary state to be established.

Assuming that there is daytime HONO flux out of the canopy at a rate of our 3σ flux detection limit (550 ppt cm sec^{-1}) into a well-mixed daytime boundary layer height of 500 m, this would result in an enhancement of 36 ppt of HONO. The resulting rate of OH production due to HONO photolysis would be negligible compared to that from typically observed O_3 levels.

Daytime HONO production rate ranging from 160 to 2600 ppt hr^{-1} has been reported in rural and suburban sites in the U.S. and Europe [*Acker et al*., 2006b; *Acker and Moller*, 2007; *Kleffmann et al*., 2005; *Ren et al*., 2010a; *Zhou et al*., 2011]. Integrated throughout a daytime boundary layer height of 500 m, this range is equivalent to a vertical flux between 2,222 ppt and 36,111 ppt cm sec^{-1}, well within our detection limit.

The contrasting observations are difficult to reconcile. Site-specific chemistry is possible, but unlikely seeing as Harvard Forest experienced comparable, if not higher, levels of NO_2 – the hypothesized HONO precursor – than at sites where measurements indicate strong daytime production. Acidity, nitrite and nitrate ion and humic acid content in soils or leaf surface may differ. Instrumental sensitivity to artifacts cannot be ruled out. At the very least, previous claims of fast HONO production should not be extrapolated to all rural environments.

Figure 3 shows a brief time series of HONO and NO_2 mixing ratios, flux of NO_2 and total solar radiation. Note, that the level of nighttime HONO level enhancement is approximately the same on both nights, whereas NO_2 on the second night is about half that of the first. Deposition of NO_2 is far greater on the first night than on the second, consistent with NO_2 but not HONO. Moreover, let us assume that 2 NO_2 molecules depositing on the canopy/ground surface yields 1 HONO molecule, and that the reaction and release of surface-adsorbed HONO into the canopy space is instantaneous. The grey trace on figure 5 shows the flux of NO_2 required in a 100 m deep nocturnal boundary layer to maintain the observed HONO mixing ratio. While there is sufficient NO_2 deposited on the first night, this is not the case on the second night. Similarly, HONO flux out of the canopy at a rate of our 3σ flux detection limit into a nocturnal boundary layer height of 100 m, would result in a HONO enhancement of 180 ppt, less than what is observed. This indicates that the flux should be greater, but is not observed. Nighttime observations at Harvard Forest strongly suggest a nighttime HONO source independent of gas-phase NO_2 and unrelated to the below canopy/ground surface.

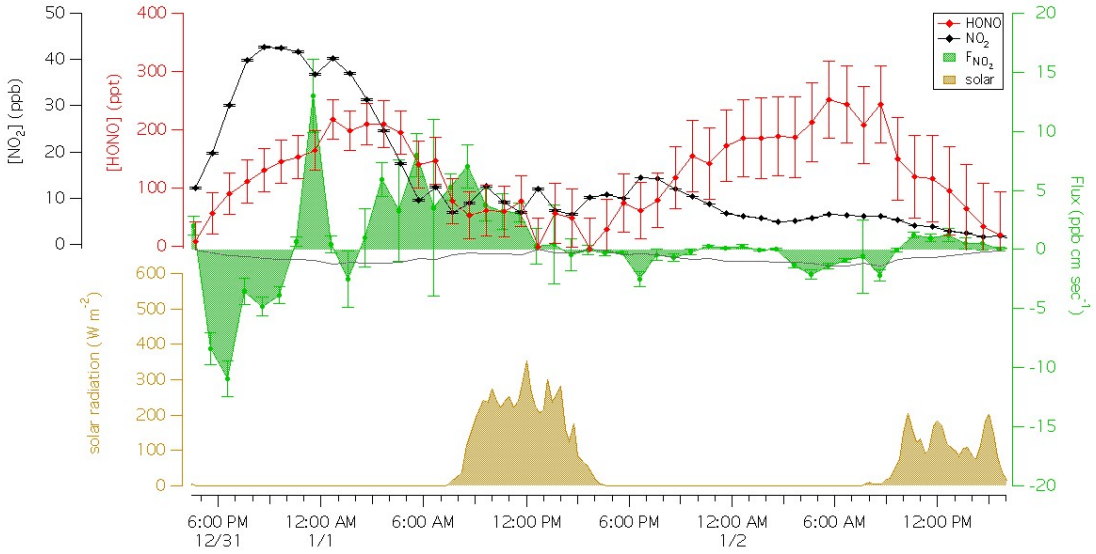

Figure 7.3. Time series of HONO (red) and NO_2 (black) mixing ratio, observed flux of NO_2 (green), calculated flux of NO_2 needed to account for observed nighttime HONO enhancement (grey) and total solar radiation (beige).

References

Acker, K., A. Febo, S. Trick, C. Perrino, P. Bruno, P. Wiesen, D. Moller, W. Wieprecht, R. Auel, M. Giusto, A. Geyer, U. Platt, and I. Allegrini (2006a), Nitrous acid in the urban area of Rome, *Atmospheric Environment*, *40*(17), 3123-3133.

Acker, K., D. Moller, W. Wieprecht, F. X. Meixner, B. Bohn, S. Gilge, C. Plass-Dulmer, and H. Berresheim (2006b), Strong daytime production of OH from HNO2 at a rural mountain site, *Geophysical Research Letters*, *33*(2), -.

Acker, K., and D. Moller (2007), Atmospheric variation of nitrous acid at different sites in Europe, *Environmental Chemistry*, *4*(4), 242-255.

Barney, W. S., and B. J. Finlayson-Pitts (2000), Enhancement of N2O4 on porous glass at room temperature: A key intermediate in the heterogeneous hydrolysis of NO2?, *Journal of Physical Chemistry A*, *104*(2), 171-175.

Dibb, J. E., L. G. Huey, D. L. Slusher, and D. J. Tanner (2004), Soluble reactive nitrogen oxides at South Pole during ISCAT 2000, *Atmospheric Environment*, *38*(32), 5399-5409.

Finlayson-Pitts, B. J., L. M. Wingen, A. L. Sumner, D. Syomin, and K. A. Ramazan (2003), The heterogeneous hydrolysis of NO2 in laboratory systems and in outdoor and indoor atmospheres: An integrated mechanism, *Physical Chemistry Chemical Physics*, *5*(2), 223-242.

He, Y., X. L. Zhou, J. Hou, H. L. Gao, and S. B. Bertman (2006), Importance of dew in controlling the air-surface exchange of HONO in rural forested environments, *Geophysical Research Letters*, *33*(2), -.

Huang, G., X. L. Zhou, G. H. Deng, H. C. Qiao, and K. Civerolo (2002), Measurements of atmospheric nitrous acid and nitric acid, *Atmospheric Environment*, *36*(13), 2225-2235.

Kleffmann, J., J. Heland, R. Kurtenbach, J. Lorzer, and P. Wiesen (2002), A new instrument (LOPAP) for the detection of nitrous acid (HONO), *Environmental Science and Pollution Research*, 48-54.

Kleffmann, J., T. Gavriloaiei, A. Hofzumahaus, F. Holland, R. Koppmann, L. Rupp, E. Schlosser, M. Siese, and A. Wahner (2005), Daytime formation of nitrous acid: A major source of OH radicals in a forest, *Geophysical Research Letters*, *32*(5).

Kleffmann, J., J. C. Lorzer, P. Wiesen, C. Kern, S. Trick, R. Volkamer, M. Rodenas, and K. Wirtz (2006), Intercomparison of the DOAS and LOPAP techniques for the detection of nitrous acid (HONO), *Atmospheric Environment*, *40*(20), 3640-3652.

Lee, B. H., E. C. Wood, M. S. Zahniser, J. B. McManus, D. D. Nelson, S. C. Herndon, G. W. Santoni, S. C. Wofsy, and J. W. Munger (2011), Simultaneous measurements of

atmospheric HONO and NO2 via absorption spectroscopy using tunable mid-infrared continuous-wave quantum cascade lasers, *Applied Physics B-Lasers and Optics*, *102*(2), 417-423.

Liao, W., A. T. Case, J. Mastromarino, D. Tan, and J. E. Dibb (2006), Observations of HONO by laser-induced fluorescence at the South Pole during ANTCI 2003, *Geophysical Research Letters*, *33*(9), -.

McKinney, K. A., B. H. Lee, A. Vasta, T. V. Pho, and J. W. Munger (2011), Emissions of isoprenoids and oxygenated biogenic volatile organic compounds from a New England mixed forest, *Atmospheric Chemistry and Physics*, *11*(10), 4807-4831.

Munger, J. W., S. C. Wofsy, P. S. Bakwin, S. M. Fan, M. L. Goulden, B. C. Daube, A. H. Goldstein, K. E. Moore, and D. R. Fitzjarrald (1996), Atmospheric deposition of reactive nitrogen oxides and ozone in a temperate deciduous forest and a subarctic woodland .1. Measurements and mechanisms, *Journal of Geophysical Research-Atmospheres*, *101*(D7), 12639-12657.

Pitts, J. N., E. Sanhueza, R. Atkinson, W. P. L. Carter, A. M. Winer, G. W. Harris, and C. N. Plum (1984), An Investigation of the Dark Formation of Nitrous-Acid in Environmental Chambers, *International Journal of Chemical Kinetics*, *16*(7), 919-939.

Platt, U., D. Perner, G. W. Harris, A. M. Winer, and J. N. Pitts (1980), Observations of Nitrous-Acid in an Urban Atmosphere by Differential Optical-Absorption, *Nature*, *285*(5763), 312-314.

Ramazan, K. A., L. M. Wingen, Y. Miller, G. M. Chaban, R. B. Gerber, S. S. Xantheas, and B. J. Finlayson-Pitts (2006), New experimental and theoretical approach to the heterogeneous hydrolysis of NO2: Key role of molecular nitric acid and its complexes, *Journal of Physical Chemistry A*, *110*(21), 6886-6897.

Ren, X., H. Gao, X. Zhou, J. D. Crounse, P. O. Wennberg, E. C. Browne, B. W. LaFranchi, R. C. Cohen, M. Mckay, A. H. Goldstein, and J. Mao (2010a), Measurement of atmospheric nitrous acid at Blodgett Forest during BEARPEX2007, *Atmospheric Chemistry and Physics*, *10*(13), 6283-6294.

Ren, X., H. Gao, X. Zhou, J. D. Crounse, P. O. Wennberg, E. C. Browne, B. W. LaFranchi, R. C. Cohen, M. McKay, A. H. Goldstein, and J. Mao (2010b), Measurement of atmospheric nitrous acid at Blodgett Forest during BEARPEX2007 (vol 10, pg 6283, 2010), *Atmospheric Chemistry and Physics*, *10*(14), 6501-6501.

Sorgel, M., I. Trebs, A. Serafimovich, A. Moravek, A. Held, and C. Zetzsch (2011), Simultaneous HONO measurements in and above a forest canopy: influence of turbulent exchange on mixing ratio differences, *Atmospheric Chemistry and Physics*, *11*(2), 841-855.

Steinfeld, J. I., J. S. Francisco, and W. L. Hase (1989), *Chemical kinetics and dynamics*, xii, 548 p. pp., Prentice Hall, Englewood Cliffs, N.J.

Stemmler, K., M. Ammann, C. Donders, J. Kleffmann, and C. George (2006), Photosensitized reduction of nitrogen dioxide on humic acid as a source of nitrous acid, *Nature*, *440*(7081), 195-198.

Stutz, J., B. Alicke, and A. Neftel (2002), Nitrous acid formation in the urban atmosphere: Gradient measurements of NO2 and HONO over grass in Milan, Italy, *Journal of Geophysical Research-Atmospheres*, *107*(D22).

Su, H., Y. F. Cheng, R. Oswald, T. Behrendt, I. Trebs, F. X. Meixner, M. O. Andreae, P. Cheng, Y. Zhang, and U. Poschl (2011), Soil Nitrite as a Source of Atmospheric HONO and OH Radicals, *Science*, *333*(6049), 1616-1618.

Turanyi, T., A. S. Tomlin, and M. J. Pilling (1993), On the Error of the Quasi-Steady-State Approximation, *Journal of Physical Chemistry*, *97*(1), 163-172.

Winer, A. M., and H. W. Biermann (1994), Long Pathlength Differential Optical-Absorption Spectroscopy (Doas) Measurements of Gaseous Hono, No2 and Hcho in the California South Coast Air Basin, *Research on Chemical Intermediates*, *20*(3-5), 423-445.

Zhou, X. L., H. L. Gao, Y. He, G. Huang, S. B. Bertman, K. Civerolo, and J. Schwab (2003), Nitric acid photolysis on surfaces in low-NOx environments: Significant atmospheric implications, *Geophysical Research Letters*, *30*(23).

Zhou, X. L., H. L. Gao, and Y. He (2007a), Evidence of nitric acid photolysis on surfaces as a Re-NOx-ification pathway, *Abstracts of Papers of the American Chemical Society*, *233*, 431-431.

Zhou, X. L., G. Huang, K. Civerolo, U. Roychowdhury, and K. L. Demerjian (2007b), Summertime observations of HONO, HCHO, and O-3 at the summit of Whiteface Mountain, New York, *Journal of Geophysical Research-Atmospheres*, *112*(D8), -.

Zhou, X. L., N. Zhang, M. TerAvest, D. Tang, J. Hou, S. Bertman, M. Alaghmand, P. B. Shepson, M. A. Carroll, S. Griffith, S. Dusanter, and P. S. Stevens (2011), Nitric acid photolysis on forest canopy surface as a source for tropospheric nitrous acid, *Nature Geoscience*, *4*(7), 440-443.

Chapter 8:

Conclusions

1) **Field experiments:**

The instrument performed well at three different field deployments. It was first taken to the Alternative Aviation Fuel Experiment (January 2009 in Palmdale, CA) where it measured emission indices of HONO, N_2O, CH_4 and H_2O_2 in aircraft exhaust. It was next deployed at the Study of Houston Atmospheric Radical Precursor campaign (May 2009 in Houston, TX) to measure HONO and NO_2 mixing ratios. Finally, HONO and NO_2 mixing ratios and eddy covariance fluxes were measured above the forest canopy at the Environmental Measurement Site at Harvard Forest from December 2010 to December 2011.

2) **Instrument performance:**

The dual cw-QC laser absorption spectrometer achieved mixing ratio detection limits (3σ 1-hr) of 15 and 5 ppt, respectively, for HONO and NO_2. For eddy covariance fluxes, the detection limits (3σ 1-hr) for HONO and NO_2 were 0.9×10^{-6} mol m^{-2} h^{-1} (550 ppt cm sec^{-1}) and 5×10^{-6} mol m^{-2} h^{-1} (2.9 ppb cm sec^{-1}), respectively.

3) **Sampling system:**

We modified an inlet design initially built to measure hydrophilic, photo-sensitive species such as nitric acid and formaldehyde. It inertially separates out large particles, allowing continuous ambient sampling at high flow-rates without the need for filters. Routine in-field

tests under humid, polluted conditions as well as in relatively pristine rural air demonstrate the absence of positive and negative artifacts due to our sampling system.

4) Line strength quantification:

Absorption line strengths – required to quantify gaseous species by spectroscopy – for HONO are not accurately represented in any comprehensive linelist, such as HITRAN. We determined in laboratory experiments the absorption line strengths for HONO in the 6 and 8 micron spectral regions. In situ ambient measurements during the SHARP campaign showed overall agreement to within 6% between four independent instruments.

5) Aircraft exhaust:

We report emissions indices (g per kg of fuel consumed) of HONO, NO_x and H_2O_2 as a function of engine power. While the EI of NO_x increases continuously with engine power – presumably due to combustion temperature – that of HONO levels off at around 60% rated engine thrust, due likely to the exponential increase in HONO+OH reaction rate between 800 and 1000 K. We detect H_2O_2 in aircraft exhaust at low idle thrust only. Production of H_2O_2 is due likely to the HO_2 self-reaction and not the OH self-reaction.

6) Urban air:

Numerous studies claim significant, yet-unaccounted daytime HONO production rates assuming sampled air masses are at photostationary state. Using a simple chemical box model, we show given conservatively-estimated transport times from nearby emission

sources that PSS is likely not achieved, leading to an overestimate of the missing HONO source.

7) **Biosphere-atmosphere exchange:**

Large, unknown daytime HONO sources have also been reported in rural, forested environments. Direct measurements by absorption spectroscopy – as opposed to wet-chemical extraction followed by derivatization – show much lower daytime levels. Additionally, HONO fluxes are lower than instrument detection limit at all times. We conclude no significant daytime HONO production. At night, we propose a non-NO_2, non-ground/canopy-surface source of HONO.

Future research

a) **Is there a reliable near-field tracer for the photochemical age of air masses?**

For short-lived species such as HONO, with a midday photochemical lifetime on the order of several minutes, the limiting factor in being able to model/calculate its atmospheric mixing ratio is the photochemical age, which is required to determine whether observed enhancements are due to direct emission or secondary production. The photostationarity assumption is not valid in the near-field. Proxy such as NO_z:NO_y is not quantitative, due mainly to the uncertainty associated with the levels of NO_z and NO_y in the background atmosphere. Ratios of hydrocarbons, likewise, are not useful as emission sources are not co-located with those of nitrogen oxides.

b) If the cause of the discrepancy in daytime HONO measurements in rural atmospheres is instrument artifact associated with the wet-chemistry method, is there valuable information to be gleaned?

Measurements based on wet-chemical extraction indicate higher HONO levels in similar environments than has been measured by us at Harvard Forest with the more direct, specific technique. Those previous measurements clearly show a diurnal signal. What do those signals indicate? To what else are these instruments sensitive?

c) What is the reaction responsible for nighttime HONO formation?

We observe nighttime enhancement of HONO at Harvard Forest. We rule out direct involvement of gas-phase NO_2 on the ground/canopy surface as the dominant source. This suggests a dispersed source in the ambient air.

Appendix

Supplementary figures

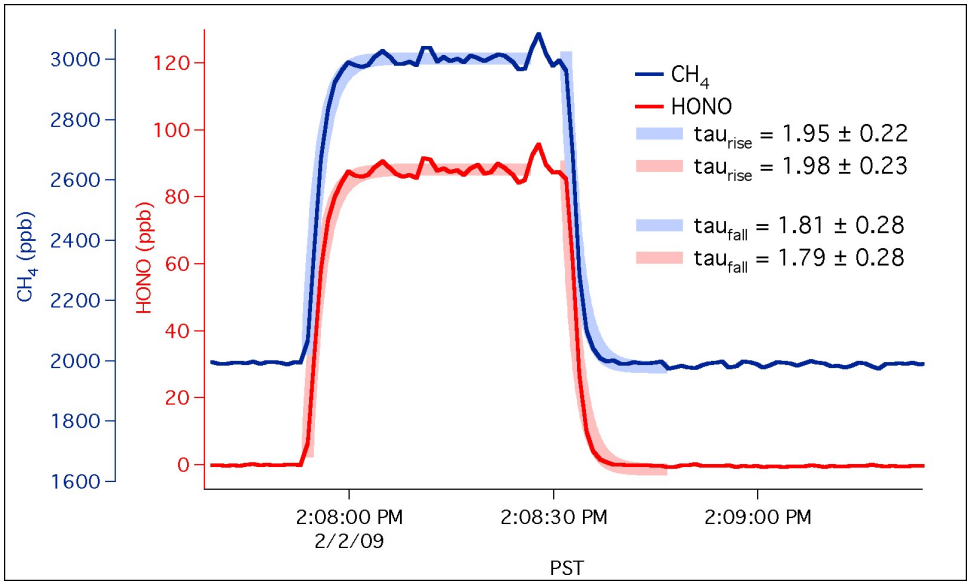

Figure B1. Mixing ratios time series observed during a typical injection of source gas with enhanced levels of CH_4 and HONO. Time response (1/e) – determined by an exponential fit of the increase and decrease of the mixing ratios versus time – are averages of six injection tests.

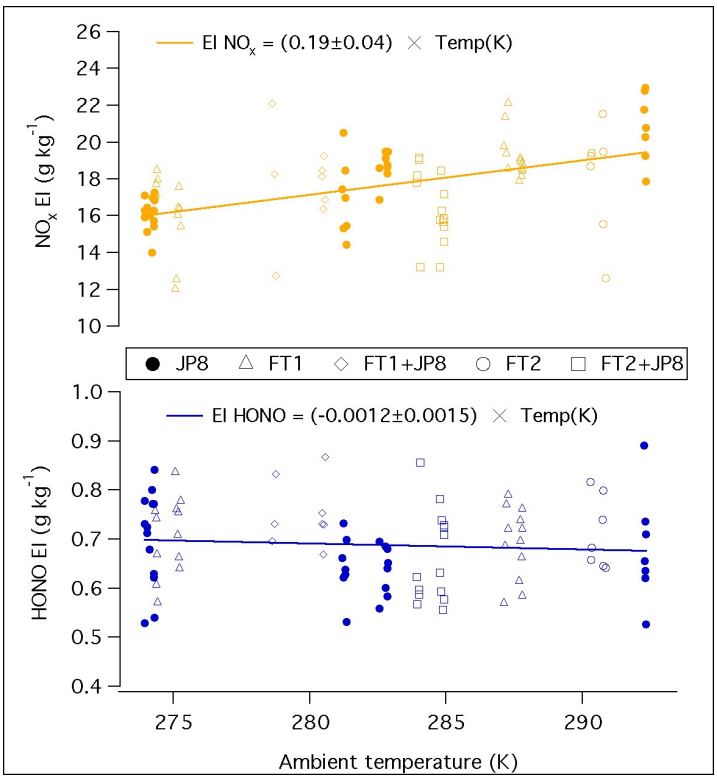

Figure B2. Emission indices of NO_x (a) and HONO (b) observed at maximum rated engine thrust parsed by fuel-type (symbols shown in legend), plotted against ambient temperature.

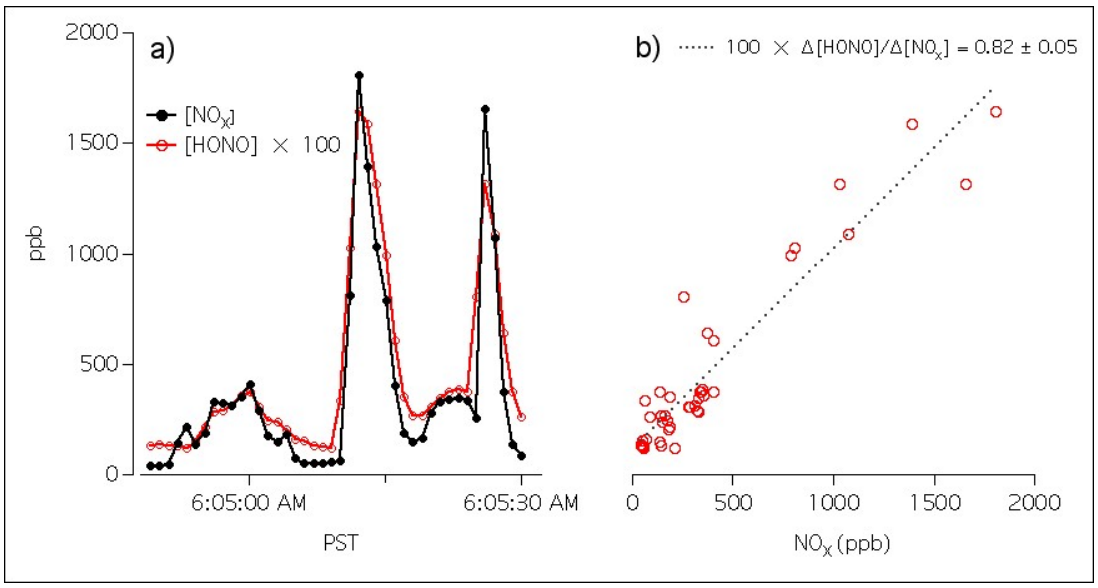

Figure B3. Time-series a) of HONO and NO_x mixing ratios measured from a diesel-powered generator during AAFEX. Scatter plot b) between HONO and NO_x shows an emission ratio of 0.82 ± 0.05%.

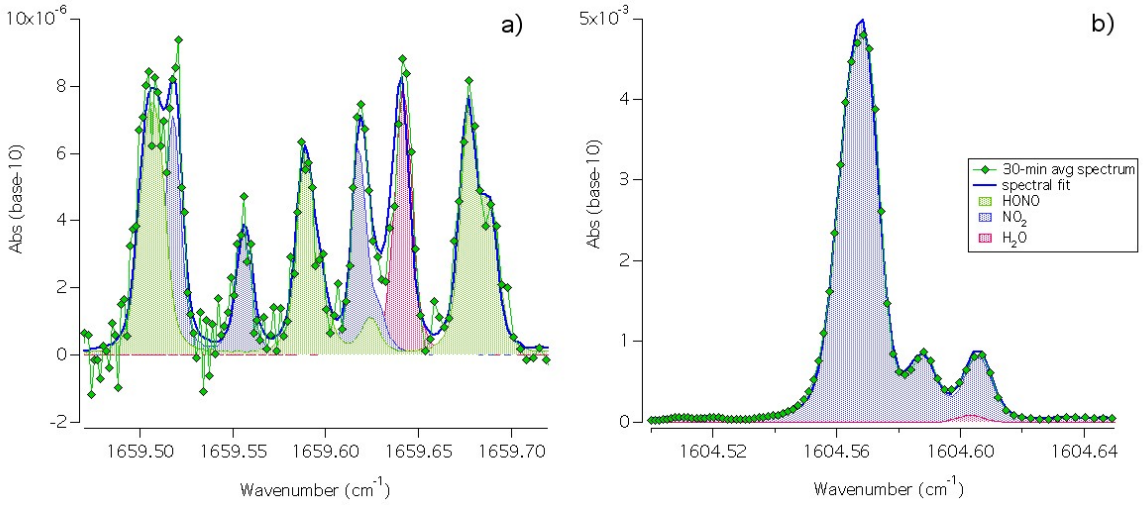

Figure B4. Half-hour averaged absorbance spectra of (a) HONO and (b) NO_2.

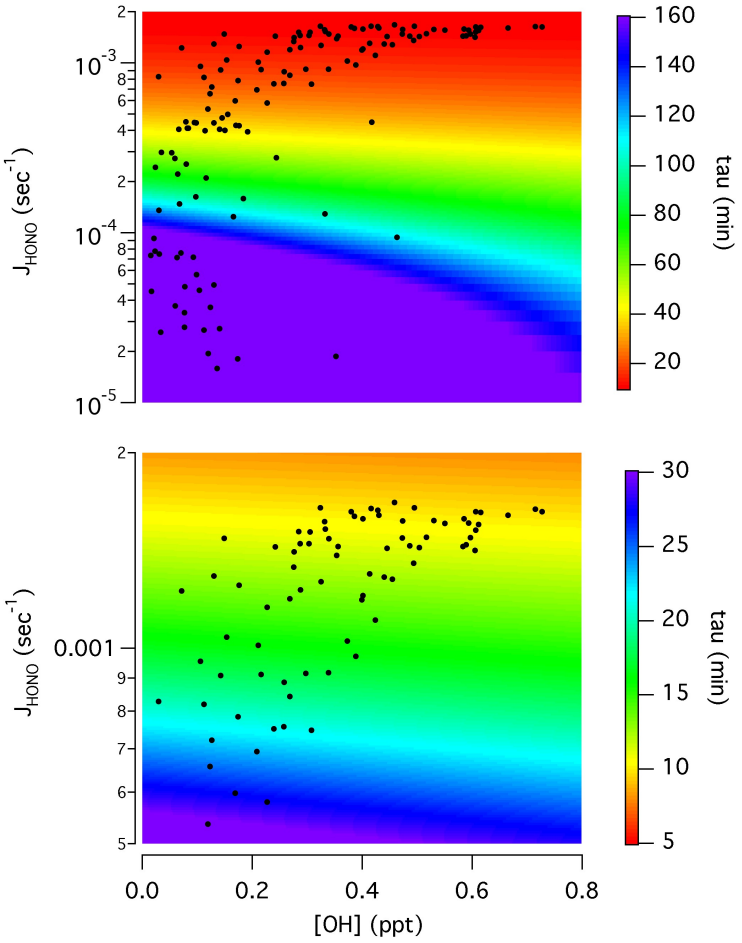

Figure B5. Atmospheric lifetime of HONO (color contour) and observed J_{HONO} versus OH (black markers). Top panel shows τ_{HONO} (E3) for the entire range of J_{HONO} and OH encountered during SHARP, while the bottom panel is a close-up of daytime conditions.

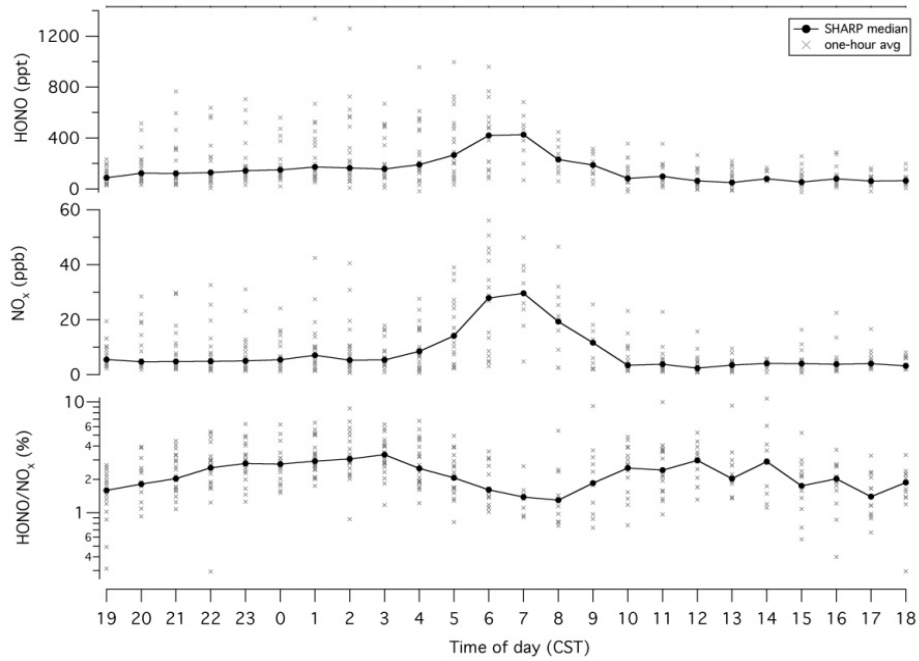

Figure B6. Hourly-averaged and SHARP campaign median of HONO, NO_x and HONO:NO_x plotted from 19:00.

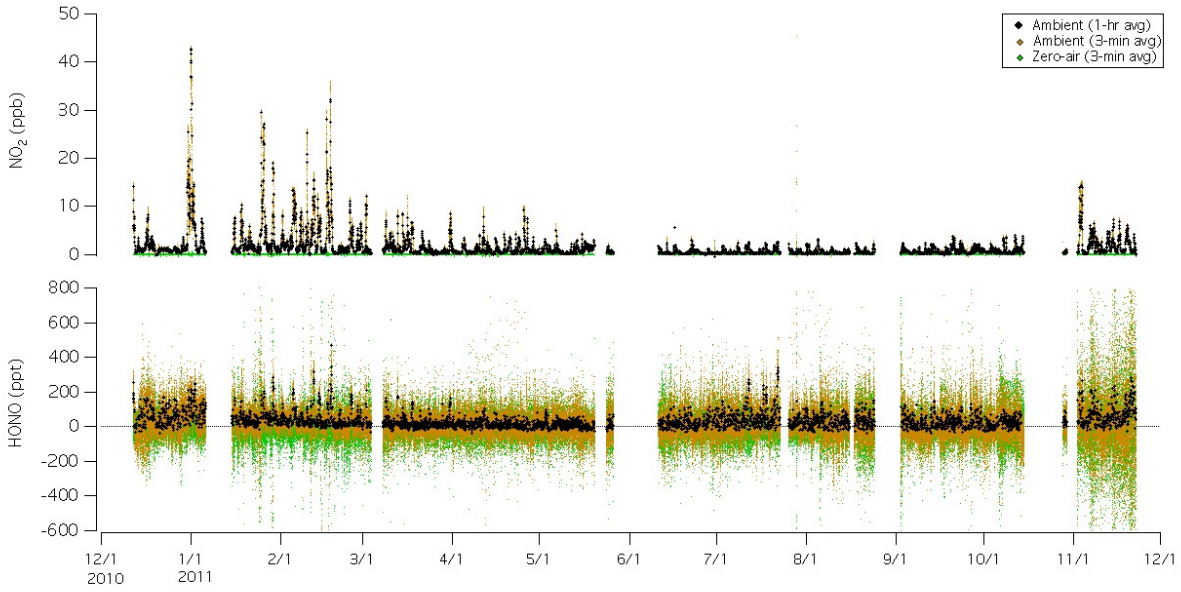

Figure B7. Complete times series of 1-hr averaged HONO and NO_2 mixing ratios measured by the dual-laser absorption spectrometer at Harvard Forest from December 2010 to December 2011. Gaps in the data are due to power flickers, instrument failures and routine maintenance.

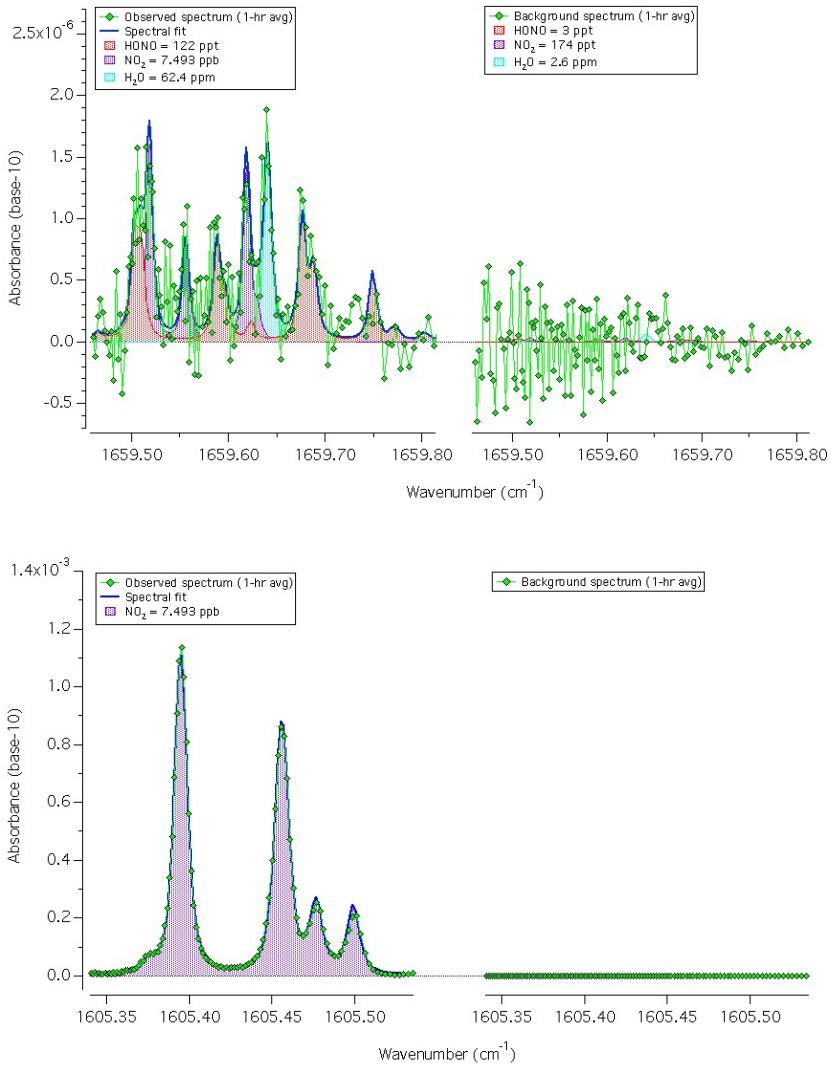

Figure B8. Side by side spectra (1-hr averaged) of ambient and background HONO (top) and NO_2 (bottom).

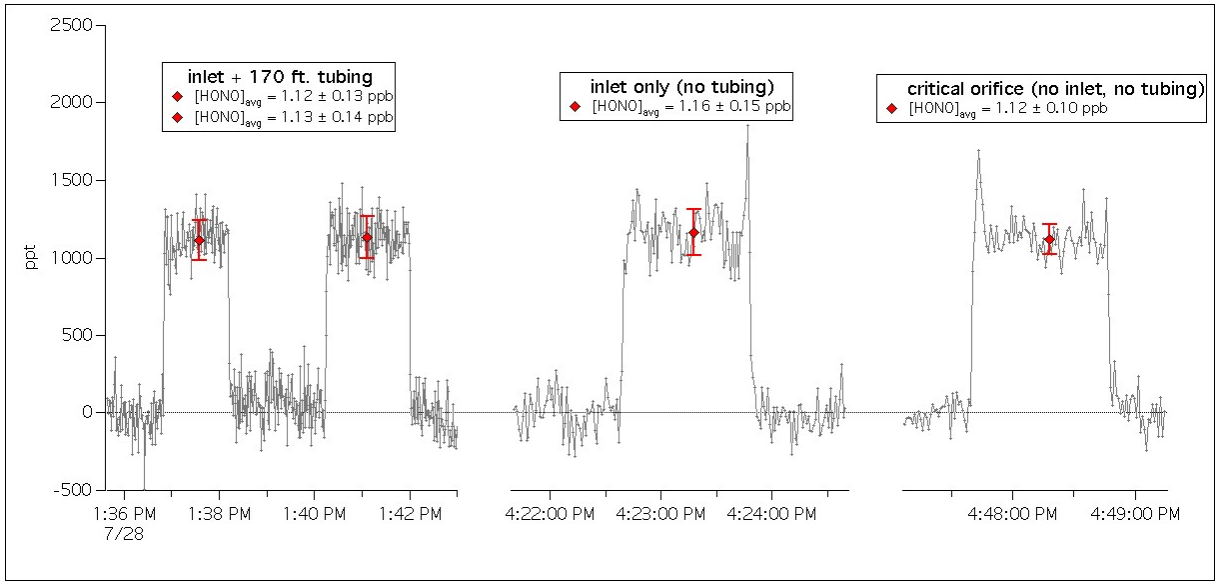

Figure B9. Additions of HONO with full setup (left), without the 180 feet of tubing (middle) and without inlet or tubing (right).

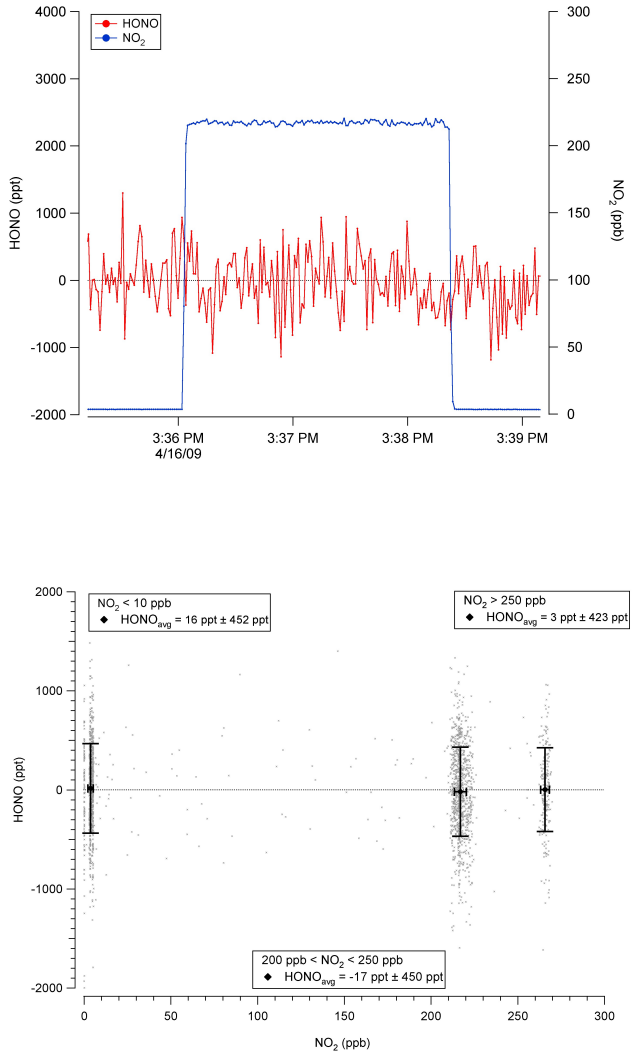

Figure B10. Scatter plot of HONO during additions of NO_2 on top of dry room air, humid Houston air and humidity-matched zero-air, demonstrating the absence of HONO enhancement.

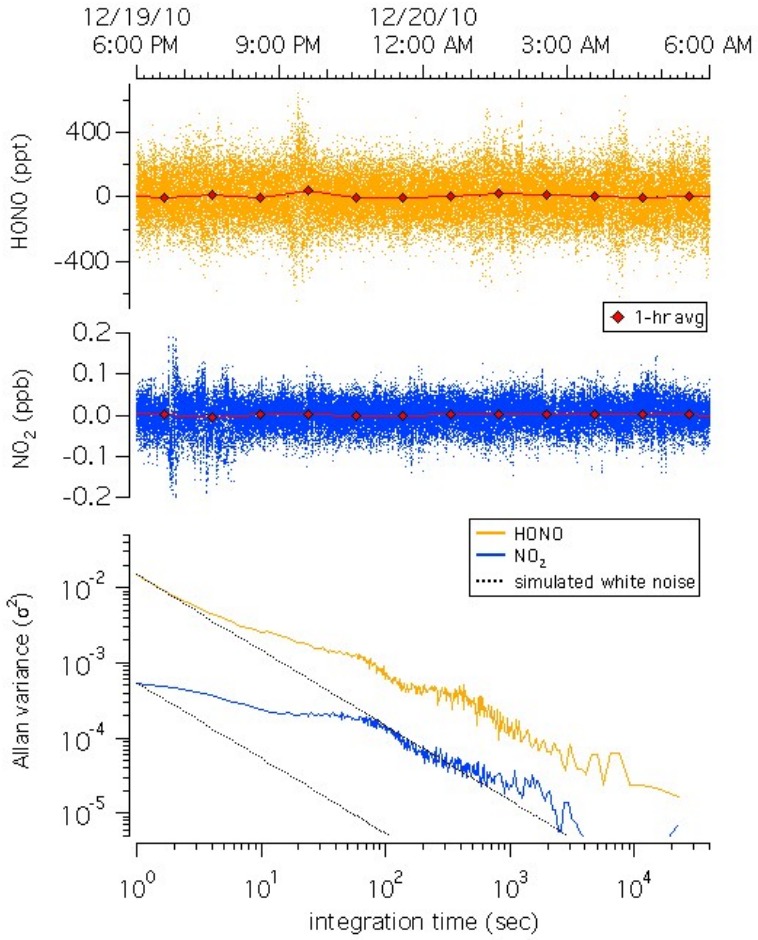

Figure B11. Top panel shows HONO and NO_2 mixing ratios during a 12-hr zero-addition experiment, when the instrument was exposed to typical temperature swings inside the shed at Harvard Forest. Allan variance analysis shows 1-s (1σ) noise for HONO and NO_2 decrease from 100 ppt and 15 ppt by a factor of 20 and 10, respectively, with 1-hr averaging.

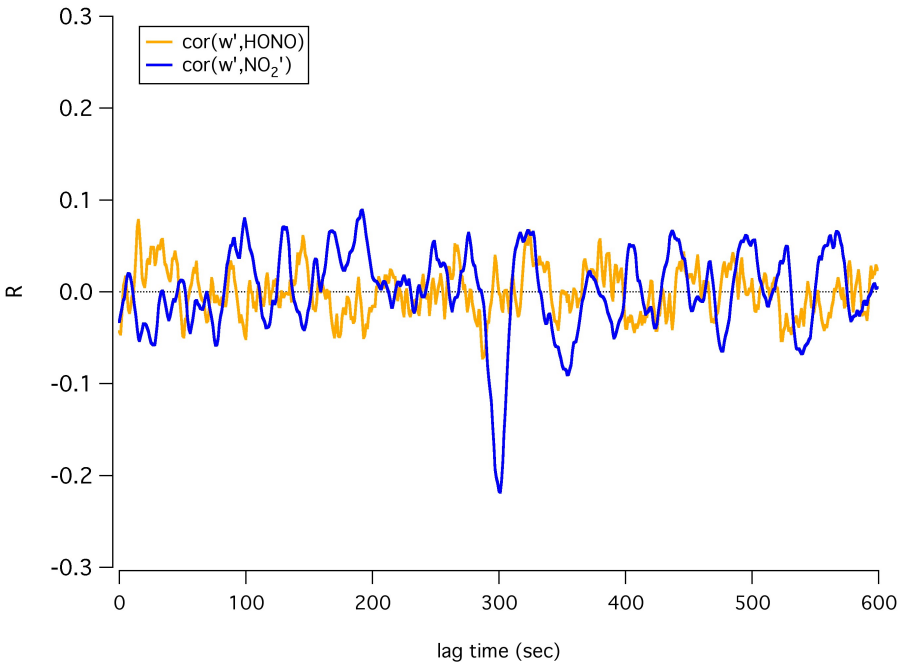

Figure B12. Lag-correlation plot of HONO' (orange) and NO_2' (blue), lagged against w', for a typical 1-hr period (December 31, 2010). A flux signal for NO_2 is detected, which is not the case for HONO.